

Buckling Test Results and Preliminary Test and Analysis Correlation from the 8-Foot-Diameter Orthogrid-Stiffened Cylinder Test Article TA02

Test Dates: 3–6 February 2009

*Mark W. Hilburger
Langley Research Center, Hampton, Virginia*

*W. Allen Waters, Jr.
Analytical Mechanics Associates, Inc., Hampton, Virginia*

*Waddy T. Haynie
Langley Research Center, Hampton, Virginia*

*Robert P. Thornburgh
U.S. Army Research Laboratory, Vehicle Technology Directorate,
Langley Research Center, Hampton, Virginia*

NASA STI Program . . . in Profile

Since its founding, NASA has been dedicated to the advancement of aeronautics and space science. The NASA scientific and technical information (STI) program plays a key part in helping NASA maintain this important role.

The NASA STI program operates under the auspices of the Agency Chief Information Officer. It collects, organizes, provides for archiving, and disseminates NASA's STI. The NASA STI program provides access to the NTRS Registered and its public interface, the NASA Technical Reports Server, thus providing one of the largest collections of aeronautical and space science STI in the world. Results are published in both non-NASA channels and by NASA in the NASA STI Report Series, which includes the following report types:

- **CONFERENCE PUBLICATION.** Collected papers from scientific and technical conferences, symposia, seminars, or other meetings sponsored or co-sponsored by NASA.
- **SPECIAL PUBLICATION.** Scientific, technical, or historical information from NASA programs, projects, and missions, often concerned with subjects having substantial public interest.
- **TECHNICAL TRANSLATION.** English-language translations of foreign scientific and technical material pertinent to NASA's mission.

Specialized services also include organizing and publishing research results, distributing specialized research announcements and feeds, providing information desk and personal search support, and enabling data exchange services.

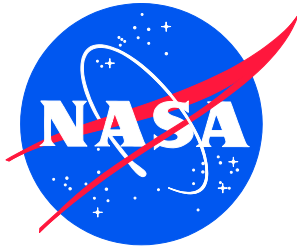
For more information about the NASA STI program, see the following:

- Access the NASA STI program home page at <http://www.sti.nasa.gov>
- E-mail your question to help@sti.nasa.gov
- Phone the NASA STI Information Desk at 757-864-9658
- Write to:
NASA STI Information Desk
Mail Stop 148
NASA Langley Research Center
Hampton, VA 23681-2199

- **TECHNICAL PUBLICATION.** Reports of completed research or a major significant phase of research that present the results of NASA Programs and include extensive data or theoretical analysis. Includes compilations of significant scientific and technical data and information deemed to be of continuing reference value. NASA counter-part of peer-reviewed formal professional papers but has less stringent limitations on manuscript length and extent of graphic presentations.

- **TECHNICAL MEMORANDUM.** Scientific and technical findings that are preliminary or of specialized interest, e.g., quick release reports, working papers, and bibliographies that contain minimal annotation. Does not contain extensive analysis.

- **CONTRACTOR REPORT.** Scientific and technical findings by NASA-sponsored contractors and grantees.



Buckling Test Results and Preliminary Test and Analysis Correlation from the 8-Foot-Diameter Orthogrid-Stiffened Cylinder Test Article TA02

Test Dates: 3–6 February 2009

*Mark W. Hilburger
Langley Research Center, Hampton, Virginia*

*W. Allen Waters, Jr.
Analytical Mechanics Associates, Inc., Hampton, Virginia*

*Waddy T. Haynie
Langley Research Center, Hampton, Virginia*

*Robert P. Thornburgh
U.S. Army Research Laboratory, Vehicle Technology Directorate,
Langley Research Center, Hampton, Virginia*

National Aeronautics and
Space Administration

Langley Research Center
Hampton, Virginia 23681-2199

The use of trademarks or names of manufacturers in the report is for accurate reporting and does not constitute an official endorsement, either expressed or implied, of such products or manufacturers by the National Aeronautics and Space Administration.

Available from:

NASA STI Program / Mail Stop 148
NASA Langley Research Center
Hampton, VA 23681-2199
Fax: 757-864-6500

Preface

The Shell Buckling Knockdown Factor (SBKF) Project was established in the spring of 2007 by the NASA Engineering and Safety Center (NESC) with the goal of developing improved (i.e., less-conservative, more robust), analysis-based shell buckling design factors (a.k.a. knockdown factors) for modern launch-vehicle structures. Preliminary design studies indicated that implementation of these new knockdown factors could help mitigate some of NASA's future launch vehicle development and performance risks by improving baseline designs, providing high-fidelity estimates of structural performance, reducing reliance on testing, and enabling lighter-weight structural designs. To this end, the SBKF project has been engaged in several technical work areas to support the development, validation, and implementation of the new design factors, including subscale and full-scale structural testing. The primary objectives of the test program are to:

1. Provide validation data for high-fidelity structural analysis models and new design knockdown factors.
2. Verify the performance and behavioral characteristics of a variety of buckling-critical structural designs subjected to relevant loading conditions.
3. Determine the effects of common structural details such as weld lands and joints on the buckling response.
4. Understand the effects of scale-up from subscale to full-scale on the buckling response.

To meet these objectives, tests on eight different subscale 8-foot-diameter, integrally stiffened aluminum-alloy cylinders were conducted in order to obtain the majority of the required validation data. In addition, two full-scale, 27.5-foot-diameter, aluminum-lithium, integrally stiffened cylinders were tested to determine structural scaling trends. Data from these tests and the corresponding pretest analysis predictions and data archival information are summarized in a series of NASA technical reports. The pretest predictions presented in these test reports were used to determine the testing and instrumentation requirements and are included herein for reference. Detailed test and analysis correlation are presented in a separate series of NASA technical publications in which refined modeling and analysis results will be discussed thoroughly.

Table of Contents

1.0	Introduction	1
2.0	Test Description.....	2
2.1	Test Objectives.....	2
2.2	Test Article Design	2
2.3	Test Article Fabrication	9
2.4	Test Facility	10
2.5	Testing.....	13
2.5.1	Test article installation and alignment verification.....	13
2.5.2	Instrumentation	14
2.5.3	Low-Speed Digital Image Correlation.....	19
2.5.4	High-Speed Digital Image Correlation (HS-DIC)	19
2.5.5	Load Sequences (LS)	21
3.0	Analysis Description.....	22
4.0	Results and Discussion	23
4.1	Initial Geometric Imperfection Data.....	24
4.2	Buckling Response of TA02-LS4: Combined Axial Compression and Bending Loads with Maximum Compression over the Center of Panel A	25
4.2.1	Load versus Displacement Response.....	25
4.2.2	Full-Field Displacement Contours.....	32
4.2.3	Load versus Axial Strain Response	42
4.2.4	Axial Strain Distribution.....	48
4.3	Buckling Response of TA02 – LS5: Combined Axial Compression and Bending with Maximum Compression over Weld Land BC	54
4.3.1	Load versus Displacement Response.....	54
4.3.2	Full-Field Displacement Contours.....	59
4.3.3	Load versus Axial Strain Response	67
4.3.4	Axial Strain Distribution.....	72
5.0	Concluding Remarks	78
6.0	References	80
Appendix A	Archive Information.....	81
A.1	Plans, Procedures, Drawings and Reports	81
A.2	TA02 Measured Geometry	81
A.3	Test Data	82
A.3.1	Raw Test Data Files	82
A.3.2	Digital Image Correlation Data Files and Contour Plots	83
A.3.3	High-Speed Video.....	83

A.3.4	Photos and Video	83
-------	------------------------	----

List of Figures

Figure 2.1.	Al-Li orthogrid-stiffened cylinder test article, TA01 (post-test).	4
Figure 2.2.	Orthogrid geometry definition.	5
Figure 2.3.	Space shuttle ET and TA02 weld land designs shown in the flat condition for machining.	5
Figure 2.4.	Typical weld land region in TA02.	6
Figure 2.5.	LaRC Drawing 1167189.	7
Figure 2.6.	Measured geometric imperfection for TA02 from photogrammetry/white-light geometry scanning system.	10
Figure 2.7.	Coordinate system and displacement definitions. $\theta = 0^\circ$ corresponds to the center of Panel A and the dashed lines indicate the location of longitudinal weld lands.	10
Figure 2.8.	Eight-foot-diameter shell buckling test facility at MSFC: a) test article assembly, b) hydraulic actuator, c) loading rod, d) load cell, e) attachment ring, f) transition section, g) load strut, and h) loading spider.	12
Figure 2.9.	Test article orientation and panel, weld land, and load line locations.	13
Figure 2.10.	IML strain gage pattern for Panel A in TA02.	15
Figure 2.11.	Schematic view showing locations of EDIs (view from outer surface) and EDI location table.	17
Figure 2.12.	Schematic view showing locations and orientations of EDIs, top view.	18
Figure 2.13.	Location of load lines 1–8 and low-speed DIC and HS-DIC systems.	20
Figure 3.1.	Finite-element model of test assembly.	23
Figure 4.1.	Geometric imperfection data for TA02 from DIC measurement prior to LS4 load application.	25
Figure 4.2.	Measured and predicted load versus end-shortening response of TA02-LS4 subjected to combined axial compression and bending.	27
Figure 4.3.	Measured and predicted prebuckling load versus radial displacement response of TA02-LS4 at the center of each panel.	29
Figure 4.4.	Measured and predicted prebuckling load versus radial displacement response of TA02-LS4 at the center of each longitudinal weld land.	29
Figure 4.5.	Measured and predicted load versus radial displacement response of TA02-LS4 at the center of Panel A and at the center of weld lands AB and CA including the buckling and postbuckling response.	30
Figure 4.6.	TA02-LS4 after buckling.	31
Figure 4.7.	DIC noise signature for u and w displacement measurements prior to TA02-LS4 test.	34
Figure 4.8.	Predicted and measured axial displacement (u) contours at 72.7 kips total load (25% classical buckling load).	35

Figure 4.9.	Predicted and measured radial displacement (w) contours at 72.7 kips total load (25% classical buckling load)	36
Figure 4.10.	Predicted and measured radial displacement (w) contours at 159.9 kips (55% classical buckling load).....	37
Figure 4.11.	Predicted and measured radial displacement (w) contours incipient to buckling.....	38
Figure 4.12.	Predicted and measured initial postbuckling radial displacement (w) contours... ..	39
Figure 4.13.	Measured post-test radial displacement (w) contours showing permanent deformations in the cylinder wall.	39
Figure 4.14.	HS-DIC results illustrating the initiation and propagation of buckling deformations in TA02-LS4.....	41
Figure 4.15.	Predicted and measured strains of back-to-back axial gages, skin and adjacent axial stiffener near center of Panel A. Panel A skin pocket: 029OSA/084ISA, Panel A stiffener: 030ORA/085IRA.	44
Figure 4.16.	Predicted and measured strains of back-to-back axial gages, skin and adjacent axial stiffener near center of Panel B. Panel B skin pocket: 126OSA/158ISA, Panel B stiffener: 127ORA/159IRA.....	45
Figure 4.17.	Predicted and measured strains of back-to-back axial gages, skin and adjacent axial stiffener near center of Panel C. Panel C skin pocket: 190OSA/222ISA, Panel C stiffener: 191ORA/223IRA.....	45
Figure 4.18.	Predicted and measured strains of back-to-back axial gages, center of weld land AB and adjacent axial stiffener in Panel A. Weld land AB: 024OWA/079IWA, Panel A stiffener: 025OWA/080IRA.	46
Figure 4.19.	Predicted and measured strains of back-to-back axial gages, center of weld land BC and adjacent axial stiffener in Panel B. Weld land BC: 122OWA/154IWA, Panel B stiffener: 123ORA/155IRA.	46
Figure 4.20.	Predicted and measured strains of back-to-back axial gages, center of weld land CA and adjacent axial stiffener. Weld land CA: 186OWA/218IWA, Panel C stiffener: 187ORA/219IRA.....	47
Figure 4.21.	Predicted and measured strains of back-to-back axial gages, near buckling initiation location.	48
Figure 4.22.	Predicted and measured axial membrane strain distribution around circumference, 72.2 kips (25% of classical buckling load).	50
Figure 4.23.	Predicted and measured axial membrane strain distribution around circumference, 159.9 kips (55% of classical buckling load).	51
Figure 4.25.	Predicted and measured axial membrane strain distribution around circumference, predicted buckling strains and measured data at 258.1 kips (88.8% classical buckling load), measured buckling strains at 286.2 kips (98.4% classical buckling load).	53
Figure 4.26.	Measured and predicted load versus end-shortening response of TA02-LS5 subjected to combined axial compression and bending.....	55
Figure 4.27.	Measured and predicted load versus radial displacement response of TA02-LS5 at the center of each panel.....	57

Figure 4.28.	Measured and predicted load versus radial displacement response of TA02 at the center of each weld land.....	57
Figure 4.29.	Measured and predicted load versus radial displacement response of TA02 at the center of weld land BC and panels B and C.	58
Figure 4.30.	TA02-LS5 after buckling.....	59
Figure 4.31.	DIC noise signature for u and w displacement measurements for TA02-LS5.	61
Figure 4.32.	Measured initial geometry from DIC systems.	62
Figure 4.33.	Predicted and measured axial displacement (u) contours at 72.8 kips (25% classical buckling load).....	63
Figure 4.34.	Predicted and measured radial displacement (w) contours at 72.8 kips (25% classical buckling load).....	63
Figure 4.35.	Predicted and measured radial displacement (w) contours at 159.6 kips (55% classical buckling load).....	64
Figure 4.36.	Predicted and measured radial displacement (w) contours incipient to buckling.....	64
Figure 4.37.	Predicted and measured radial displacement (w) contours at initial postbuckling equilibrium for TA02-LS5.	65
Figure 4.38.	HS-DIC results illustrating the initiation and propagation of buckling deformations in TA02-LS5.	66
Figure 4.39.	Predicted and measured back-to-back axial strains of skin and axial stiffener near center of Panel A. Panel A skin pocket: 029OSA/084ISA, Panel A stiffener: 030ORA/085IRA.....	69
Figure 4.40.	Predicted and measured back-to-back axial strains of skin and axial stiffener near center of Panel B. Panel B skin pocket: 126OSA/158ISA, Panel B stiffener: 127ORA/159IRA.....	69
Figure 4.41.	Predicted and measured back-to-back axial strains of skin and axial stiffener near center of Panel C. Panel C skin pocket: 190OSA/222ISA, Panel C stiffener: 191ORA/223IRA.....	70
Figure 4.42.	Predicted and measured back-to-back axial strains at center of weld land AB and adjacent axial stiffener. Weld land AB: 024OWA/079IWA, Panel A stiffener: 025ORA/080IRA.....	70
Figure 4.43.	Predicted and measured back-to-back axial strains at center of weld land BC and adjacent axial stiffener. Weld land AB: 122OWA/154IWA, Panel B stiffener: 123ORA/155IRA.....	71
Figure 4.44.	Predicted and measured back-to-back axial strains at center of weld land CA and adjacent axial stiffener. Weld land CA: 187OWA/219IWA, Panel C stiffener: 186ORA/218IRA.....	71
Figure 4.45.	Predicted and measured back-to-back axial strains in selected Panel B skin pockets.	72

List of Tables

Table A1.	Strain Gage Locations and Orientations for TA02	84
-----------	---	----

Table A2.	Electronic Displacement Indicator (EDI) Locations.....	89
Table A3.	Files Used to Generate Color Contour Plots, Load Sequence 4 (Tecplot Format, see Figures 4.8-4.13)	90
Table A4.	Files Used to Generate Color Contour Plots, Load Sequence 5 (Tecplot Format, see Figures 4.34-4.39)	91

Nomenclature

Symbols

δ_{D263AA}	measured displacement: subscript corresponds to specific LVDT channel
imp	measured geometric imperfection
kip	1000 lbf
L	cylinder length
M_{cr}	predicted linear bifurcation buckling load of a cylinder subjected to a bending moment
P_{cr}	predicted linear bifurcation buckling load of a compression-loaded cylinder
R	cylinder OML radius
r_u, r_v, r_w	rotations about the x, θ, z axis
u, v, w	axial, circumferential, and radial displacements
x, θ, z	axial, circumferential, and radial coordinate of a cylindrical coordinate system
$\mu\epsilon$	microstrain or 1.0e-6 strain

Orthogrid design variables

Orthogrid design variables	See Figure 2.2
b_r	circumferential stiffener (ring) spacing
b_s	axial stiffener (stringer) spacing
h	stiffener height measured from the inner skin surface
H	stiffener height measured from the OML ($H = h + t$)
t	shell wall skin thickness
t_{eff}	effective shell wall thicknesses value
t_r	circumferential stiffener (ring) thickness
t_s	axial stiffener (stringer) thickness

Acronyms

fps	frames per second
3D	three dimensional
Al-Li	aluminum lithium alloy
CSS	Central Storage System
DAS	data acquisition system
DIC	digital image correlation
EDI	electronic displacement indicator
ET	External Tank
EU	engineering units
FOV	field(s) of view
HS	high speed

IML	inner mold line (inner surface of structure)
IRIG	Inter-range Instrumentation Group
LaRC	Langley Research Center
LCS	load control system
LPS	load point scans
LS	load sequence
LTA	Load Test Annex
LVDT	linear voltage displacement transformer (type of edi)
MSFC	Marshall Space Flight Center
NESC	NASA Engineering and Safety Center
NSCKN	NASA Safety Center Knowledge Now
OML	outer mold line (outer surface of structure)
SBKF	Shell Buckling Knockdown Factor
SLTMAS	Structural Loads Test Measurement Acquisition System
STAGS	Structural Analysis of General Shells
TA	test article

Abstract

Results from the testing of cylinder test article SBKF-P2-CYL-TA02 (referred to herein as TA02) are presented. The testing was conducted at the NASA Marshall Space Flight Center (MSFC), February 3–6, 2009, in support of the Shell Buckling Knockdown Factor Project (SBKF).¹ The test was the second of two tests used to verify the performance of a newly constructed buckling test facility at MSFC and to verify the test article design and analysis approach used by the SBKF researchers. TA02 is an 8-foot-diameter, 6.5-foot-long, aluminum-lithium (Al-Li), orthogrid-stiffened cylindrical shell similar to those used in current state-of-the-art launch-vehicle structures and was designed to exhibit global buckling when subjected to combined compression and bending loads. Five different load sequences were applied to TA02 during testing and included three sub-critical load sequences, i.e., loading conditions that did not cause buckling or material failure. The sub-critical load sequences consisted of either uniform axial compression loading or combined axial compression and bending. Two different load sequences subjected TA02 to combined axial compression and bending until buckling over two different regions of the cylinder. Traditional displacement transducers and strain gages were used to monitor the test article response at nearly 300 locations and multiple digital image correlation systems were used to obtain low-speed and high-speed full-field displacement measurements of the outer surface of the test article. Overall, the test facility and test article performed as designed. In particular, the test facility successfully applied all desired load combinations to the test article and was able to test safely into the postbuckling range of loading. In addition, the test article failed by global buckling, and the test results correlated well with initial pretest predictions.

1.0 Introduction

Results from the testing of cylinder test article SBKF-P2-CYL-TA02 (referred to herein as TA02 or TA) are presented. TA02 is the second in a series of nine subscale, integrally stiffened metallic cylindrical shells to be tested in the Shell Buckling Knockdown Factor Project (SBKF) test program. TA02 is an 8-foot-diameter, 6.5-foot-long, aluminum-lithium (Al-Li), orthogrid-stiffened cylindrical shell similar to those used in current state-of-the-art launch-vehicle structures and was designed to exhibit global buckling when subjected to combined compression and bending loads. The objectives of this test were to verify the performance of the test facility, the test procedures, and the test article design and analysis approach for cylinders subjected to combined axial compression and bending loads.

First, brief descriptions of the test article design, fabrication, and test are given in Section 2. Next, the modeling and analysis methods used in support of the test article design and testing activities are described in Section 3. Then, selected test results are presented and compared to

¹ NASA Engineering and Safety Center (NESC) Assessment #: 07-010-E

pretest predictions in Section 4. Finally, a complete listing of all test and analysis data, data files and drawings is provided in Appendix A. This listing includes archival directory names, file names, and file format descriptions. All references used to support the test are also provided and include test article design drawings, test article fabrication and test plans and procedures, and pretest analysis results.

2.0 Test Description

Cylinder test article TA02 was designed by SBKF project researchers at NASA Langley Research Center (LaRC) Structural Mechanics and Concepts Branch (D312) and was fabricated by the NASA Marshall Space Flight Center (MSFC) Metal Joining and Processing Branch (EM32). The testing of TA02 occurred on February 3–6, 2009 at MSFC in Building 4619 Load Test Annex (LTA) under the direction of the Structural Strength Test Group (ET30). A special-purpose test apparatus was designed and fabricated for the SBKF test effort. The test apparatus was designed to apply up to 1.5 million pounds of total force in axial compression and bending and 10 psi internal pressure. A multi-channel load control system (LCS) was used to apply the test loads and included load control and displacement control options. Traditional strain and displacement data were obtained from 294 locations on the test article and full-field displacement data were obtained on the test article outer mold line (OML) by using low-speed and high-speed (HS) digital image correlation (DIC) systems. This section gives a brief overview of the test objectives, test article, instrumentation, test facility, and test load cases. Additional details on the testing of TA02 can be found in the test plan and test procedure (Refs. 1 and 2).

2.1 Test Objectives

The test of TA02 was designed to provide data necessary to verify the test apparatus performance and the test article design approach for a cylinder subjected to combined axial compression and bending loads and included the following objectives:²

1. Verify the operation and performance of the test system. Specifically, verify the adequacy of the test procedures, verify instrumentation, and low-speed and HS-DIC systems and measurements, and assess test article/test fixture designs.
2. Obtain test data necessary to verify the test article design and analysis approach through detailed test and analysis correlation.

2.2 Test Article Design

TA02 is an 8-foot-diameter, 6.5-foot-long, orthogrid-stiffened cylindrical shell (nominal dimensions) and is constructed from three 2195 Al-Li integrally stiffened curved-panel segments (120° arc segments) that were friction-stir welded together to form a complete cylinder. The test article TA02 used the same design as TA01 (Ref. 3). The design included similar design features and response characteristics as those found in current state-of-the-art launch-vehicle cylinder structures to maximize the applicability of the test data to the design of future test articles and

² TA01 was tested to buckling November 2008 (Ref. 3) and was used to verify the test apparatus performance and the test article design approach for a cylinder subjected to uniform compression. TA02, as reported herein, was subjected to several different loading conditions including combined axial compression and bending until buckling and collapse in order to verify the performance of the system under combined loading conditions and complete the design and test-system verification process.

modern launch vehicles. A post-test photo of TA01 is shown in Fig 2.1. The visible internal axial and circumferential grid pattern corresponds to the internal stiffeners, referred to herein as an orthogrid stiffener pattern or orthogrid.

One of the primary objectives of the test, as described in Section 2.1, was to verify the performance of the test apparatus and thus specific requirements on the test article response and test data were defined. In particular, the test article was to exhibit global buckling at a load level between 50% and 70% of the loading capacity of the apparatus when subjected to combined axial compression and bending loads. In addition, the test article was to exhibit an unstable collapse response characterized by a sudden reduction in axial load and release of potential energy, which is common in the buckling of thin-walled cylinders, so that the safe control of testing into the postbuckling range of loading could be demonstrated.

The test article was designed using a two-step process as described in Ref. 4. First, the acreage stiffener pattern was designed using closed-form solutions, assuming a uniform construction throughout the cylinder, i.e., the effects of the axial weld lands were excluded. Several design constraints were applied during the design process to ensure that the test article would fail due to global buckling only and to minimize the potential for failure mode interactions. To this end, margins of at least 20% were required on all other failure modes, such as skin pocket buckling (buckling of the skin between stiffener elements), stiffener buckling, and material yielding. The design variables included the skin thickness t , stiffener height h , axial and circumferential stiffener thickness t_s and t_r , respectively, and axial and circumferential stiffener spacing b_s and b_r , respectively (see Fig. 2.2 for orthogrid schematic). The resulting acreage design includes a skin thickness of 0.100 inches, axial and circumferential stiffener spacing of 4.0 inches, axial and circumferential stiffener thickness of 0.100 inches, and a stiffener height, H , of 0.400 inches as measured from the OML. The design corresponds to an $R/t_{eff} = 230.9$, where t_{eff} is an effective shell wall thicknesses value defined in Fig. 2.2. A_{11} and A_{22} are axial and circumferential membrane stiffnesses, respectively, and D_{11} and D_{22} are axial and circumferential bending stiffnesses, respectively, as defined in Ref. 5.

Next, the three axial weld lands were introduced into the test article design and the shell response was analyzed using a detailed geometrically nonlinear finite element analysis (Ref. 4). One of the design objectives was to include scaled versions of the weld land design used on the 27.5-foot-diameter space shuttle external tank (ET) (see Fig. 2.3a). Scaling of the ET weld land geometry corresponded to a test article weld land thickness and half-width equal to 0.093 inches and 1.164 inches, respectively. However, due to restrictions on the welding process and fixtures at the time of manufacturing, the weld thickness was limited to a minimum of 0.25 inches, and weld land width was limited to a minimum of 2.5 inches (half-width of 1.25 inches).

Results from a detailed finite-element analysis of the preliminary test article design with three axial weld lands indicated that the test article would be susceptible to local buckling along the weld lands due to the lower bending stiffness in these locations. Thus, additional reinforcement was added to the acreage areas adjacent to the weld lands in order to remove the local buckling response along the weld lands. Specifically, an additional axial stiffener was added on both sides of the weld land and the thickness of several of the stiffeners was increased as shown in Fig. 2.3b and in Fig. 2.4. Finite element analysis results of this reinforced weld land design indicated that these additional stiffeners eliminated the initiation of buckling in the weld land region and that

the test article would exhibit behavioral characteristics similar to a uniform cylinder (Ref. 4). The final design drawing, LaRC Drawing 1167189, is shown in Fig. 2.5 (Ref. 6).

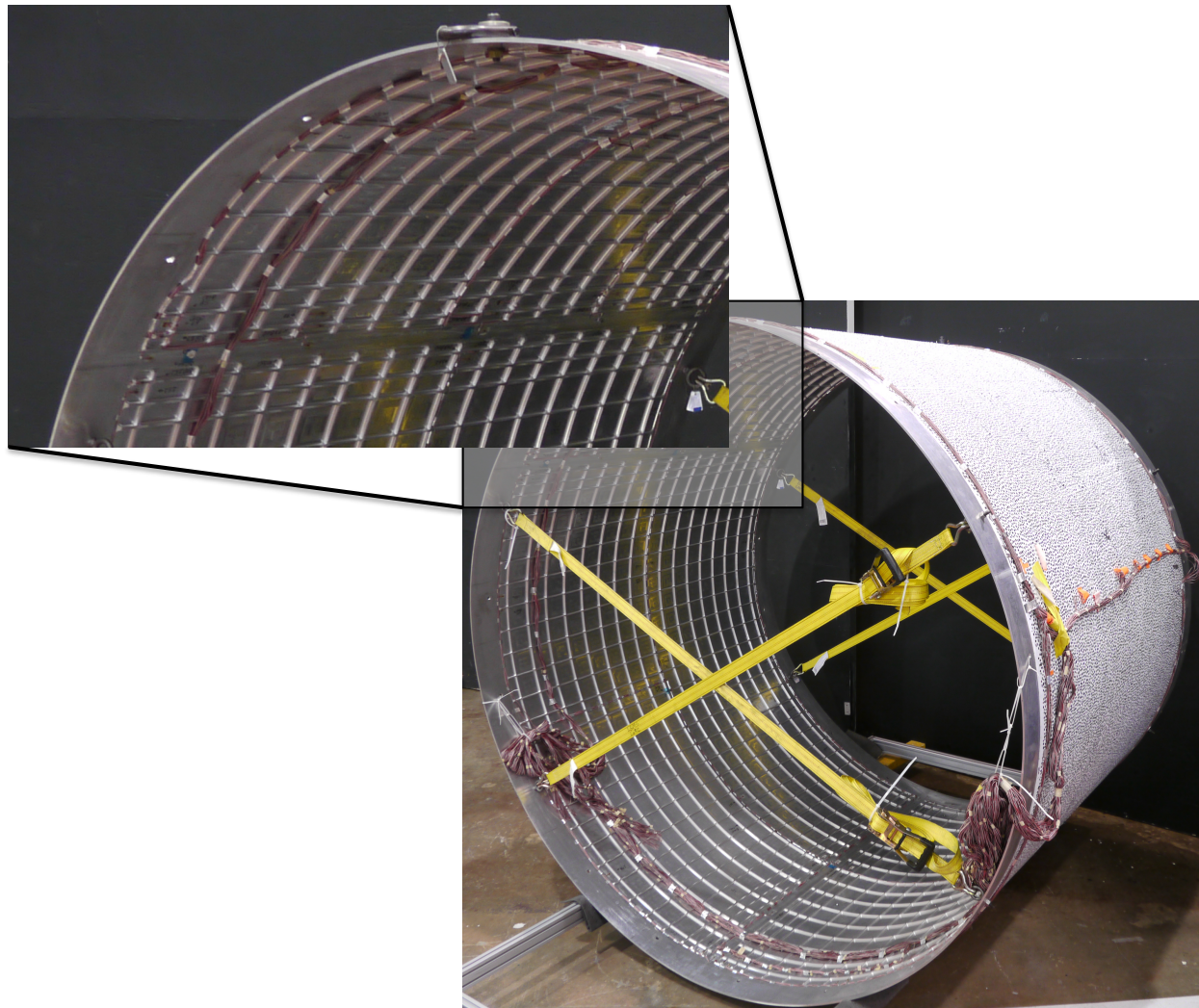
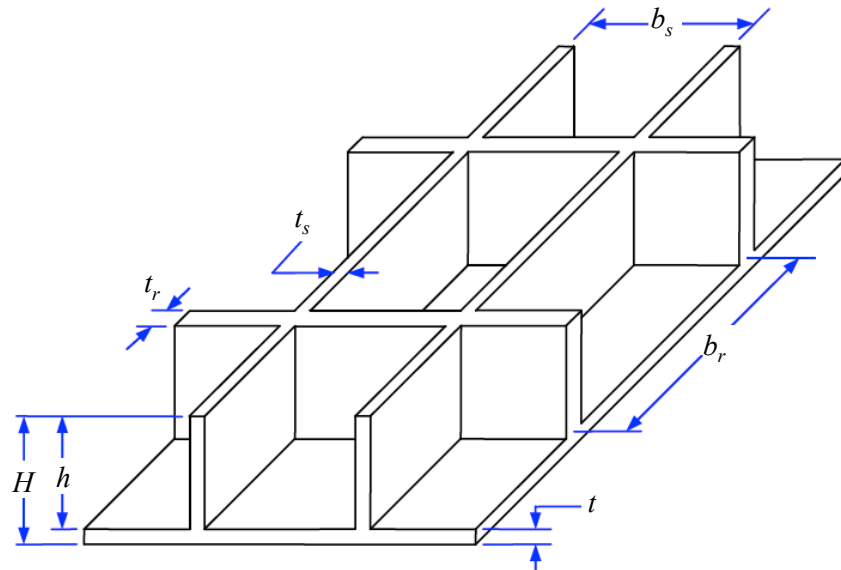


Figure 2.1. Al-Li orthogrid-stiffened cylinder test article, TA01 (post-test).



$$t = 0.100\text{-inch} \quad H = 0.400\text{-inch} \quad b_r = 4.000\text{-inch} \quad t_r = 0.100\text{-inch}$$

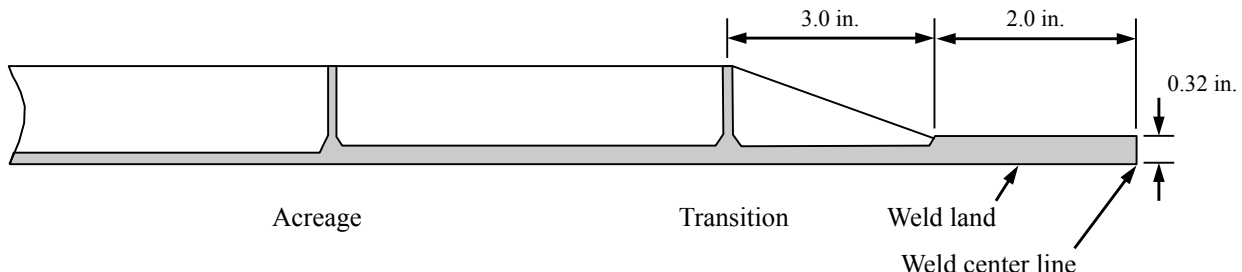
$$b_s = 4.000\text{-inch} \quad t_s = 0.100\text{-inch} \quad h = 0.300\text{-inch}$$

$$L/D: \text{Barrel length to diameter ratio} = 0.816$$

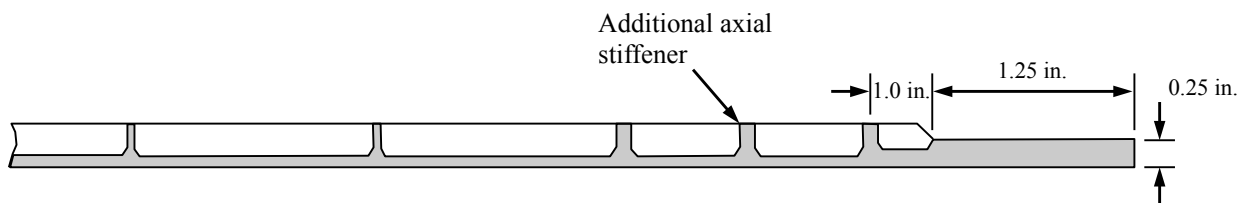
$$R/t_{eff}: \text{Radius to effective wall thickness ratio} = 230.9$$

$$t_{eff} = \sqrt[4]{\frac{144D_{11}D_{22}}{A_{11}A_{22}}}$$

Figure 2.2. Orthogrid geometry definition.



a) Typical space shuttle ET weld land design cross-section (not to scale).



b) TA02 weld land design cross-section (not to scale).

Figure 2.3. Space shuttle ET and TA02 weld land designs shown in the flat condition for machining.

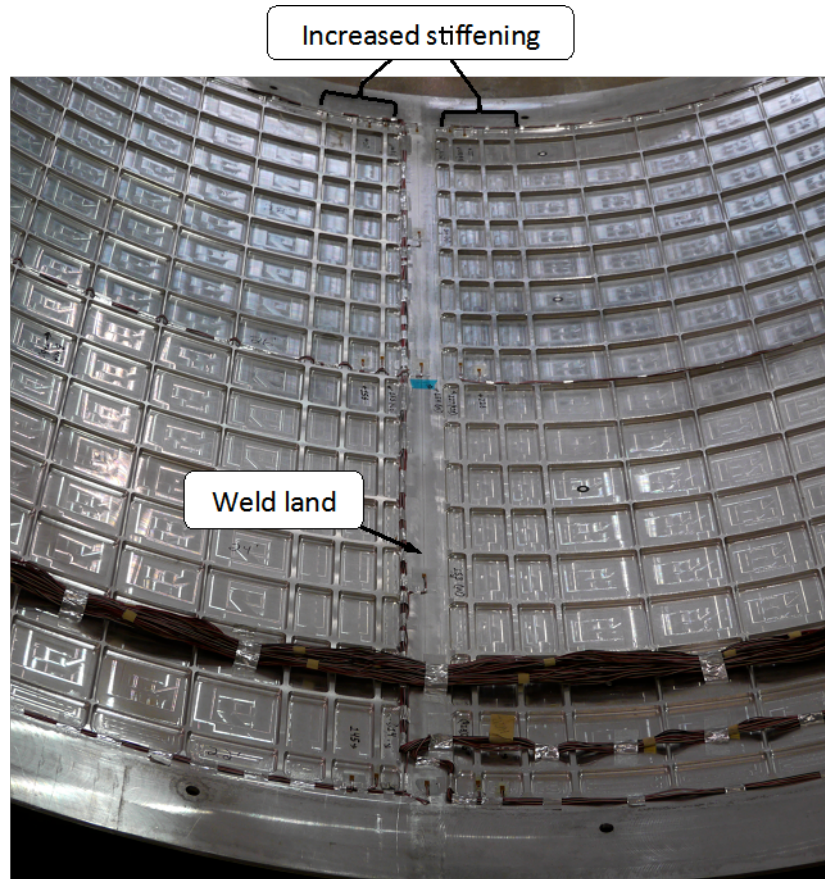
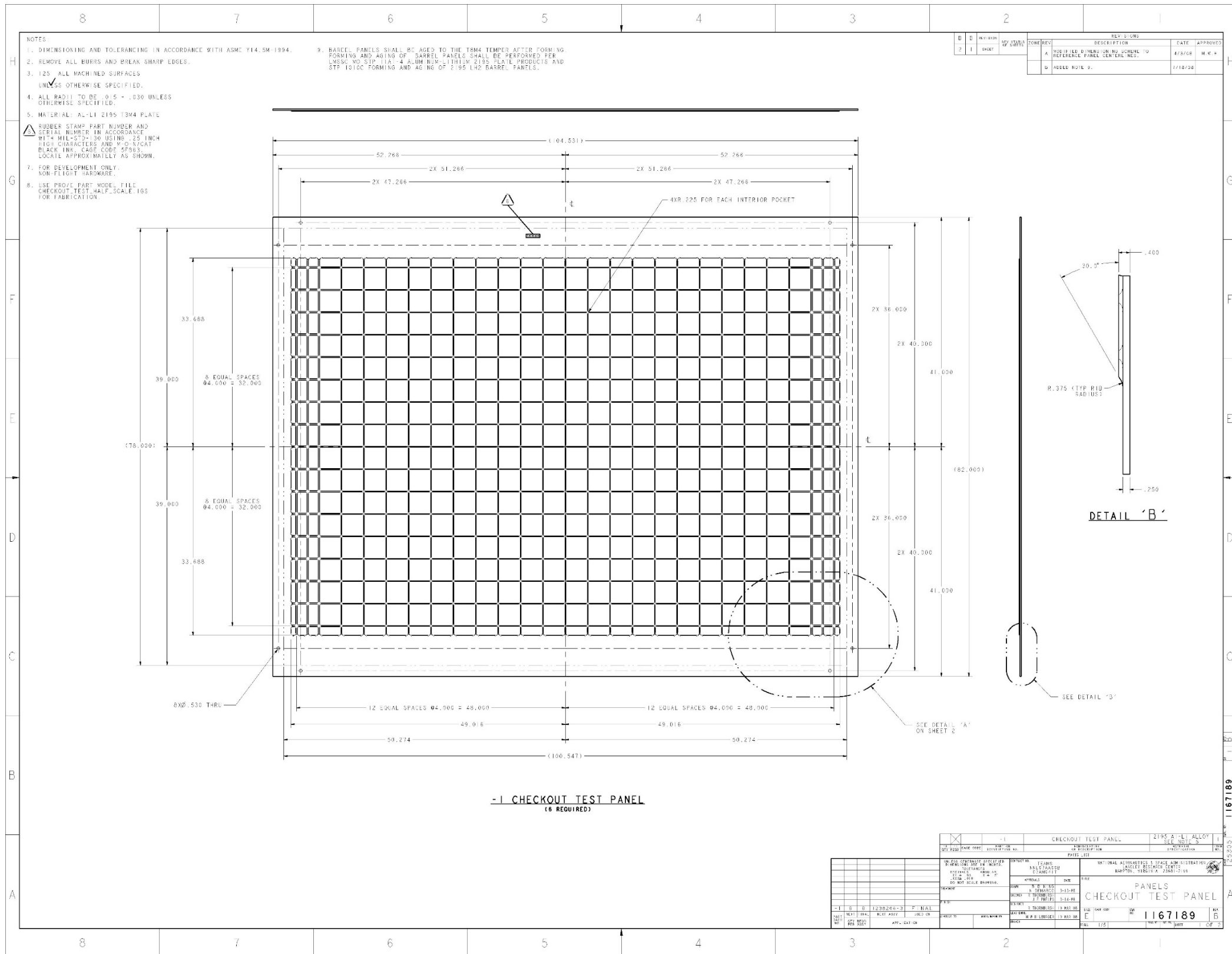
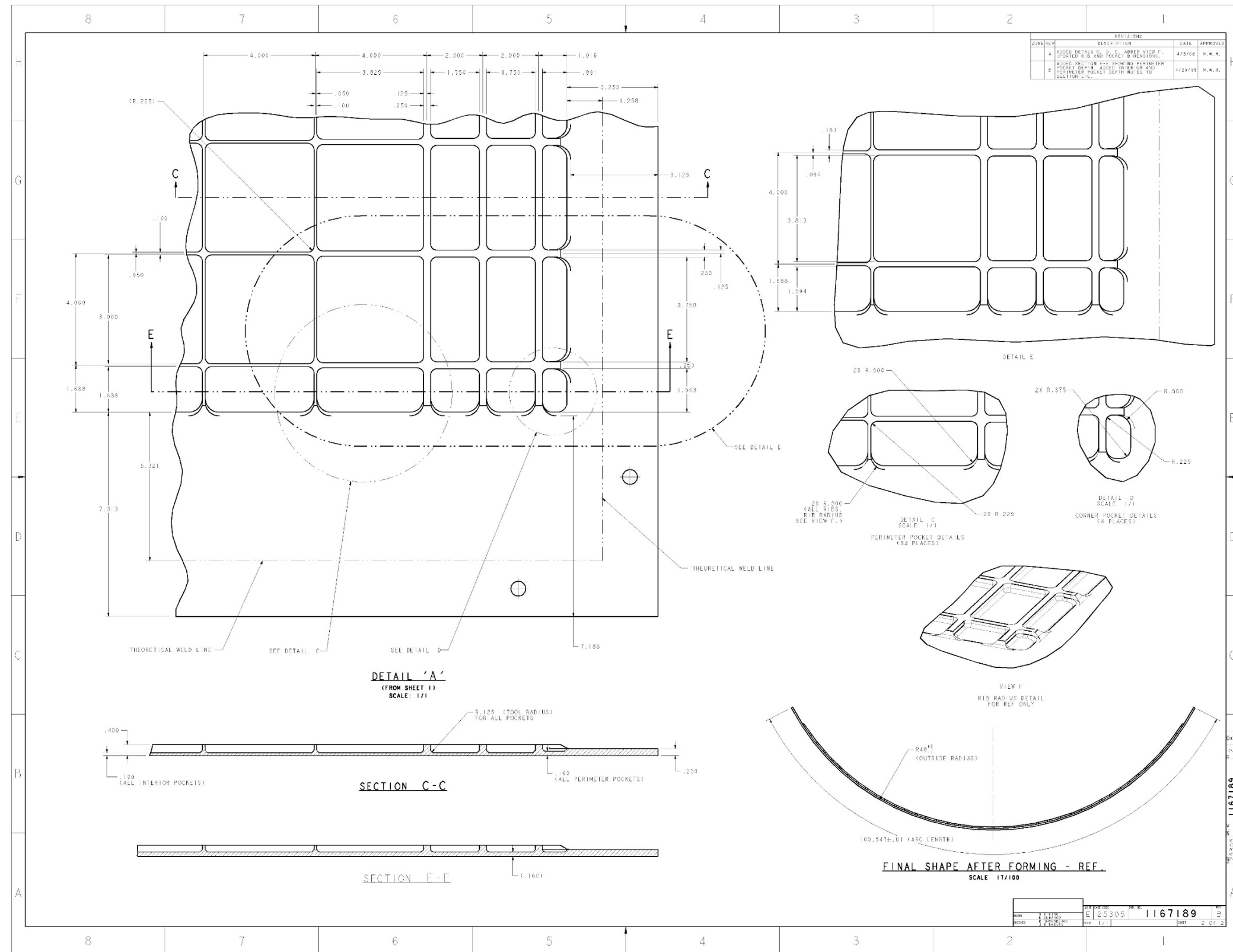


Figure 2.4. Typical weld land region in TA02.



a) Inner mold line (IML) orthogrid stiffener pattern for a TA02 panel segment

Figure 2.5. LaRC Drawing 1167189



b) TA02 panel segment details
Figure 2.5. Concluded.

2.3 Test Article Fabrication

Three curved panel segments were used to construct the cylinder and were fabricated in a three-step process. First, flat orthogrid-stiffened panels were fabricated by machining the stiffener pattern into 2195-T3 Al-Li flat-plate material to form the pockets and weld land details. After machining, the orthogrid panels were visually inspected for flaws and the skin pocket thicknesses, and stiffener heights and thicknesses were measured using a Leica AT901 laser tracker system³ to verify that they were built to specified tolerances. Following inspection, the flat orthogrid panels were bump-formed using a brake press (while in the -T3 temper) into curved panel segments with an OML radius of 48 inches. Finally, the panels were heat treated and aged to a -T83 temper. Once machined, formed, and heat treated, the three orthogrid panels, referred to as Panels A, B, and C, were friction-stir welded together along the axial weld lands to form a cylinder with an 8-foot (96-inch) OML diameter and a 6.5-foot (78-inch) length. The three weld lands joining the three panels were 0.250 inches thick, and 1.25 inches wide on either side of the weld seam, resulting in a total weld-land width of 2.5 inches (all dimensions nominal). Each weld was subjected to a series of visual and ultrasonic quality inspections (see Ref. 7). No defects or anomalies were identified in the welds of TA02.

After the panels had been welded into a cylinder, the ends of the test article were machined flat and parallel to tolerances specified in the manufacturing and assembly drawing 1238206 (Ref. 8) in an effort to provide uniform load introduction into the test article. The top and bottom ends of the test article were measured using a Leica AT901 laser tracker system to verify the tolerances on flatness and parallelism. The measurements indicated the top and bottom ends of the test article were flat to within 0.030 inches and 0.027 inches, respectively, and parallel to each other to within 0.035 inches.

Once machining and inspection were complete, each end of the test article was potted in an attachment ring (Ref. 9). Concentricity and bolt-hole alignment specifications for the top and bottom attachment rings were defined so as to minimize any loads that would result from the misalignment of the test assembly. Shims were used to position the test article in the attachment rings and adjust concentricity. Ring alignment and concentricity were verified using a plumb bob.

Once potted, the geometry of the test article OML was measured using a GOM ATOS photogrammetry/white-light geometry measurement system⁴ with a measurement accuracy of ± 0.001 inch. The deviation of the measured geometry from a best-fit circular cylinder was calculated and defined as the initial geometric imperfection (*imp*) and is shown in Fig. 2.6. The coordinate system used in the geometry measurement is shown in Fig. 2.7. The three longitudinal weld lands are located at $\theta = -60^\circ, 60^\circ$ and 180° and the $\theta = 0^\circ$ location is aligned with the center of Panel A. The OML geometry data indicate that the test article is circular to within ± 0.10 inches. The weld lands do not appear to have a strong influence on or correlation with the imperfection pattern, rather, local geometry variations appear across the mid-length of Panels A and B and are attributed to a slight over-forming during the bump-forming process which was reported by the panel manufacturer. In addition, the top and bottom attachment ring loading

³ http://www.leica-geosystems.us/en/Leica-Absolute-Tracker-AT901_69047.htm, current as of May 2016.

⁴ <http://www.gom.com/metrology-systems/3d-scanner.html>, current as of May 2016.

surfaces of the test article assembly were measured using a Leica AT901 laser tracker system to verify the tolerances on flatness and parallelism. The top and bottom attachment ring loading surfaces were flat to within 0.012 inches and 0.013 inches, respectively, and were parallel to each other to within 0.013 inches. The orthogrid design, attachment ring design and barrel assembly are presented in Drawings 1167189 (Ref. 6), 1238206 (Ref. 8) and 1238205 (Ref. 9), respectively, and in Section 2.1 of the test plan (Ref. 1).

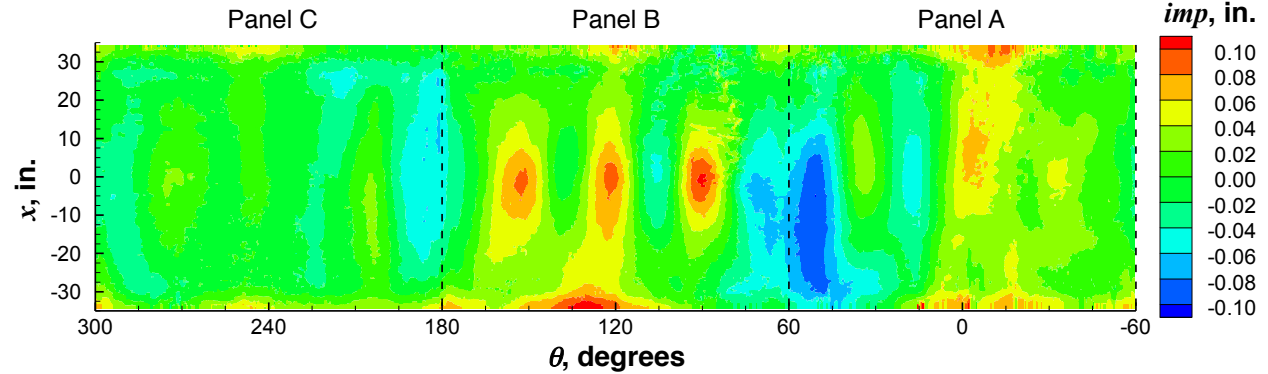


Figure 2.6. Measured geometric imperfection for TA02 from photogrammetry/white-light geometry scanning system.

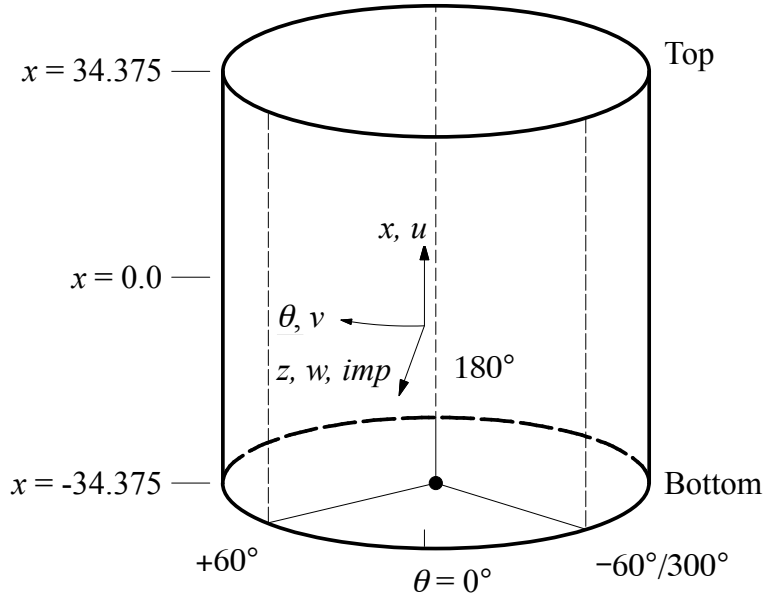


Figure 2.7. Coordinate system and displacement definitions. $\theta = 0^\circ$ corresponds to the center of Panel A and the dashed lines indicate the location of longitudinal weld lands.

2.4 Test Facility

The test facility is comprised of the test assembly (test article, test fixtures), LCS, and data acquisition system (DAS). The test assembly is shown in Fig. 2.8 and engineering drawings are found in Drawing 90M12370 (Ref. 10). The test assembly is a self-reacting load system composed of an upper and lower load “spider”, 16 load struts, upper and lower load-introduction cylinders (referred to in Ref. 10 and Fig. 2.8 as transition sections), pressure plates, the test article assembly, and eight load lines. Each load line consists of a hydraulic actuator, a 4-inch-

diameter loading rod, a load cell, and attachment hardware. Each load line attaches to the upper and lower loading spiders. The load lines can be controlled independently in load control or stroke (position) control to apply uniform compression or combined compression and bending with a maximum load capability of 1.5 million pounds of axial compression force and 80,000 pounds of axial tension force. The test fixtures were designed and analyzed to ensure uniform load introduction into the test article when subjected to uniform compression or combined axial compression and bending up to the maximum load capability of the assembly. It should be noted that the load lines are in tension when the TA is subjected to compression loads. Additional information on the loading structure is also documented in Drawing 90M12375 (Ref. 11). A top-view schematic of the test assembly is presented in Fig. 2.9 and indicates the test article orientation and load line locations (indicated by the filled circle symbols in the figure) with respect to the panel and weld locations. In addition, the three panel sections that comprise the barrel test article are labeled as Panels A, B, and C.

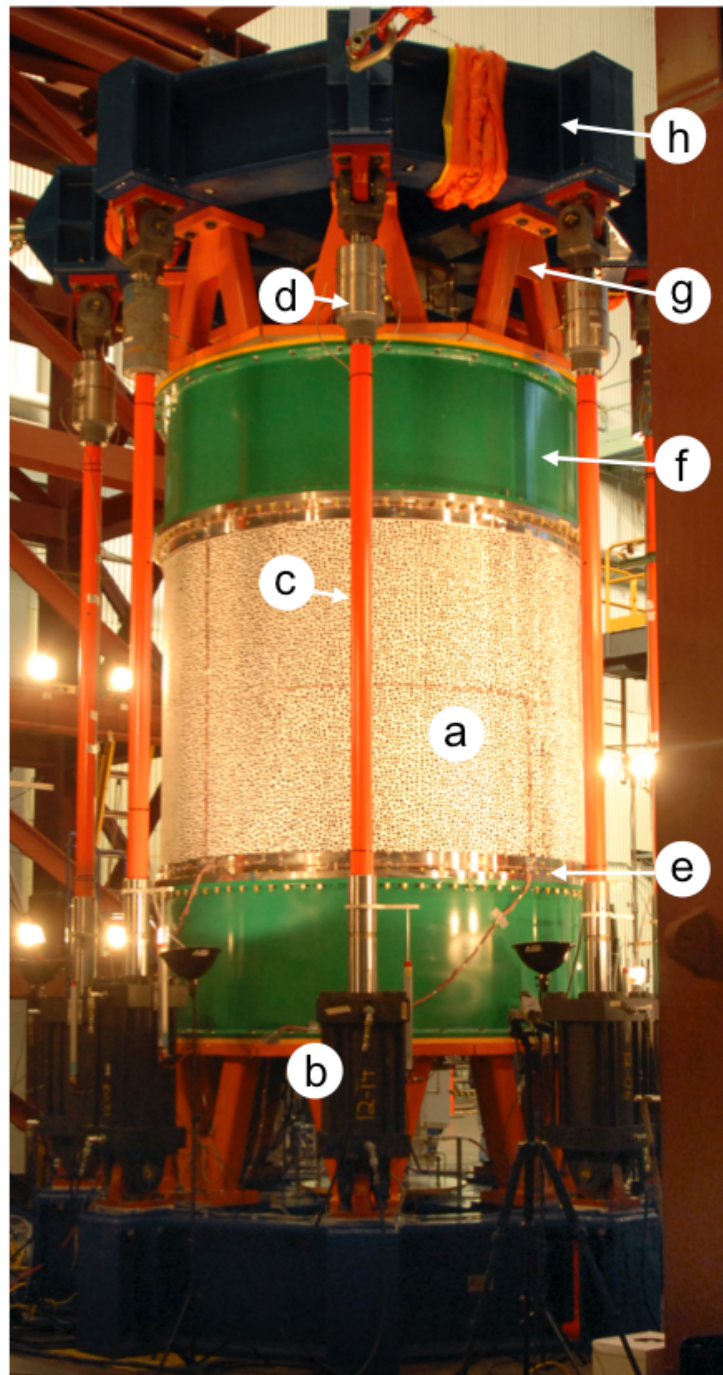


Figure 2.8. Eight-foot-diameter shell buckling test facility at MSFC: a) test article assembly, b) hydraulic actuator, c) loading rod, d) load cell, e) attachment ring, f) transition section, g) load strut, and h) loading spider.

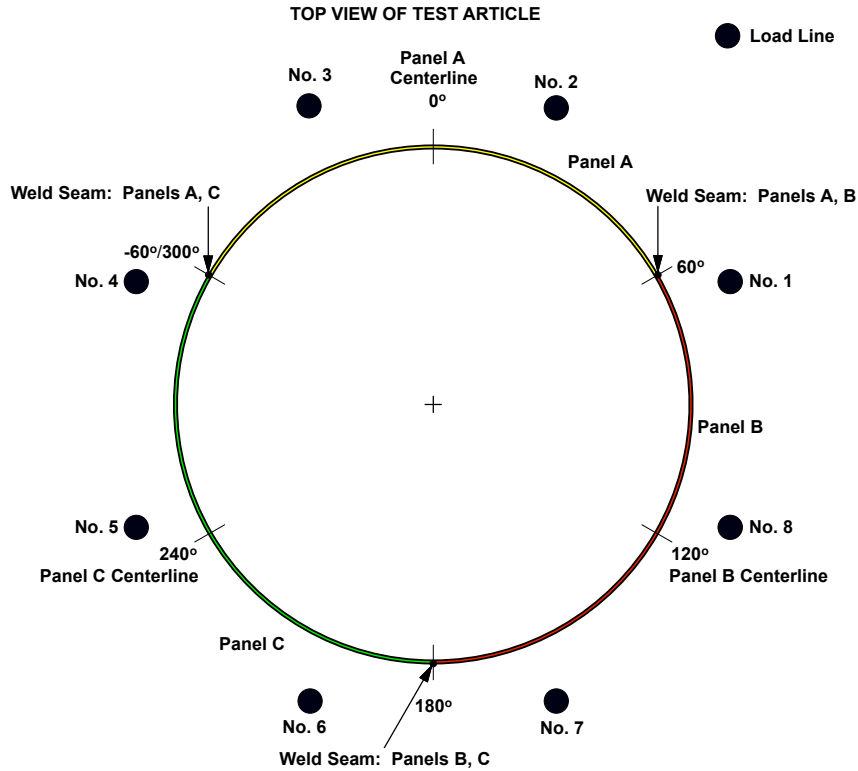


Figure 2.9. Test article orientation and panel, weld land, and load line locations.

The DAS was a custom-built Structural Loads Test Measurement Acquisition System (SLTMAS) developed by MSFC/ET30 that can record up to 4792 analog inputs and 192 digital inputs. The DAS uses National Instruments SCXI-1520 signal conditioners for the strain gages, load cells, and linear voltage displacement transducers (LVDTs). Data was taken at a rate of 2 Hz.

The LCS was an MTS FlexTest® 60 multi-channel system and was programmed to use a combination of load control and position control during the testing. More specifically, during sub-critical load sequences, the LCS applied loads to TA02 in load control to ensure uniform loading. However, during the load sequences (LS) to failure, LS4 and LS5, the LCS was programmed to apply loads in load control up to the buckling event. Once buckling occurred, as indicated by a significant reduction in load in the load lines, the LCS automatically transitioned to displacement (stroke) control so that the test could proceed safely through any additional unstable buckling events in the postbuckling range of loading. In all load cases, the LCS was programmed such that the load rate never exceeded 10,000 lbf per minute in any individual load line. Specific load control requirements are defined in the test plan and test procedure.

2.5 Testing

2.5.1 *Test article installation and alignment verification*

Once the TA was installed into the test fixture and the load lines were mounted between the upper and lower loading spiders, relative alignment between the TA and the load lines was measured using the Leica laser-tracker based position measurement system with an accuracy of ± 0.001 degree. These measurements indicated that the load lines were parallel to the axis of the

TA to within 0.050 degrees on average, corresponding to a misalignment of 0.18 inches from top to bottom.

2.5.2 *Instrumentation*

TA02 was instrumented with 270 strain gages and the pattern for the barrel panels is shown in Fig. 2.10 (Ref. 12). Strain gage locations and naming convention are summarized in Table A1 in Appendix A. Twenty-four electronic displacement indicators (EDIs), also referred to as LVDTs, were placed at various locations on the specimen to measure axial, radial, and tangential displacements. Schematic views of the EDI measurement locations and orientations are shown in Figs. 2.11 and 2.12. In particular, axial displacement measurement locations are indicated by open circle symbols and radial and tangential measurements are indicated by arrows in Fig. 2.12. EDI locations and naming convention are summarized in Table A2 in Appendix A.

The axial end-shortening of TA02 was measured at four locations around the circumference of the test article. The axial end-shortening corresponds to the relative axial displacement between the upper and lower test article attachment rings at the 0°, 90°, 180°, and 270° locations around the circumference of the test article. The end-shortening measurements are defined as follows:

$$\begin{aligned} 0^\circ: \delta_{D263AA} &= \delta_{D239AA} - \delta_{D259AA} \\ 90^\circ: \delta_{D264AA} &= \delta_{D240AA} - \delta_{D260AA} \\ 180^\circ: \delta_{D265AA} &= \delta_{D241AA} - \delta_{D261AA} \\ 270^\circ: \delta_{D266AA} &= \delta_{D242AA} - \delta_{D262AA} \end{aligned}$$

where δ_{D239AA} , δ_{D240AA} , δ_{D241AA} , δ_{D242AA} and δ_{D259AA} , δ_{D260AA} , δ_{D261AA} , δ_{D262AA} correspond to axial EDI measurements on the top and bottom attachment rings, respectively, and δ_{D263AA} , δ_{D264AA} , δ_{D265AA} , δ_{D266AA} correspond to the derived end-shortening displacements. Similarly, transverse shear displacement and twisting of the cylinder were determined from the relative radial and tangential displacements measured at the top and bottom attachment rings. Finally, LVDTs were used to measure radial displacements at the center of each panel segment and at the center of each weld as well as two additional locations within Panel A near the lower attachment ring.

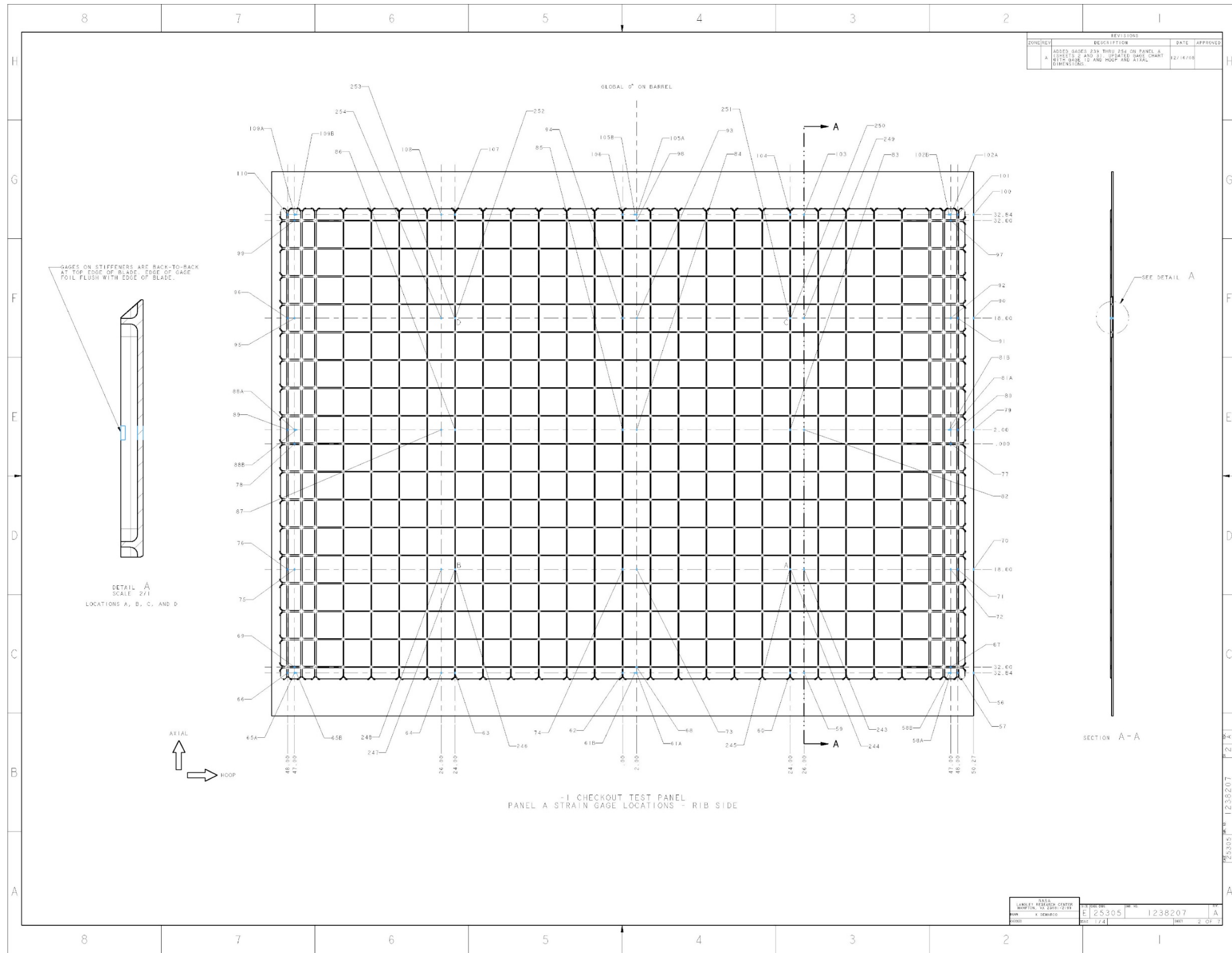


Figure 2.10. IML strain gage pattern for Panel A in TA02

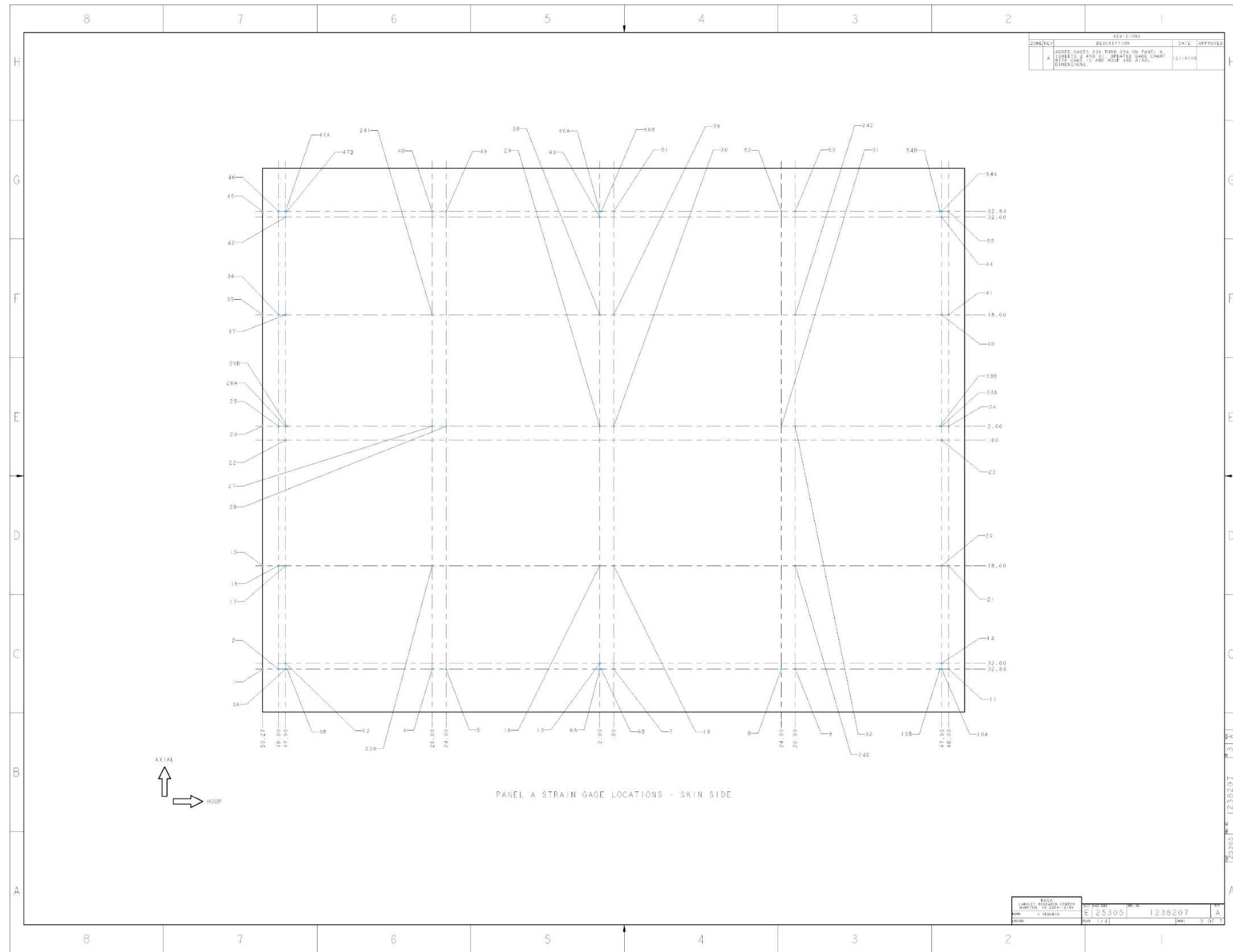
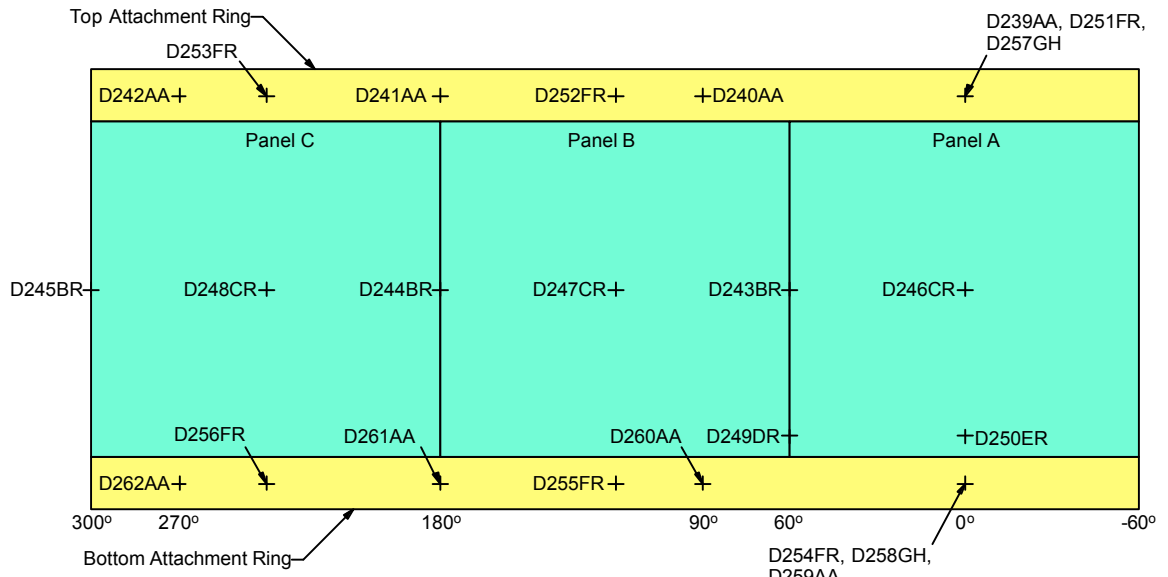


Figure 2.10. OML strain gage pattern for Panel A in TA02. Concluded



Key to EDI Nomenclature: DXXXZY

Solid vertical line between panels corresponds to a weld land

"+" indicates EDI measurement location.

XXX - EDI Identifier No.

Y - Location Code A-G From Test Plan

Z - Orientation: A - Axial

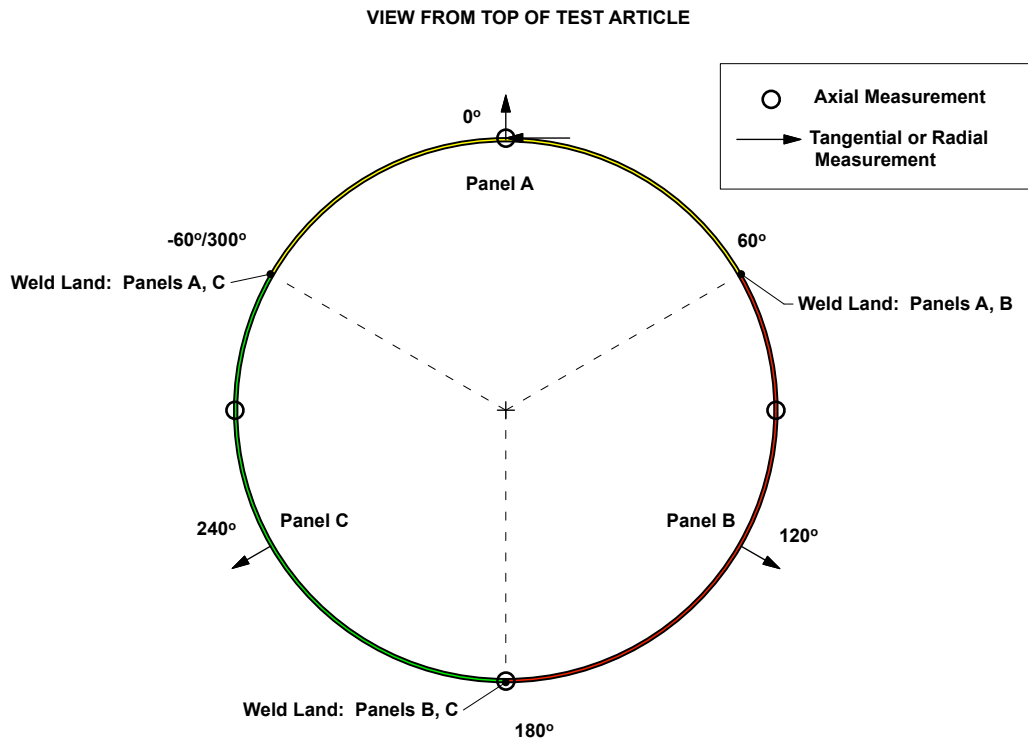
R - Radial

H - Tangential

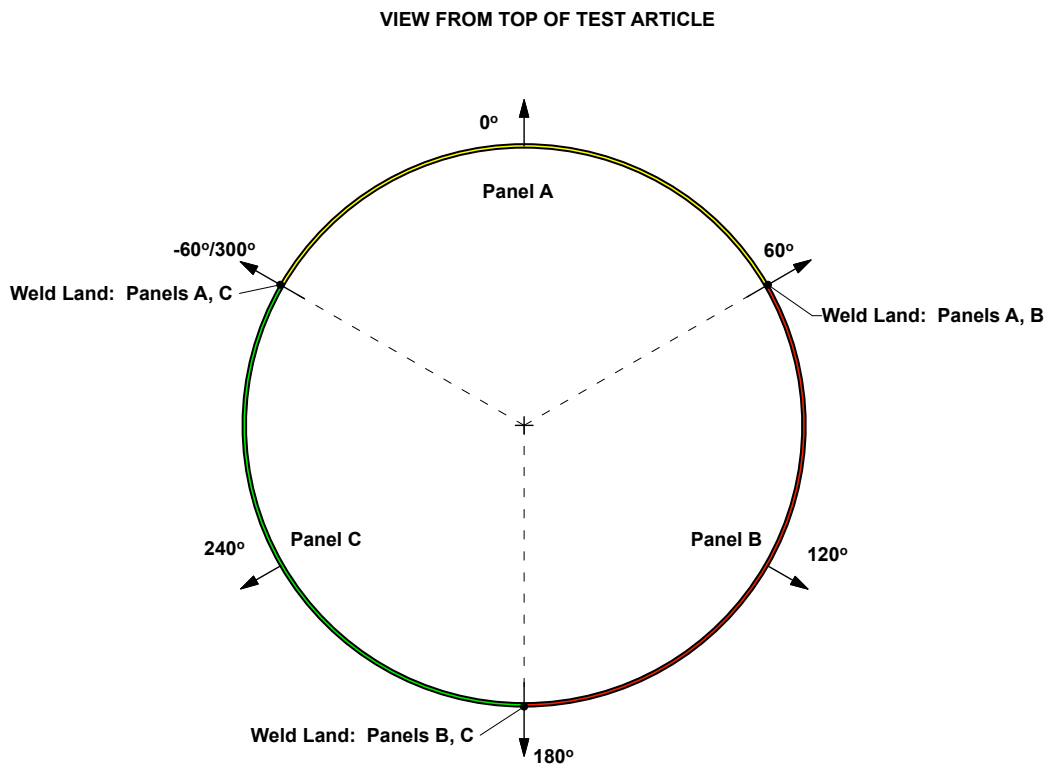
Y – EDI Location Code

A	axial displacement measurements at four places on the top and bottom attachment rings
B	radial displacement measurements at the mid-length of each weld land
C	radial displacement measurements at the center of each panel
D	radial displacement measurement of weld land AB (weld land between Panel A and Panel B) 5 inches up from the bottom attachment ring
E	radial displacement measurement at mid-arc-width of Panel A ($\theta = 0^\circ$) and 5 inches up from the bottom attachment ring
F	radial displacement measurements at three points on both the bottom and top attachment rings, located at the mid-arc-width of each panel
G	tangential displacement measurements on both the bottom and top attachment rings, located at $\theta = 0^\circ$

Figure 2.11. Schematic view showing locations of EDIs (view from outer surface) and EDI location table.



a) Axial, radial, and tangential displacement measurement locations on the top and bottom attachment rings.



b) Radial displacement measurement locations at the test article mid-length.

Figure 2.12. Schematic view showing locations and orientations of EDIs, top view.

2.5.3 Low-Speed Digital Image Correlation

Low-speed DIC was used to obtain full-field three-dimensional (3D) displacement data on approximately 90% of the TA OML surface. Schematics of the DIC coordinate system and field of view (FOV) are presented in Figs. 2.7 and 2.13, respectively. Complete coverage could not be achieved due to two of the eight load lines obstructing the views of the DIC system cameras, specifically, load lines 4, and 8 as illustrated in Fig 2.13. Note: the camera locations and FOV indicated in Fig. 2.13 are notional and are not to scale.

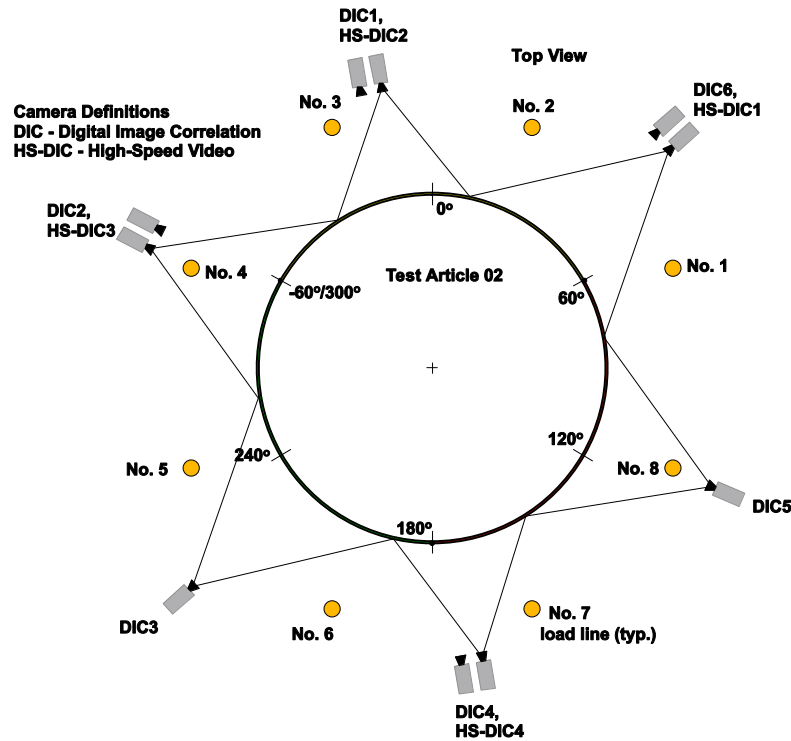
Prior to each load sequence, several images of the unloaded TA were taken with each DIC system to help characterize the measurement noise. Typical measurement noise of ± 0.004 inches in the axial u displacements and ± 0.010 inches in the radial w displacements was observed. The DIC system was also used to measure a pretest OML surface geometry for correlation with previous white-light geometry measurements (described in Section 2.3) in order to verify that no significant changes in geometry had occurred between manufacturing and test integration. DIC data (images) were acquired every 10 seconds throughout each load sequence using the 2007 Correlated Solutions Vic-Snap software.⁵ Displacement data were processed using the 2007 Correlated Solutions VIC-3D™ software and converted into cylindrical coordinates (coordinate system defined Fig. 2.7). It should be noted that some of the DIC data presented herein exhibits slight discontinuities in data values in the regions where adjacent DIC systems overlap. These discontinuities are attributed to system-to-system differences in the measurement error. In addition, it is noted that the measurement error typically is greater at the measurement boundaries, i.e., the extreme values of the circumferential location.

The VIC-3D™ session files, all calibration information, and all acquired images have been archived to enable further detailed processing at a later date. The DIC requirements and setup information are presented in more detail in Section 3.0 of Ref. 1. See Appendix A for archival information.

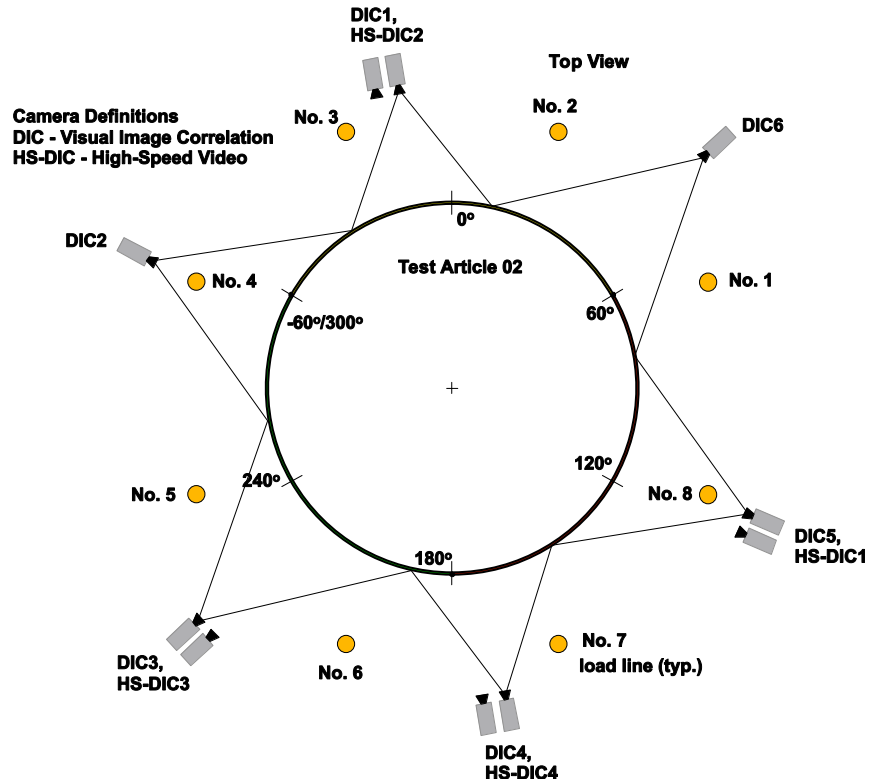
2.5.4 High-Speed Digital Image Correlation (HS-DIC)

Four 3D HS-DIC systems were co-located with four DIC systems as shown in Fig. 2.13 and were used to qualitatively measure the radial displacement response during the cylinder buckling event. The camera setup for LS4, in which maximum compression load was applied at $\theta = 0^\circ$ and where the initiation of buckling was anticipated, is illustrated in Figure 2.13a. The camera setup for LS5, in which maximum compression load was applied at $\theta = 180^\circ$ and where the initiation of buckling was anticipated, is illustrated in Figure 2.13b. Vision Research Phantom 7.1 high-speed digital cameras were used in the HS-DIC systems and recorded images at 10,000 frames per second (fps). HS-DIC1 and HS-DIC3 used a resolution of 512 by 384 and HS-DIC2 and HS-DIC4 used a resolution of 640 by 480 pixels. The cameras were synchronized using an inter-range instrumentation group (IRIG) option and used a manual post-trigger to capture images of the buckling event.

⁵ www.correlatedsolutions.com



a) Camera locations for load sequence 4 (LS4).



b) Camera locations for load sequence 5 (LS5).

Figure 2.13. Location of load lines 1–8 and low-speed DIC and HS-DIC systems.

Displacement data were processed using the 2007 Correlated Solutions VIC-3D™ software and converted into cylindrical coordinates (coordinate system defined Fig. 2.7). It should be noted that some of the HS-DIC data presented herein exhibits slight discontinuities in data values in the regions where adjacent DIC systems overlap. These discontinuities are attributed to system-to-system differences in the measurement error and possible synchronization error between systems. In addition, it is noted, as with the low-speed DIC, that the measurement error typically is greater at the measurement boundaries, i.e., the extreme values of the circumferential location.

The VIC-3D™ session files, all calibration information, and all acquired images have been archived to enable further detailed processing at a later date. The DIC requirements and setup information are presented in more detail in Section 3.0 of Ref. 1. See Appendix A for archival information.

2.5.5 *Load Sequences (LS)*

TA02 was subjected to a total of five loading sequences (LS): three sub-critical LS (i.e., load levels that do not induce test article buckling/failure) and two different LS to buckling. Each LS, described herein, is defined in terms of a percentage of the classical buckling load for the cylinder in compression, P_{cr} , and a percentage of the classical buckling load for the cylinder in bending, M_{cr} , where $P_{cr} = 726,800$ lb and $M_{cr} = 17.4e6$ inch-lb. P_{cr} is the classical linear bifurcation buckling load of a geometrically perfect, uniform cylinder (i.e., uniform geometry and does not include the weld lands) subjected to an axial compression load. The classical buckling bending moment is given by $M_{cr} = \frac{1}{2}P_{cr} \times R$, where R is the OML radius of the cylinder. The load sequences are defined in more detail in the TA02 test plan (Ref. 1) and test procedure (Ref. 2).

The load cases include one uniform axial compression load case and four combined axial compression and bending load cases as follows:

Load Sequence 1: Uniform axial compression to $0.2P_{cr}$

Load Sequence 2: Combined axial compression and bending to $0.2P_{cr} + 0.3M_{cr}$ with maximum compression at $\theta = 0^\circ$

Load Sequence 3: Combined axial compression and bending to $0.2P_{cr} + 0.3M_{cr}$ with maximum compression at $\theta = 180^\circ$

Load Sequence 4: Combined axial compression and bending to failure with load ratio of $1.0P_{cr}:1.5M_{cr}$ and with maximum compression at $\theta = 0^\circ$

Load Sequence 5: Combined axial compression and bending to failure with load ratio of $1.0P_{cr}:1.5M_{cr}$ and with maximum compression at $\theta = 180^\circ$

For the presentation of predicted and measured results in Section 4, it is convenient to define a *total load* associated with the combined axial compression and bending loads as the sum of the applied or measured actuator loads, from analysis or test, for a given combined load state. For the subcritical combined load sequences LS2 and LS3, corresponding to $0.2P_{cr} + 0.3M_{cr}$, the maximum applied total load is 145.4 kips. Similarly, the expected maximum total load for failure load sequences LS4 and LS5, corresponding to $0.4P_{cr} + 0.6M_{cr}$, is 290.7 kips and corresponds to the classical buckling load for this combined load case. This classical buckling load assumes a linear interaction between the axial compression and bending load (see Ref. 5).

Note: LS5 is the second of two LSs to failure that were applied to TA02. It was assumed that any material yielding in the test article that resulted from LS4 would be primarily limited to Panel A and would have minimal influence on the second buckling test, LS5, in which maximum compression would be applied to weld land BC at $\theta = 180^\circ$.

3.0 Analysis Description

Pretest predictions of the buckling response of TA02 were used to determine testing and instrumentation requirements and are presented in this test report for reference. These pretest predictions include many simplifying assumptions and should be viewed as preliminary in nature. Final post-test analysis results will be presented in separate NASA technical publications in which refined modeling and analysis approaches and results will be discussed in detail.

Pretest predictions of the buckling response of TA02 were obtained using the STAGS (STructural Analysis of General Shells) shell-analysis code (Ref. 13). STAGS is a finite-element code developed for the linear and geometrically nonlinear static and dynamic analysis of general shells. The finite-element model included representations of the entire test assembly including the steel load introduction structure, load lines, test article attachment rings, and the test article (see Fig. 3.1). A combination of beam and shell elements was used to generate the model. The standard 410 quadrilateral shell element from the STAGS element library was used in the model and is a four-noded flat facet-type element that is based on the Kirchoff-Love shell hypothesis and the nonlinear Lagrangian strain tensor. The element nodes include three translational degrees of freedom and three rotational degrees of freedom. Large element rotations are accounted for by using a corotational algorithm. The STAGS 210 beam element was also used and is based on the Timoshenko beam theory.

The model was constructed such that the load-introduction fixtures, attachment rings, and TA were separate entities and joined at each interface with multi-point constraints. The load introduction structure was included in the analysis to ensure that the boundary stiffness and kinematics were modeled accurately. The TA02 model included the three longitudinal weld land details. The cylinder skin was modeled with shell elements and beam elements were used to represent the stiffeners. The nominal as-designed TA dimensions were used to define the model. The as-measured initial TA imperfection (Fig. 2.6) was then used to modify the geometrically perfect nominal geometry of the test article mesh to accurately represent the as-built geometrically imperfect TA. Specifically, a user-written subroutine was used to read in the measured geometry of the TA OML and adjust or perturb the OML geometry of the finite-element mesh at each nodal location.

The load was introduced into the structure by applying eight point loads at the ends of beams representing the load lines (depicted by arrows in Fig. 3.1) in the test configuration and the bottom-loading spider was held fixed at its base. The connections between each of the components of the test assembly were assumed to be perfect, that is, the bolted connections were assumed to be uniform rigid attachments with no relative movement between each component.

Al-Li 2195-T8M4 plate material properties from MSFC-HDBK-3513 (Ref. 14) were used in the analysis and included an elastic modulus of 11.0 GPa, a Poisson's ratio of 0.33, and a density of 0.098 lbm/in³. Material data obtained from Ref. 14 indicates that the material exhibits slight differences in the longitudinal and transverse stiffness properties but this was not considered

during the preliminary test article design and analysis. A36 steel properties were used for all the test fixture components and included an elastic modulus of 29.0 Msi, a Poisson ratio of 0.26, density of 0.28 lb/in³.

Geometrically nonlinear analyses of the imperfect TA were used to predict the prebuckling, buckling and initial post-buckling response of the TA presented herein. The predicted buckling total loads for LS4 and LS5 are 258.1 kips (88.8% classical buckling load) and 268.0 kips (92.2% classical buckling load), respectively.

Detailed modeling information and results are presented in Refs. 4 and 15.

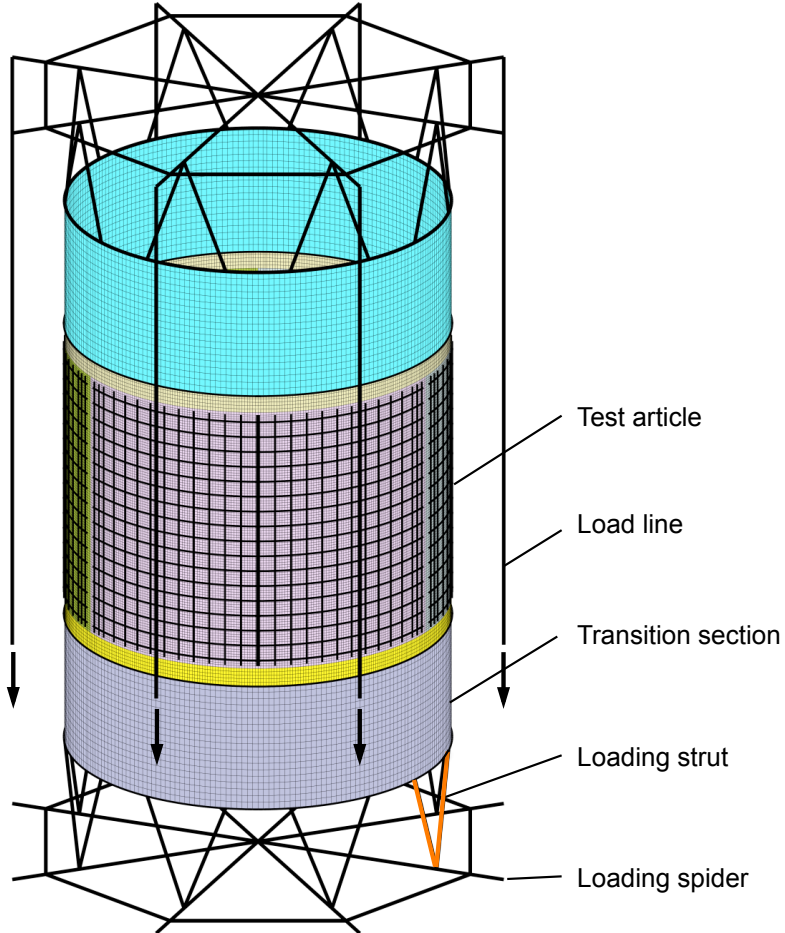


Figure 3.1. Finite-element model of test assembly.

4.0 Results and Discussion

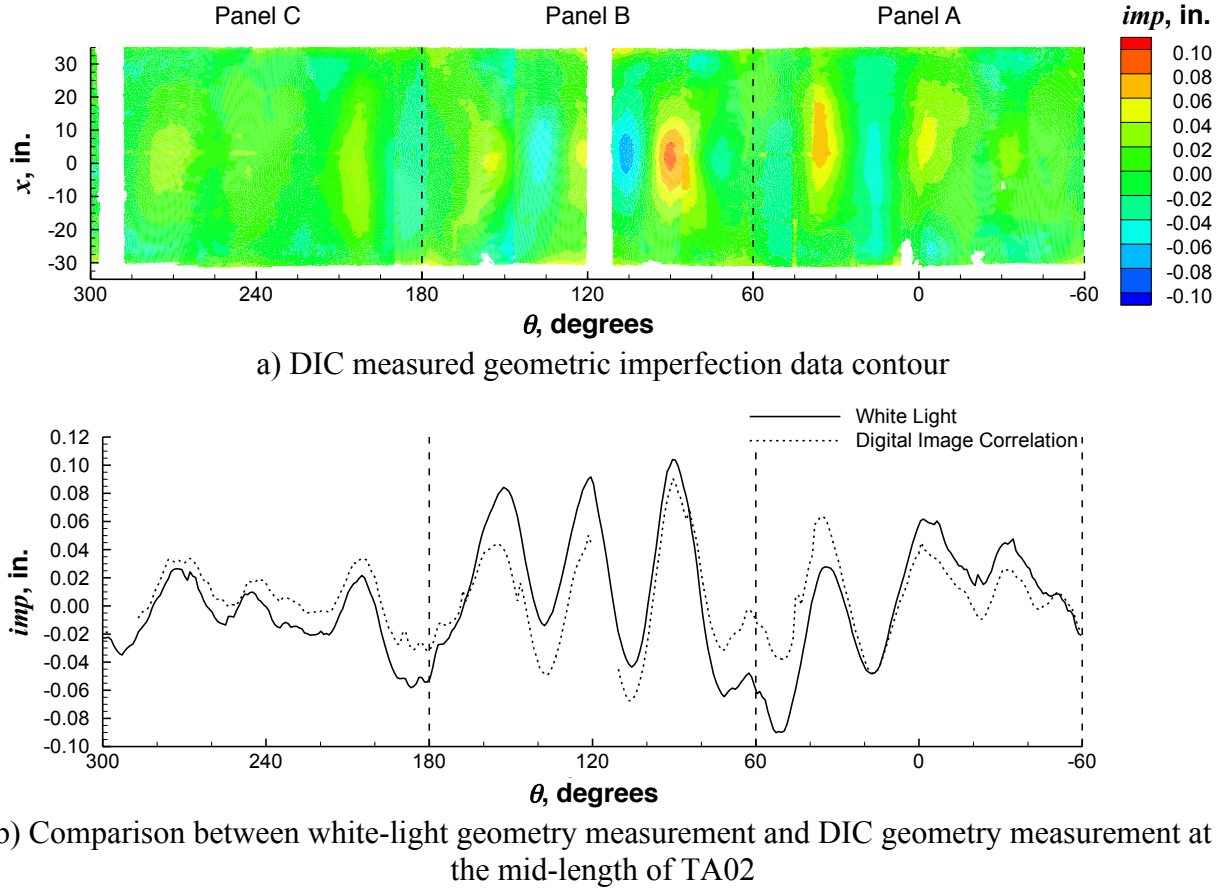
Results from the testing of TA02 are presented in this section. First, geometric imperfection data obtained from the DIC system is presented and compared to the photogrammetry/white-light geometry measurement in Section 4.1. Then selected results from LS4 and LS5 are presented and compared to pretest predictions in Sections 4.2. and 4.3, respectively. The test results include, load versus end-shortening, and load versus radial displacement response curves. Then low-speed DIC and HS-DIC data are presented for selected prebuckling, buckling, and postbuckling load levels. Finally, load versus strain response curves are presented along with plots of the axial

strain distribution around the circumference of the test article for selected prebuckling load levels and incipient buckling.

4.1 Initial Geometric Imperfection Data

The initial OML geometry of TA02 was measured prior to its installation into the test facility by using a photogrammetry/white-light metrology technique as described in Section 2.3. The measurement accuracy was ± 0.001 inches. The deviation of the measured data from a best-fit cylinder was calculated and defined as the initial geometric imperfection (*imp*) and is shown in Fig. 2.6. The three longitudinal weld lands are located at -60° , 60° , and 180° . The measured data indicate that TA02 was for the most part circular to within ± 0.10 inches with some additional deviations near the upper and lower boundaries.

The OML geometry of TA02 was measured a second time after it was installed in the test facility using DIC, immediately prior to testing and is shown in Fig. 4.1a. The DIC measurements were used to determine if the geometric imperfection of TA02 had changed during handling and installation into the test fixtures as compared to the corresponding white-light/photogrammetry measurement shown in Fig. 2.6. Circumferential traces of the initial geometric imperfection at the mid-length of TA02 based on the white-light measurement and the DIC measurement are compared in Figure 4.1b. The DIC-based imperfection measurement shares similar characteristics to the high-resolution white-light/photogrammetry measurement including the circumferential periodic variation in the imperfection. However, the data appear to indicate a slight difference in the geometry with a maximum difference of approximately 0.044 inches at the AB weld land ($\theta = 60^\circ$).



a) DIC measured geometric imperfection data contour

b) Comparison between white-light geometry measurement and DIC geometry measurement at the mid-length of TA02

Figure 4.1. Geometric imperfection data for TA02 from DIC measurement prior to LS4 load application.

4.2 Buckling Response of TA02-LS4: Combined Axial Compression and Bending Loads with Maximum Compression over the Center of Panel A

Selected test results are presented to illustrate the overall buckling response of TA02 subjected to combined axial compression and bending, and are compared to pretest predictions. The loading of the cylinder is defined in the LCS such that an axial-compression-to-bending-load ratio of $1.0P_{cr}:1.5M_{cr}$ is maintained throughout the test. The bending component of the loading in LS4 induces a maximum compression load at the center of Panel A ($\theta = 0^\circ$) in the TA. TA02 will be referred to as TA02-LS4 when describing results from LS4 so as to distinguish them from results from other load cases.

4.2.1 Load versus Displacement Response

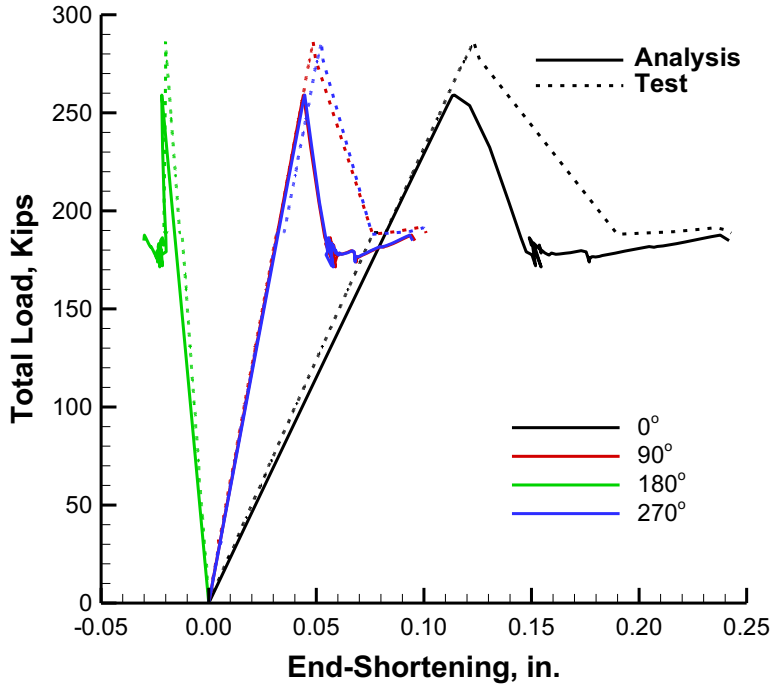
Predicted and measured total load versus end-shortening response curves for TA02-LS4 are shown in Fig. 4.2 and are indicated by the solid and dashed curves, respectively. First, total load versus end-shortening response curves associated with $\theta = 0^\circ$, 90° , 180° , and 270° locations are presented in Fig. 4.2a as black, red, green, and blue curves, respectively. The corresponding total load versus average end-shortening response curves are shown in Fig. 4.2b. The total load is defined as the sum of the eight load line loads (see Section 2.5.5), the end-shortening displacements correspond to the relative axial displacement between upper and lower attachment

rings (see Section 2.5.2), and the average end-shortening is the average of the end-shortening displacements from the 0°, 90°, 180°, and 270° locations. (Note: negative end-shortening corresponds to elongation of the test article.)

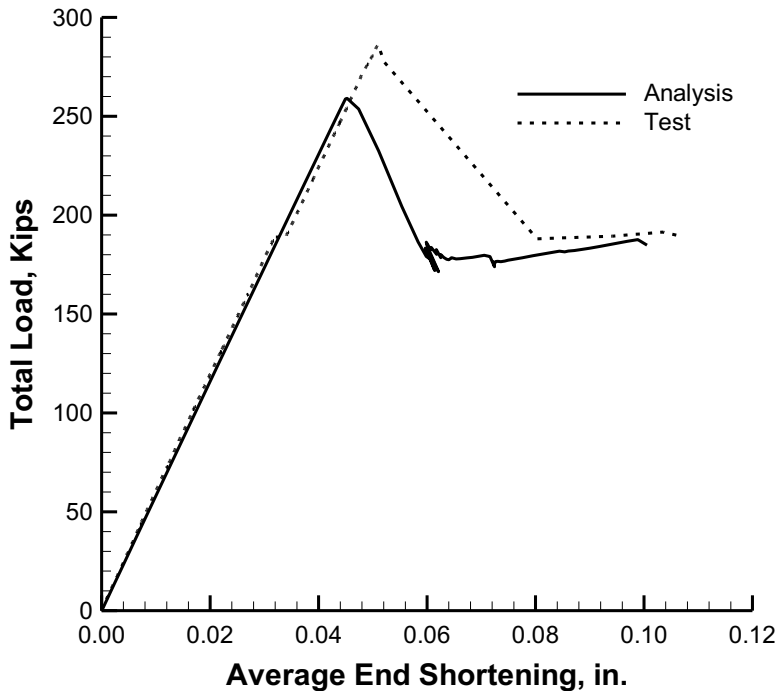
A linear prebuckling response is predicted for TA02-LS4 up to a maximum total load of 258.1 kips (88.8% of the classical buckling load for LS4). The measured response is linear up to a load of approximately 190.0 kips, and there the response indicates a slight increase in the average end-shortening. After that nearly instantaneous increase in average end-shortening, the measured response is linear up to a maximum total load of 286.2 kips (98.4% of the classical buckling load for LS4). The loading anomaly observed at 190 kips was accompanied by an audible popping noise during the test and is attributed to the slight movement or settling of the test article in the potting of the attachment ring. This type of settling behavior had been observed in previous testing of TA01 and TA02 and was not unexpected. Additional evidence of this settling is shown in other data presented in subsequent sections.

The maximum load is followed by the buckling of TA02-LS4 and is characterized by a sudden reduction in the axial load of approximately 35% to a postbuckling load of 188.2 kips. In addition, the measured load-shortening response curve indicates a significant increase in the average end-shortening displacement during the buckling response from 0.052 inches to 0.08 inches. This increase in average end-shortening is associated with the release of (reduction in) elastic strain energy in the test fixtures in the postbuckling range of loading which imparts a sudden increase in end shortening (spring back). A similar load versus end-shortening behavior was also observed during the transient collapse response of TA01. Note that the oscillation of the predicted axial load in the initial postbuckling range is attributed to the structural damping parameters used in the finite-element simulation.

Overall, the character of the load versus end-shortening response is predicted well, including the prebuckling and postbuckling axial stiffness; however, the predicted maximum total load of 258.1 kips is approximately 10% lower than the measured maximum total load of 286.2 kips. A similar difference was observed in the test and analysis correlation of TA01 as reported in Ref. 3.



a) Total load versus end-shortening response at four circumferential locations.



b) Total load versus average end-shortening response.

Figure 4.2. Measured and predicted load versus end-shortening response of TA02-LS4 subjected to combined axial compression and bending.

Predicted and measured prebuckling load versus radial displacement response curves at the center of each panel and the center of each weld land are presented in Figs. 4.3 and 4.4, respectively. Positive displacements correspond to outward radial displacements. Panels A, B,

and C are shown as black, red, and green curves, respectively, and weld lands AB, BC, and CA are shown as black, red, and green curves, respectively. The buckling and postbuckling data are omitted from these figures so that the small-magnitude prebuckling displacements could be seen more clearly.

The measured results indicate that the centers of Panel A, weld lands AB, and CA move radially outward during the prebuckling response with a maximum displacement of approximately 0.063 inches at the center of Panel A. In contrast, the centers of weld land BC and panels B and C move slightly inward with a maximum inward displacement of -0.024 inches at the center of weld land BC. The predicted results indicate similar response trends overall; however, the maximum prebuckling displacement at the center of Panel A is predicted to be 0.073 inches, which is 16% greater than the corresponding measured displacement. It is noted that the measured data indicate a discontinuous change in the radial displacement at 190 kips, and corresponds to the same discontinuity observed in the end-shortening measurement shown in Fig. 4.2. The discontinuity in the displacement response is seen in all the radial displacement measurements and is attributed to an apparent shift or settling of the TA02 in the attachment rings, as discussed earlier.

Predicted and measured prebuckling, buckling, and postbuckling radial displacement response curves for the center of Panel A and at the center of weld lands AB and CA are shown in Fig. 4.5 to illustrate the displacement response characteristics during the buckling event and in the postbuckling range of loading. Buckling, initial postbuckling, and deep postbuckling (end of test) points are indicated on the curves with filled and open square, circle, and triangle symbols, respectively. Open symbols are measured results and filled symbols are predictions. The results indicate a sudden reversal in the displacements at weld lands CA and AB from radially outward at buckling (square symbols) to radially inward at initial postbuckling (circle symbols). In contrast, the center of Panel A deforms outward. Upon further loading into the postbuckling range, the predicted inward radial displacements at the weld lands increase with a maximum measured displacement of -2.3 inches occurring at the AB weld land.

Overall, the predicted response trends correlate well with the measured results. However, the predicted prebuckling displacements are, in many cases, slightly larger in magnitude than the corresponding measured displacements. A similar result was also observed in TA01 (Ref. 3).

A photo of the buckled TA is shown in Fig. 4.6 and shows some of the initial postbuckling deformations in Panel A near the lower attachment ring. Measured and predicted full-field displacement contours are presented and compared in the next section and illustrate the prebuckling, buckling, and postbuckling displacement response in more detail.

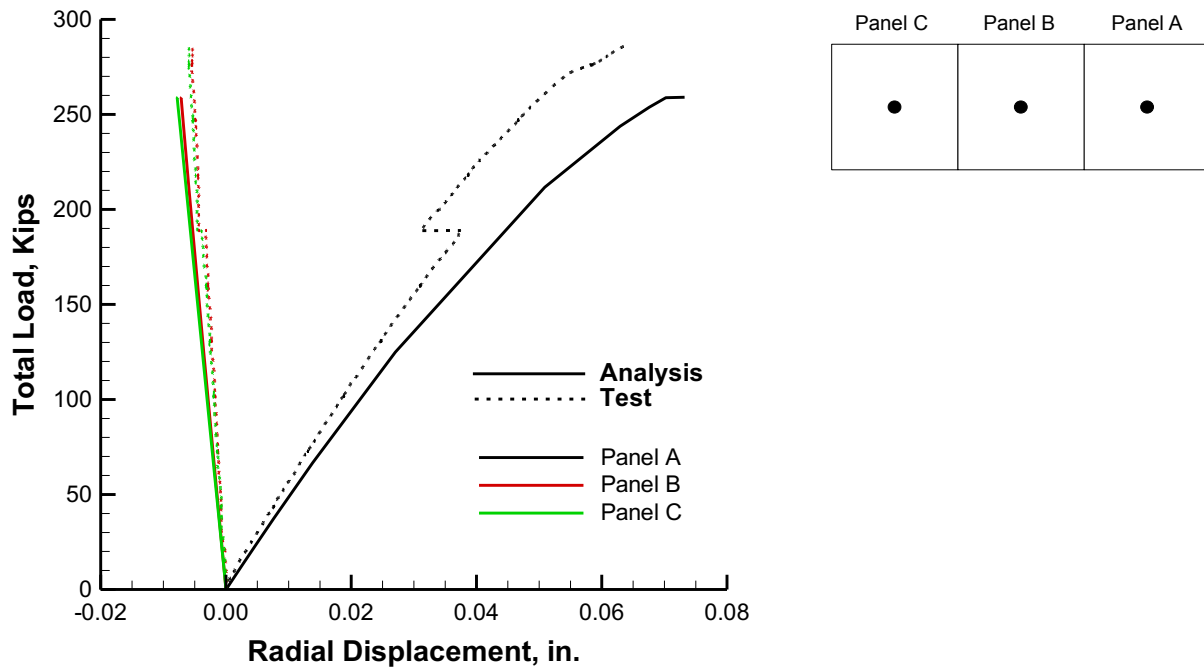


Figure 4.3. Measured and predicted prebuckling load versus radial displacement response of TA02-LS4 at the center of each panel.

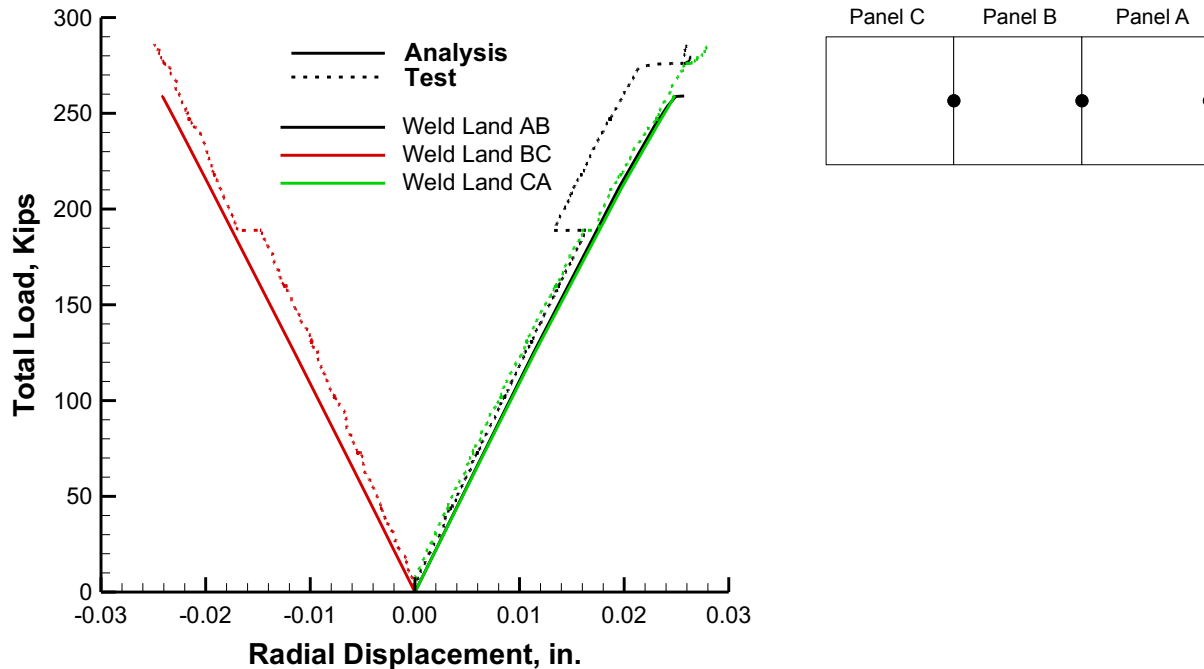


Figure 4.4. Measured and predicted prebuckling load versus radial displacement response of TA02-LS4 at the center of each longitudinal weld land.

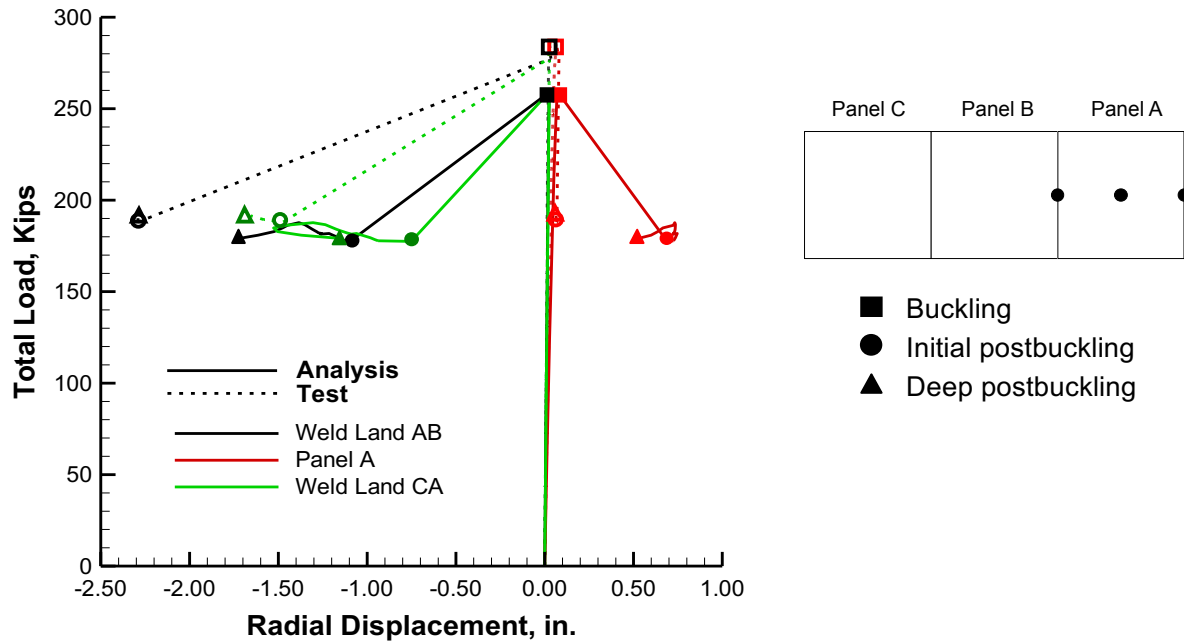


Figure 4.5. Measured and predicted load versus radial displacement response of TA02-LS4 at the center of Panel A and at the center of weld lands AB and CA including the buckling and postbuckling response.

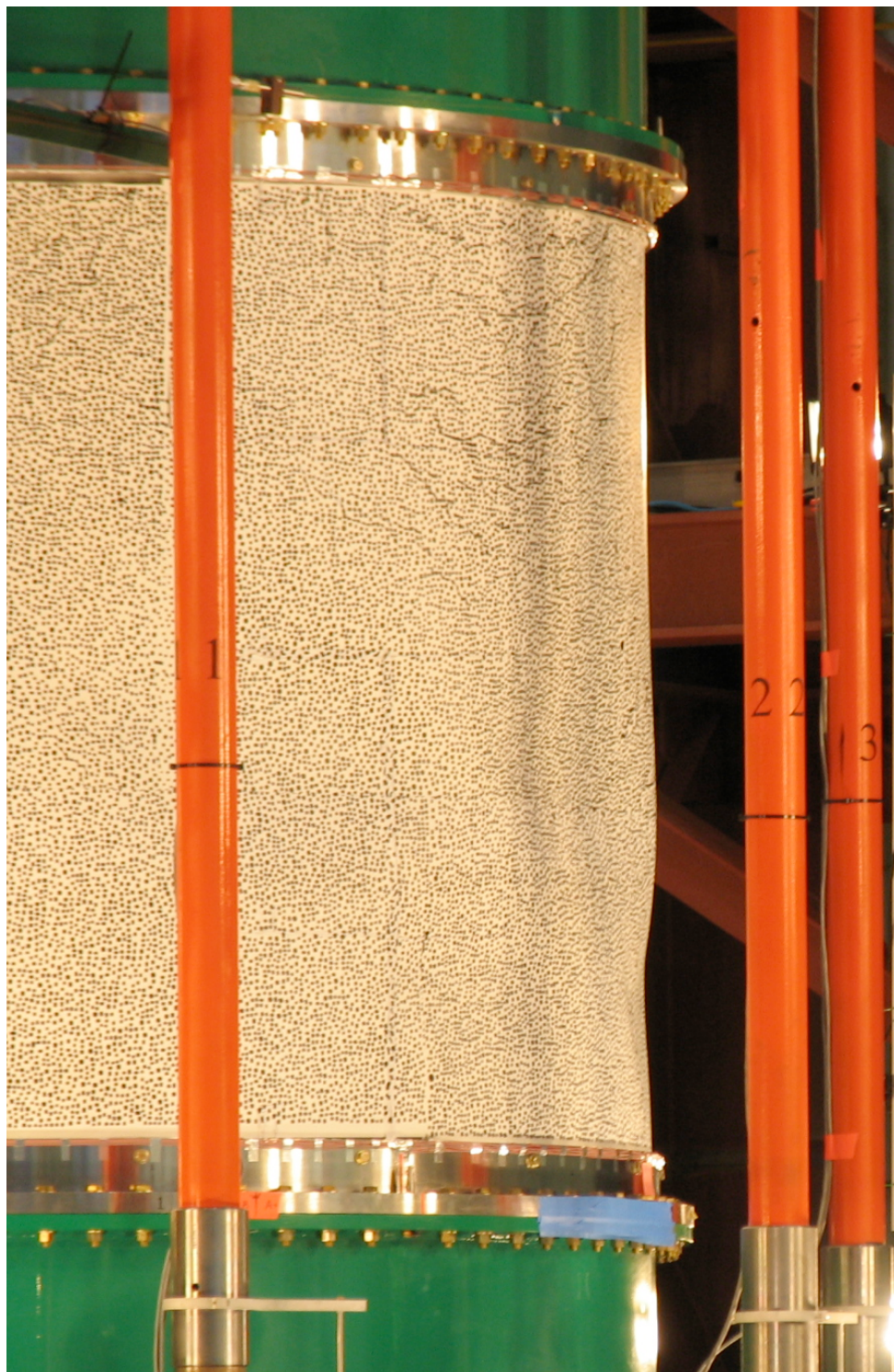


Figure 4.6. TA02-LS4 after buckling.

4.2.2 Full-Field Displacement Contours

Predicted and measured full-field prebuckling, buckling, and postbuckling displacement contours are presented in this section. First, selected axial and radial full-field displacement contours obtained from low-speed DIC systems are presented and compared to initial pretest predictions. Then, HS-DIC displacement contours obtained during the collapse response of the test article are presented. The displacement contours are plotted as a function of axial, x , and circumferential, θ , coordinates defined in Fig. 2.7. The dashed vertical lines shown in the contour plots at -60° , 60° and 180° correspond to weld lands CA, AB and BC, respectively. Finally, measured radial displacement versus time response curves are presented that illustrate the transient deformation response of the test article during collapse

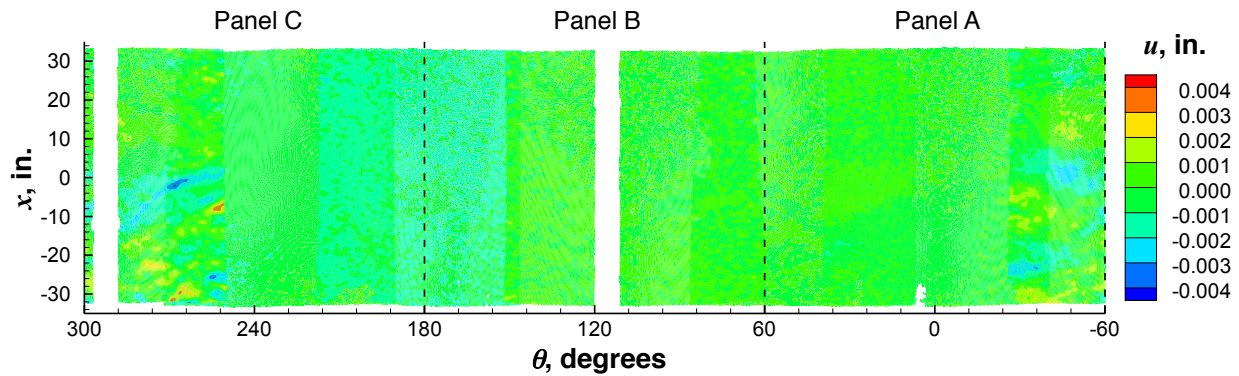
Low-Speed DIC Displacement Measurements

An estimate of the low-speed DIC measurement noise for the axial, u , and radial, w , displacement measurements is presented in Figs. 4.7a and 4.7b, respectively. The results indicate measurement noise of approximately ± 0.004 inches in the axial displacements and ± 0.010 inches in the radial displacements. These levels of noise are typical for this type of DIC system, set-up parameters and calibration method used. Note: data are missing in two locations around the circumference of the test article due to load lines obstructing the FOV and appear as white vertical stripes in the figures.

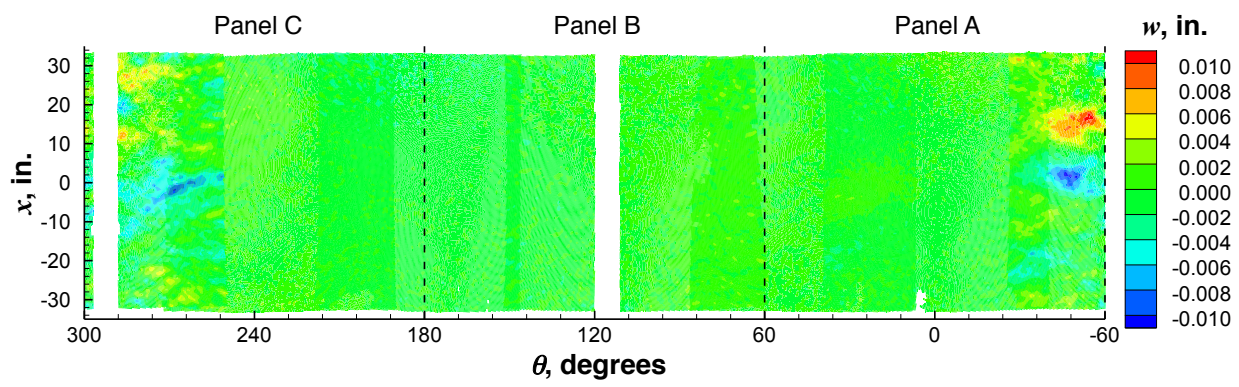
Selected axial u and radial w displacement contours are presented in Figs. 4.8 through 4.13 and include predicted and measured results from three prebuckling load levels and one postbuckling load level. Prebuckling u and w displacements at 72.7 kips (25% of the classical buckling load) are shown in Figs. 4.8 and 4.9, respectively. The predicted u displacements indicate a nonuniform end displacement distribution on the top edge of TA02-LS4 with maximum axial displacement u of -0.034 inches at $\theta = 0^\circ$ in Panel A and a u displacement of 0.006 inches at $\theta = 180^\circ$ at weld land BC. This u displacement distribution is consistent with the applied combined axial compression and bending loads. Overall, the corresponding measured displacements show a similar distribution. However, some localized variation is observed in the measured data and is attributed to the inherent measurement noise shown in Fig. 4.7a. The predicted w displacements, shown in Fig. 4.9a, indicate the development of a periodic variation in the radial deformations within Panel A and are characterized by seven circumferential half-waves that span from -60° to $+60^\circ$. Maximum outward displacements of 0.020 inches occur at the top of Panel A and are associated with the applied bending load that causes the top portion of the cylinder to translate out of plane. The corresponding measured displacements are shown in Fig. 4.9b and indicate a similar response.

Predicted and measured radial displacement contours at 159.9 kips (55% of the classical buckling load) are shown in Figs. 4.10a and 4.10b, respectively. Overall, the contour patterns are similar to those observed at the lower load levels. It should be noted that a discontinuity appears in the measured displacements at $\theta = 145^\circ$ (Fig. 4.10b) and is likely due to differences measurement error from system to system as described in Section 2.5.3. The predicted and measured u displacement distributions at this load level (not presented herein) are similar to those presented in Fig. 4.8.

As the applied load increases up to the buckling load of the test article, both the predicted and measured radial displacement contours indicate the development of a single ellipse-shaped dimple near the bottom of Panel A as shown in Fig. 4.11. The amplitude of the inward dimple, incipient to buckling, is 0.043 inches and 0.025 inches in the predicted and measured data, respectively. The buckling response of TA02-LS4 initiates at this single dimple and is characterized by the rapid development of additional buckles throughout Panel A and at weld lands AB and CA (as shown in Fig. 4.12) and a significant reduction in total load (as shown in Fig. 4.2). The predicted initial postbuckling displacements exhibit a series of four large inward buckles at the mid-length of the panel and several smaller buckles near the lower attachment ring. The maximum amplitude displacements are predicted to occur in the acreage of Panel A and are approximately -1.75 inches. The measured buckling displacements also exhibit a similar distribution of buckles; however, the buckles are slightly offset towards the bottom of the cylinder and the maximum amplitude displacements occur at weld land AB and weld land CA. This difference in behavior is attributed to the use of linear elastic material properties in the finite-element model that cannot account for the material yielding that occurred in the test article. More specifically, the predicted transient buckling response (results not presented herein) exhibited a displacement pattern similar to the one observed in Fig. 4.12b near the bottom edge of the TA during the initial stages of the transient buckling response. As the transient buckling continued, these small buckles were predicted to move towards the mid-length of the TA as shown in Fig. 4.12a. However, it is likely that the test article experienced material yielding in regions of large magnitude strains associated with the short-wavelength buckles that develop during the early stages of buckling (see HS-DIC results in next section), which may have prohibited the movement of these buckles. Post-test inspection of the test article indicated permanent deformations associated with material yielding in the areas of large bending gradients as shown in Fig. 4.13.

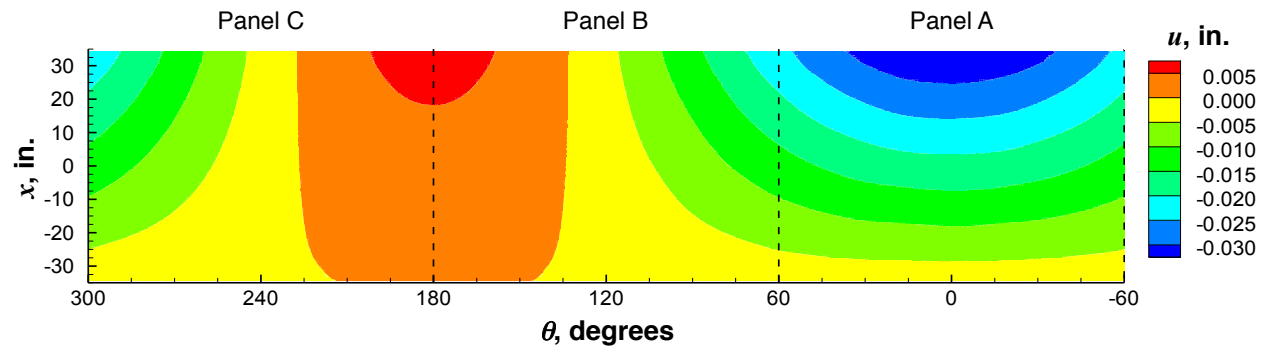


a) Axial displacement u .

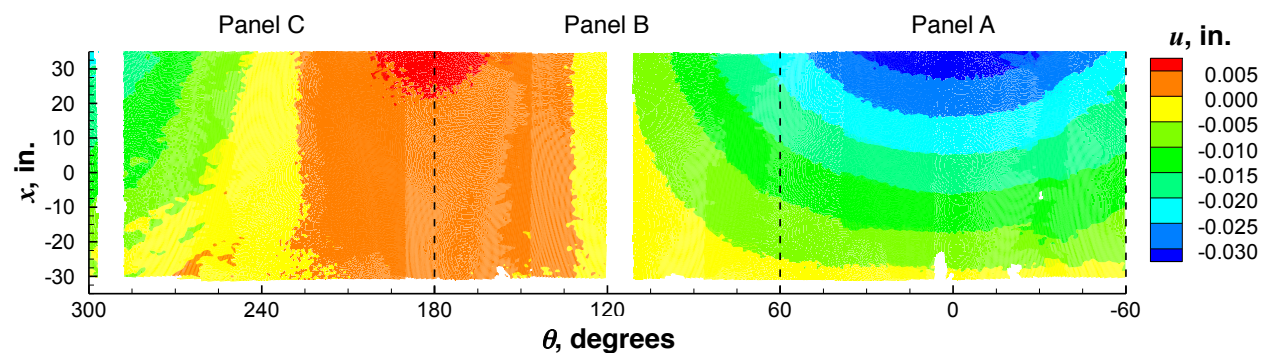


b) Radial displacement w .

Figure 4.7. DIC noise signature for u and w displacement measurements prior to TA02-LS4 test.

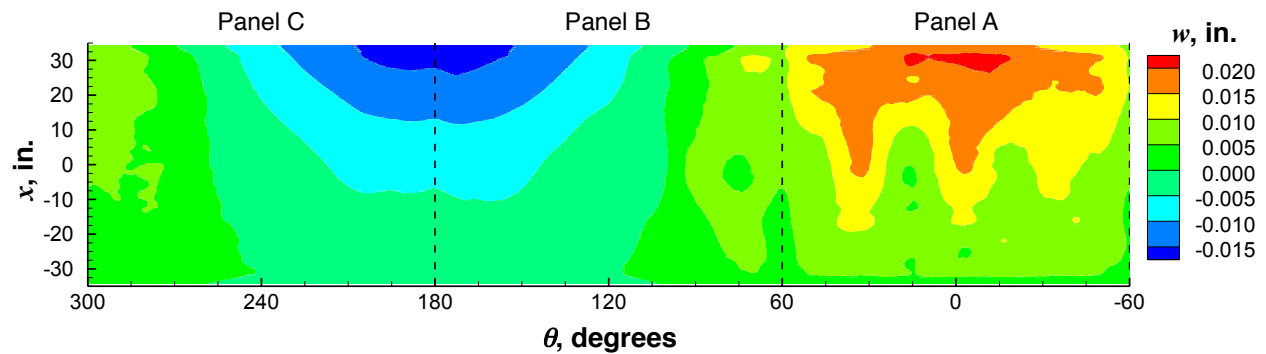


a) Finite-element prediction.

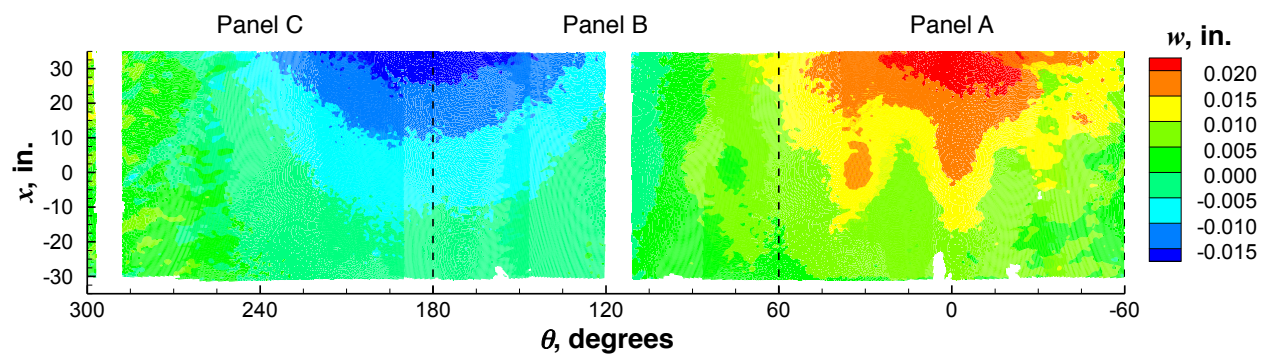


b) DIC.

Figure 4.8. Predicted and measured axial displacement (u) contours at 72.7 kips total load (25% classical buckling load).

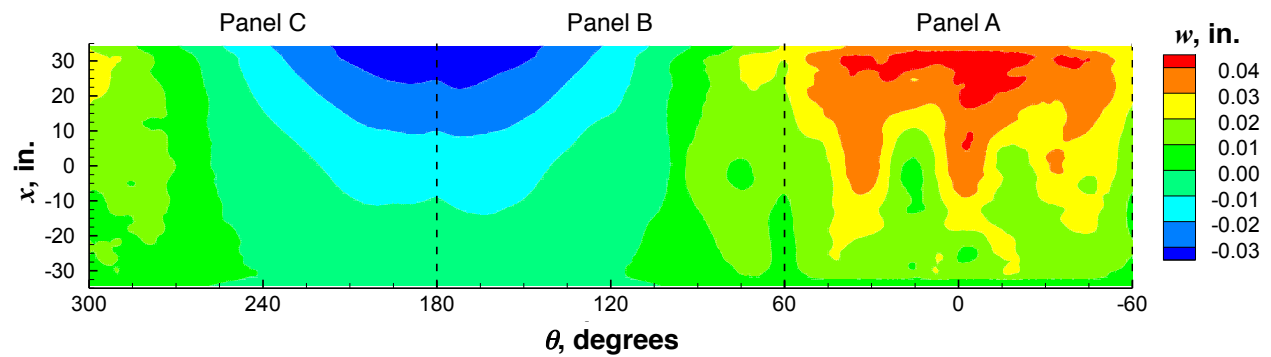


a) Finite-element prediction.

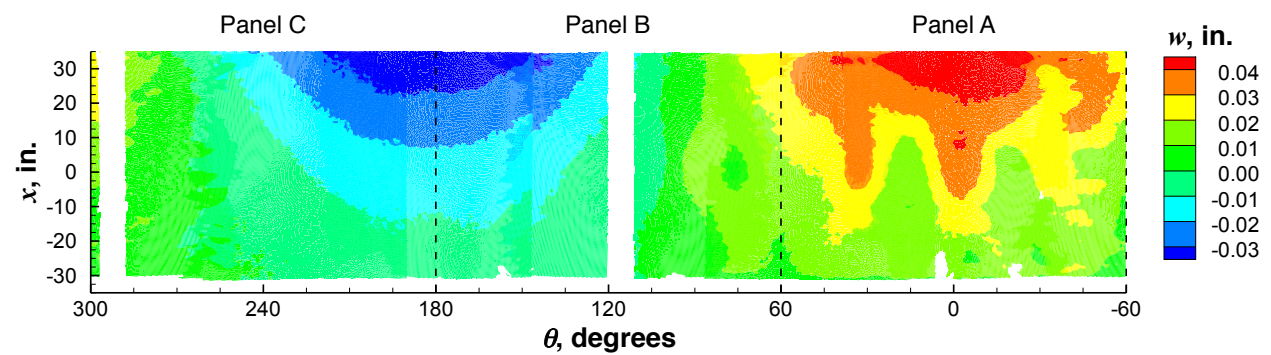


b) DIC.

Figure 4.9. Predicted and measured radial displacement (w) contours at 72.7 kips total load (25% classical buckling load).

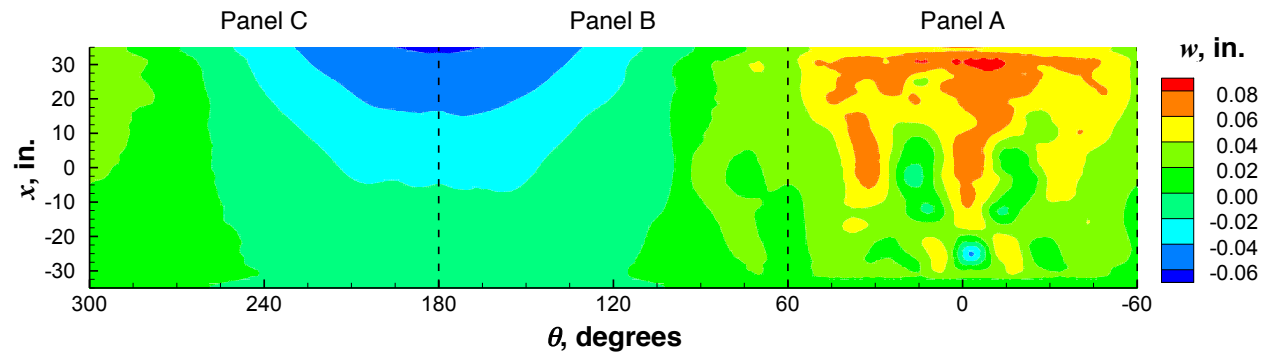


a) Finite-element prediction.

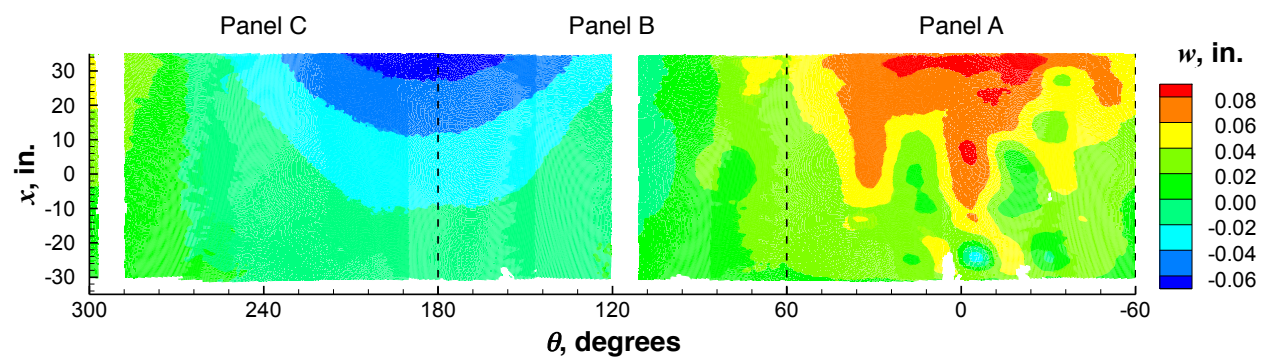


b) DIC.

Figure 4.10. Predicted and measured radial displacement (w) contours at 159.9 kips (55% classical buckling load).

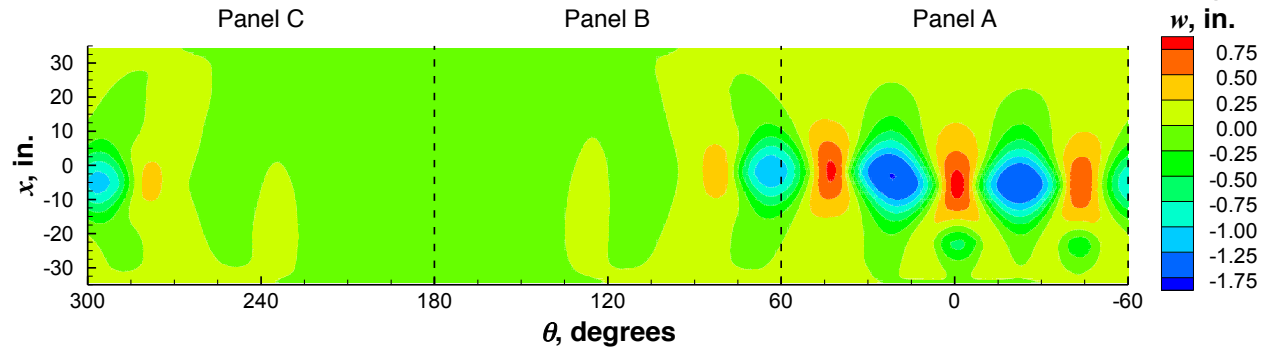


a) Finite-element prediction at buckling load of 258.1 kips (88.8% classical buckling load).

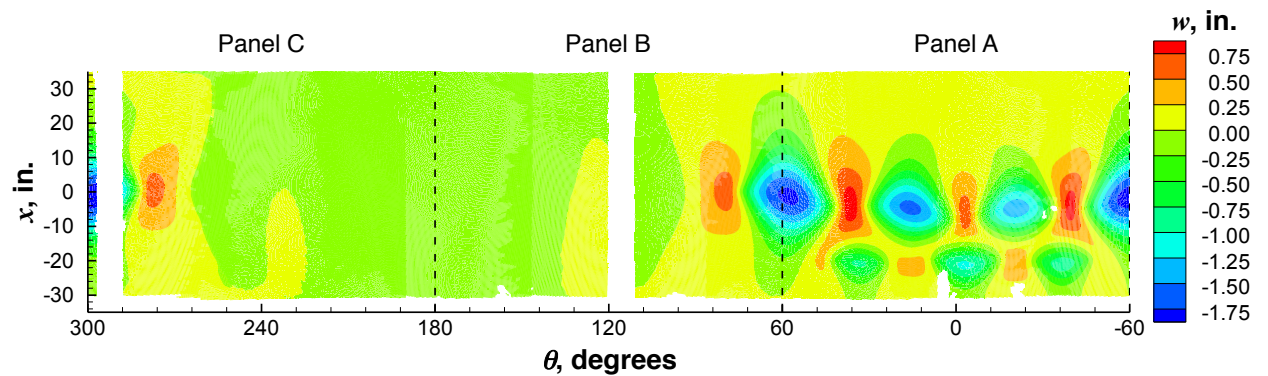


b) DIC at buckling load of 286.7 kips (98.6% classical buckling load).

Figure 4.11. Predicted and measured radial displacement (w) contours incipient to buckling.



a) Finite-element prediction at initial postbuckling load of 177.0 kips.



b) DIC at initial postbuckling load of 188.2 kips.

Figure 4.12. Predicted and measured initial postbuckling radial displacement (w) contours.

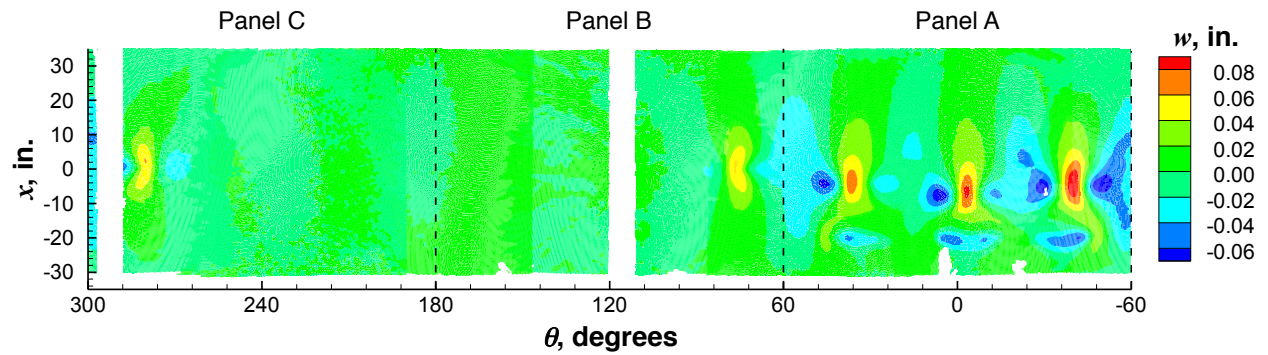


Figure 4.13. Measured post-test radial displacement (w) contours showing permanent deformations in the cylinder wall.

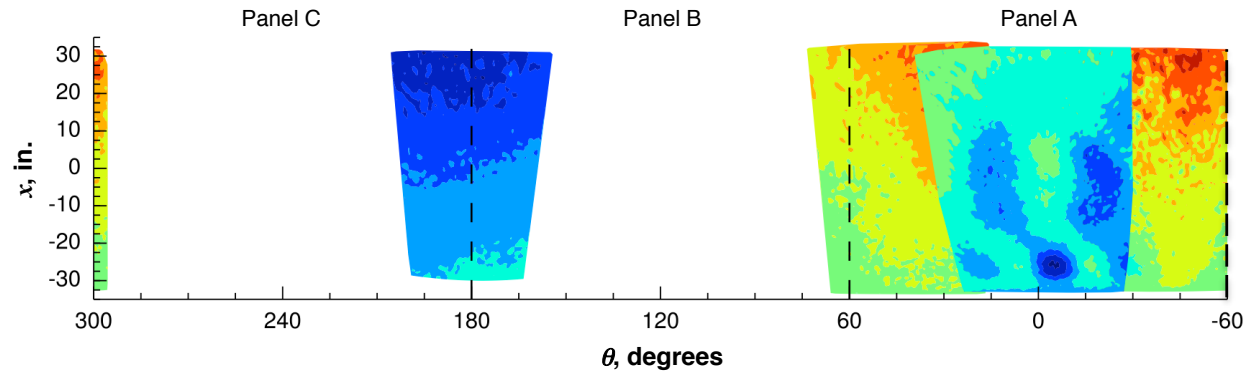
HS-DIC Displacement Measurements

Selected radial displacement contours obtained from HS-DIC systems are presented to illustrate the unstable transient buckling response of the test article in Figs. 4.14a through 4.14e (i.e., show the progression of the deformation response that occurred between the radial displacement incipient to buckling, shown in Fig. 4.11b, and the initial postbuckling radial

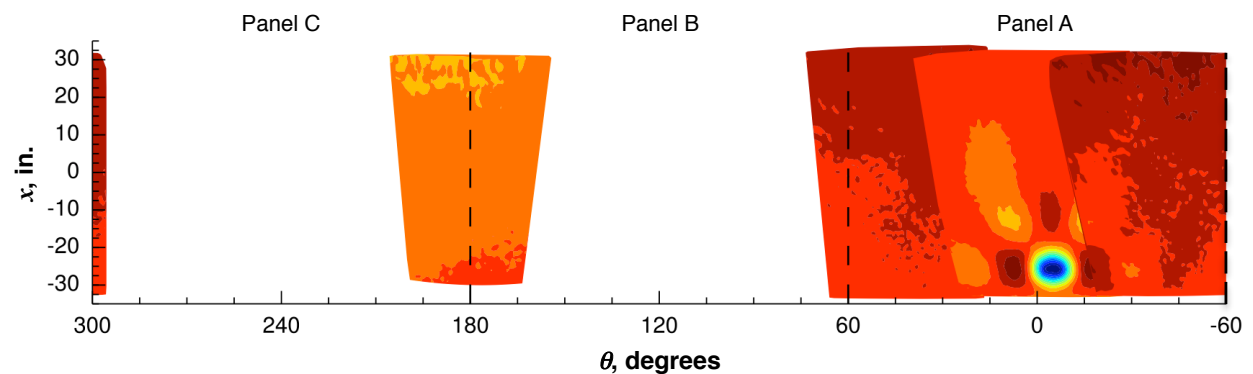
displacement response, shown in Fig. 4.12b). Four 3D HS-DIC systems were set up around the circumference of the test article and captured images at 10,000 fps (see Fig. 2.13a for camera locations). Three of the four HS-DIC systems were used to characterize the deformation response of Panel A from -60° to 60° around the circumference of TA02-LS4. The fourth system was used to gather images of weld land BC from 165° to 195° around the circumference. The blue and green contours represent inward radial deformations and the yellow and red contours represent outward radial deformations. Note, displacement values are omitted due to uncertainty in their accuracy, however, it is expected that the contours do provide an accurate qualitative indication of the buckling behavior.

Incipient buckling contours are shown for $t = 0.000$ seconds⁶ in Fig. 4.14a and shows an initial ellipse-shaped dimple at the bottom of Panel A, as was observed in the corresponding low-speed DIC measurement shown in Fig. 4.11b. (Note: the discontinuities in the displacement measurements of the three overlapping HS-DIC systems are attributed to a difference in system to system measurement error and possibly a synchronization error between the systems as described in Section 2.5.4.) At time $t = 0.010$ seconds, the initial dimple becomes more distinct and additional small dimples develop in the bottom half of Panel A between -30° to 30° as shown in Fig. 4.14b. As the collapse response continues, additional buckles form and propagate throughout Panel A as shown in Figs. 4.14c (time $t = 0.014$ seconds) and 4.14d (time $t = 0.020$ seconds) until a fully developed postbuckling configuration is obtained as shown in Fig. 4.14e at time $t = 0.030$ seconds and Fig. 4.14-f at time $t = 0.300$ seconds. The measured HS-DIC postbuckling displacement patterns correlate well with the corresponding low-speed DIC contours presented in Fig. 4.12b and are characterized by seven circumferential half-waves between -60° to 60° at the mid-length of the cylinder.

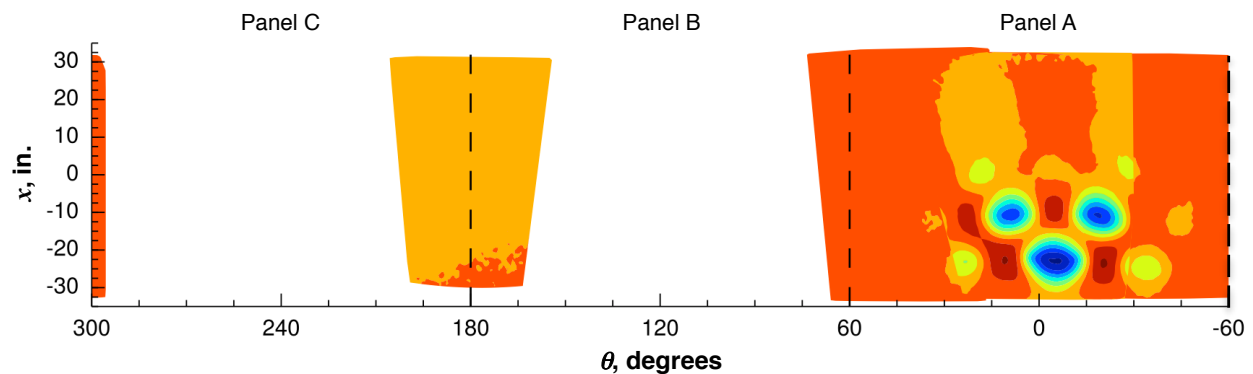
⁶ Note: $t = 0.000$ seconds is an arbitrary time reference used to determine relative time throughout the transient collapse response.



a) Incipient buckling $t = 0.000$ seconds.

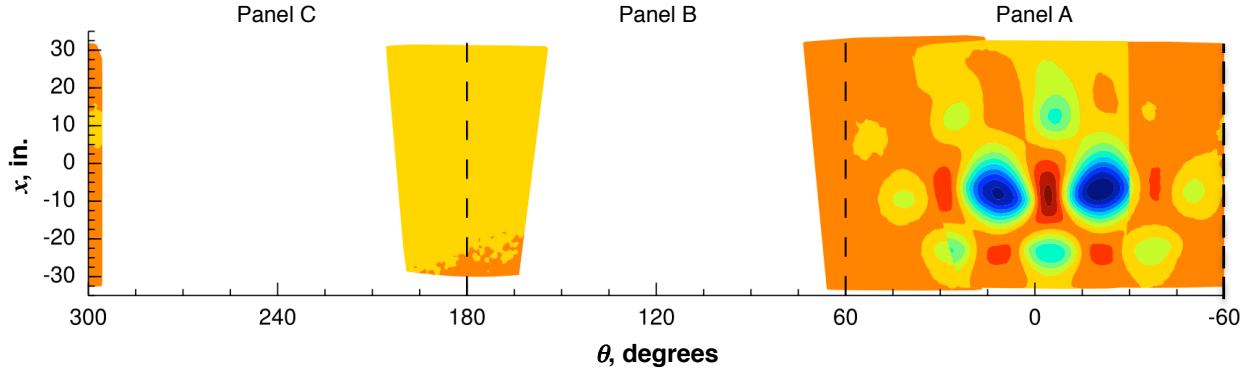


b) Initial buckling $t = 0.010$ seconds.

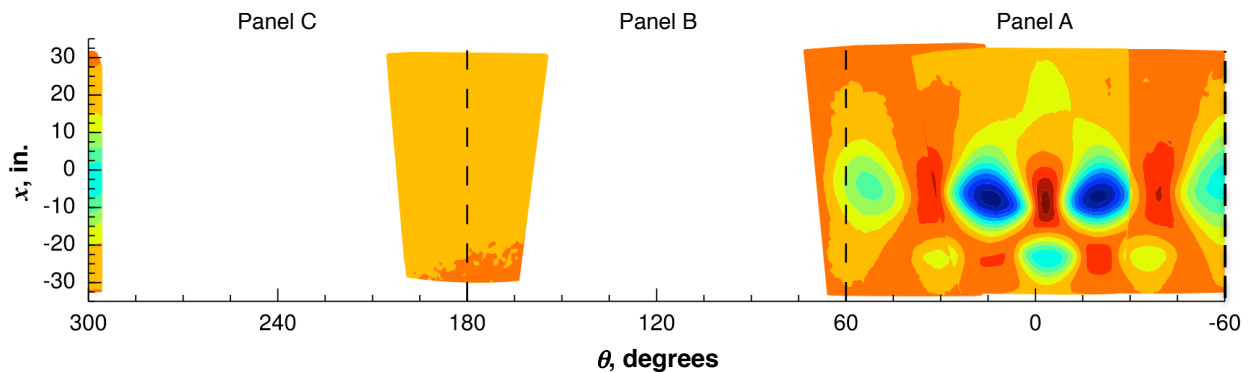


c) Buckling $t = 0.014$ seconds.

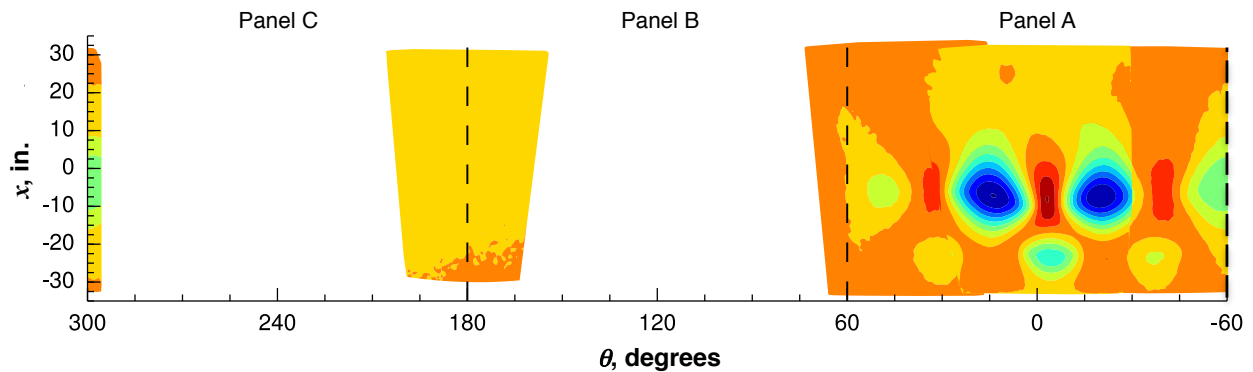
Figure 4.14. HS-DIC results illustrating the initiation and propagation of buckling deformations in TA02-LS4.



d) Buckling $t = 0.020$ seconds.



e) Buckling $t = 0.030$ seconds.



f) Buckling $t = 0.300$ seconds.

Figure 4.14. Concluded.

4.2.3 Load versus Axial Strain Response

Predicted and measured prebuckling load versus axial strain response curves are presented in Figs. 4.15 through 4.21. Predicted results are represented by solid lines, and the measured results by dashed lines. Negative strains correspond to compression. The buckling and postbuckling strains have been omitted from the figures so that small-magnitude prebuckling strains can be easily observed. In the figures, a gage is referred to by its location, e.g., a gage on the cylinder OML at a location where there is an internal stiffener, is referred to as an OML stiffener gage. In addition, schematics of strain gage locations are provided in each figure and include an IML view indicating the general gage locations and a cross-section view to illustrate the specific

location of the gages on the skin or stiffener. It should be noted that the stiffener gages are located either on one side of the stiffener (e.g., thin stiffeners in the acreage) or on top of the stiffener (e.g., thick stiffeners near weld lands) and indicate in the cross-section view. The objective of this strain data comparison is to help assess the accuracy of the predicted local response characteristics of the skin and stiffeners at various locations around the cylinder. First, back-to-back strain gage results from skin pockets and longitudinal stiffeners near the centers of panels A, B, and C, are shown in Figs. 4.15, 4.16, and 4.17, respectively. Similar results from weld lands and adjacent longitudinal stiffeners for weld lands AB, BC and CA, are presented in Figs. 4.18, 4.19 and 4.20, respectively. Finally, strain gage results from two different locations near the buckling initiation sight in Panel A are shown in Fig. 4.22.

Back-to-back strain gage results from skin pockets and longitudinal stiffeners near the centers of panels A, B, and C, are shown in Figs. 4.15, 4.16, and 4.17, respectively. Each figure contains predicted and measured results from strain gages at the center of a skin pocket near the center of each panel, corresponding to the black and red lines for the OML and IML gages, respectively; and results from strain gages on the longitudinal stiffeners adjacent to each of these skin pockets, corresponding to the green and blue lines for the OML and IML gages, respectively. The combined axial compression and bending loads applied in LS4 cause the maximum strains to occur near the center of Panel A and lower strains in the other panels, as expected. The measured results for Panel A indicate that the strain response is, for the most part, linear up to buckling with strains that range from $-1550 \mu\epsilon$ to $-1675 \mu\epsilon$. A slight amount of bending in the shell wall is observed as indicated by the divergent load versus strain response curves for the OML (029OSA) and IML (084ISA) skin gages. The strains at the center of panels B and C are significantly lower than those in Panel A and range from approximately $-150 \mu\epsilon$ to $-250 \mu\epsilon$. The lower strains are expected because the centers of panels B and C are on the opposite side of the bending axis from Panel A and thus are at locations where the bending moment is relieving some of the axial compressive load.

The discontinuity near 190 kips that was described in Section 4.2.1 for the load versus end-shortening response can also be seen in the strain responses. On average, the axial compression strains in panels A and C increase by $50 \mu\epsilon$ (4% change) and by $15 \mu\epsilon$ (1.2% change), respectively, while the compression strains in Panel B decrease by $-25 \mu\epsilon$ (2% change). As stated in Section 4.2.1, this event was accompanied by an audible popping noise during the test and is attributed to the slight movement or settling of the test article in the potting of the attachment ring. The strains appear to continue along a similar slope after the event and suggest that the overall TA response was unaffected.

Back-to-back strain gage results from weld lands AB, BC and CA and from longitudinal stiffeners adjacent to the weld lands, are shown in Figs. 4.18, 4.19, and 4.20, respectively. Each figure contains analysis and test results from the center of each weld land, corresponding to the black and red lines for the OML and IML gages, respectively; and results from longitudinal stiffeners adjacent to each of the weld lands, corresponding to the green and blue lines for the OML and IML gages, respectively. Overall, the predicted and measured strains agree well. The results indicate similar strain behavior as was seen in the skin pockets and stiffeners presented in Figs. 4.15 through 4.17 previously. The measured strains near weld lands AB and CA are similar in character and range from $-1150 \mu\epsilon$ to $-1350 \mu\epsilon$ with only slight indications of the settling event at 190 kips (see Figs. 4.18 and 4.20, respectively). The measured strains at weld land BC

range from $340 \mu\epsilon$ to $370 \mu\epsilon$ and indicate a slight tension load. In addition, the strains exhibit a slight increase in magnitude during the settling event at the 190-kips load level.

Predicted and measured strains from gages closest to the buckling initiation location are presented in Fig. 4.21. Buckling of the cylinder wall initiated in Panel A near the location indicated by the red X symbol in the figure. The two strain gage locations closest to the buckling initiation location are at $(-32.8 \text{ inches}, 0^\circ)$ and $(-18.0 \text{ inches}, 0^\circ)$, where (x, θ) denote axial and circumferential coordinates using the coordinate system defined in Fig. 2.7. At both locations, there is a pair of gages, one located on the cylinder OML and the other on the side of the internal longitudinal stiffener. For the pair at $(-32.8 \text{ inches}, 0^\circ)$, strain gages 007ORA and 062IRA are the OML and IML stiffener gages, respectively. For the pair at $(-18.0 \text{ inches}, 0^\circ)$, strain gages 019ORA and 074IRA are the OML and IML stiffener gages, respectively. The measured results indicate linear behavior up to approximately 275 kips. As the total load approaches the buckling load, the measured load versus strain response curves for the strain gage pair 007ORA and 062IRA begin to diverge, indicating of the onset of buckling near this location (as was illustrated in Fig 4.14 displacement contours). The corresponding predicted strains are presented and do not correlate as well as the predicted strains presented in Figs. 4.15 through 4.20. The reason for this poor correlation is not currently known, however, it is likely that the use of beam elements in the finite-element models of the stiffeners as well as the sensitivity of the strain measurements and predictions in regions of large magnitude bending gradients near the boundary may have a significant effect on the results correlation. Additional detailed test and analysis correlation is required to fully assess these modeling and measurement sensitivities.

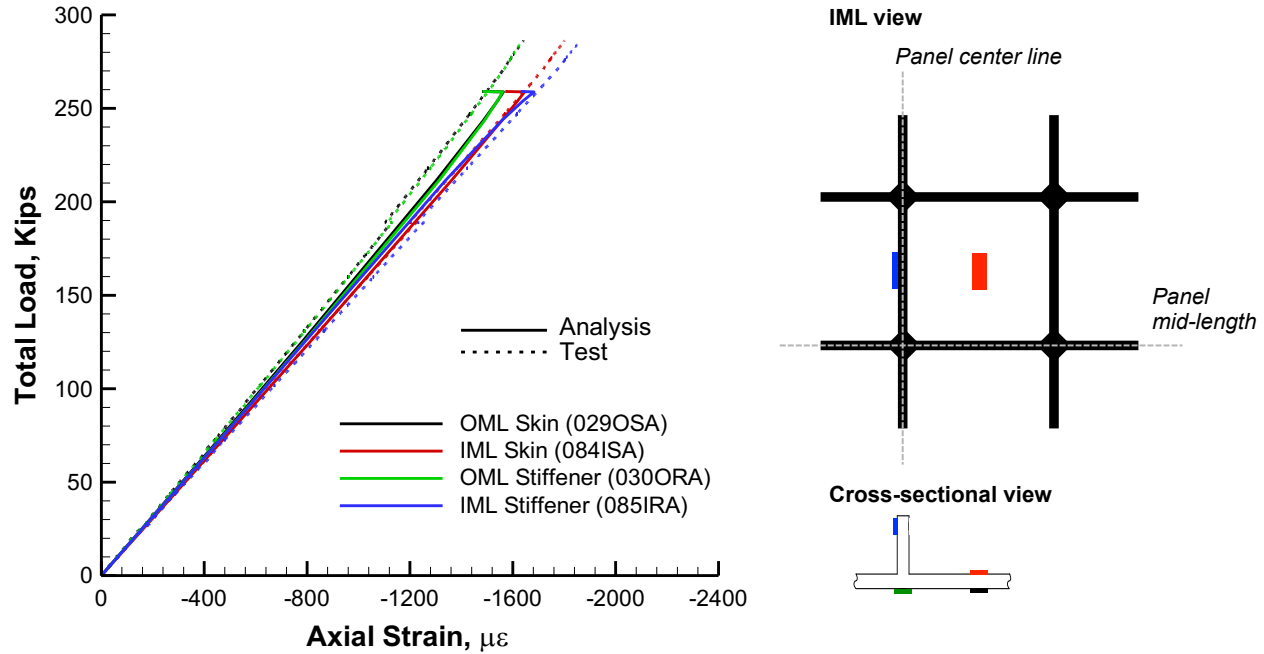


Figure 4.15. Predicted and measured strains of back-to-back axial gages, skin and adjacent axial stiffener near center of Panel A. Panel A skin pocket: 029OSA/084ISA, Panel A stiffener: 030ORA/085IRA.

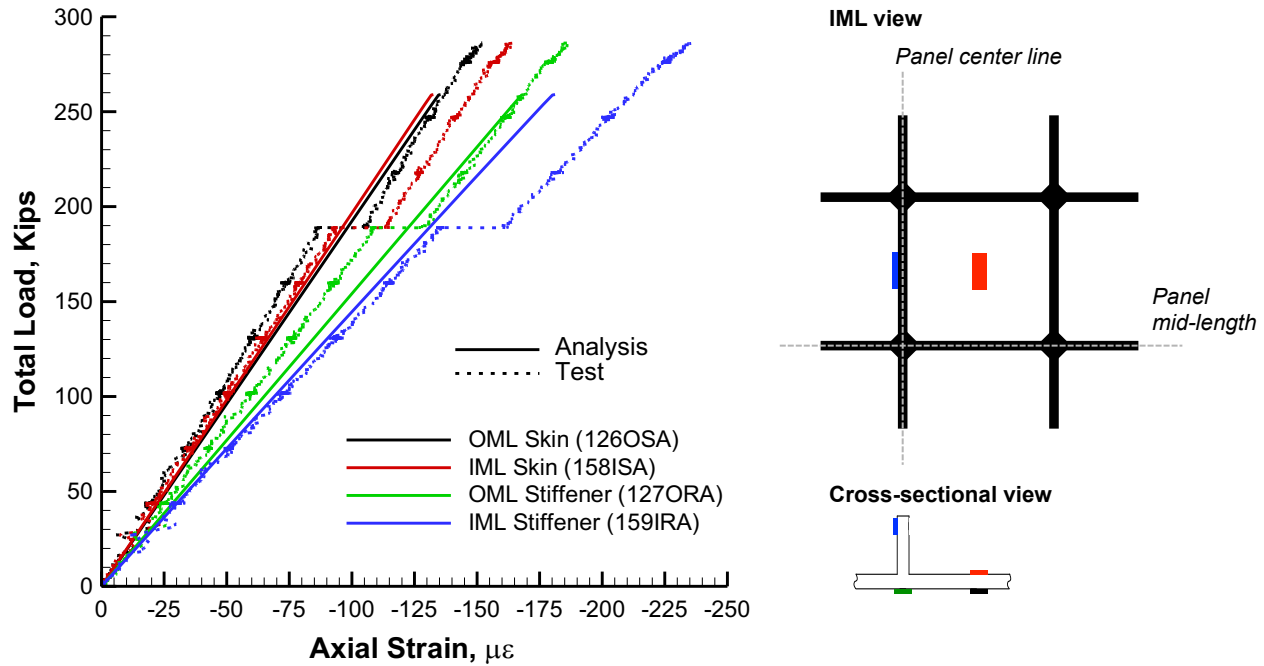


Figure 4.16. Predicted and measured strains of back-to-back axial gages, skin and adjacent axial stiffener near center of Panel B. Panel B skin pocket: 126OSA/158ISA, Panel B stiffener: 127ORA/159IRA.

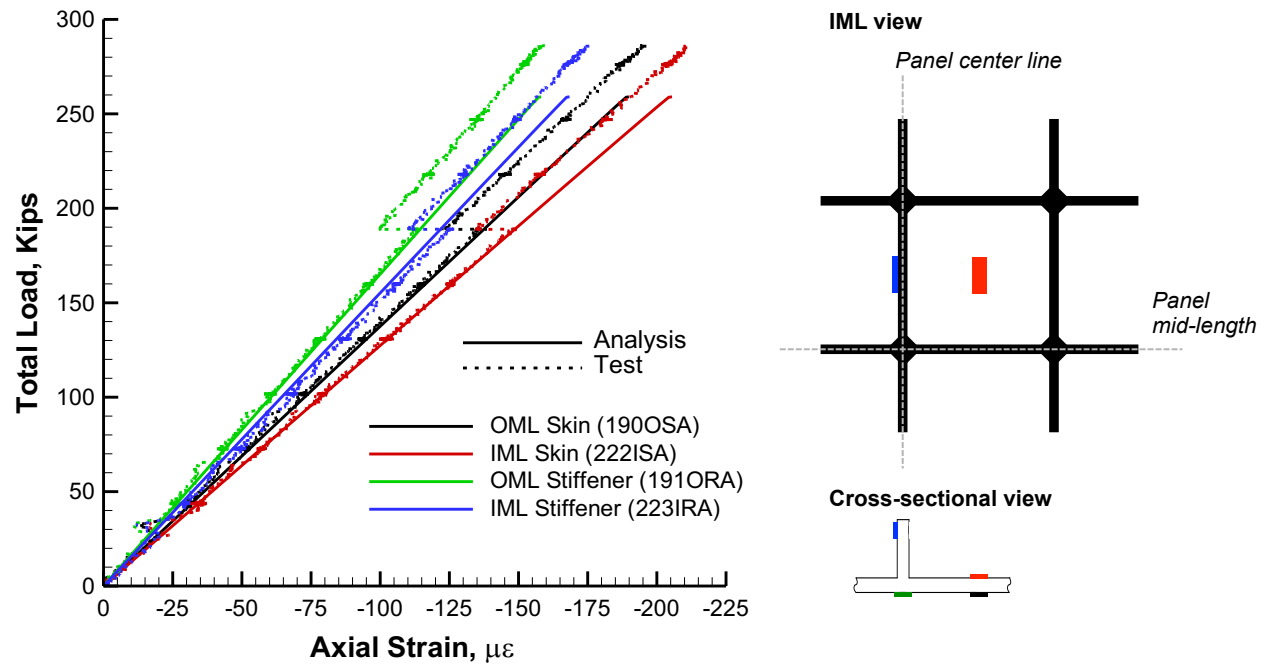


Figure 4.17. Predicted and measured strains of back-to-back axial gages, skin and adjacent axial stiffener near center of Panel C. Panel C skin pocket: 190OSA/222ISA, Panel C stiffener: 191ORA/223IRA.

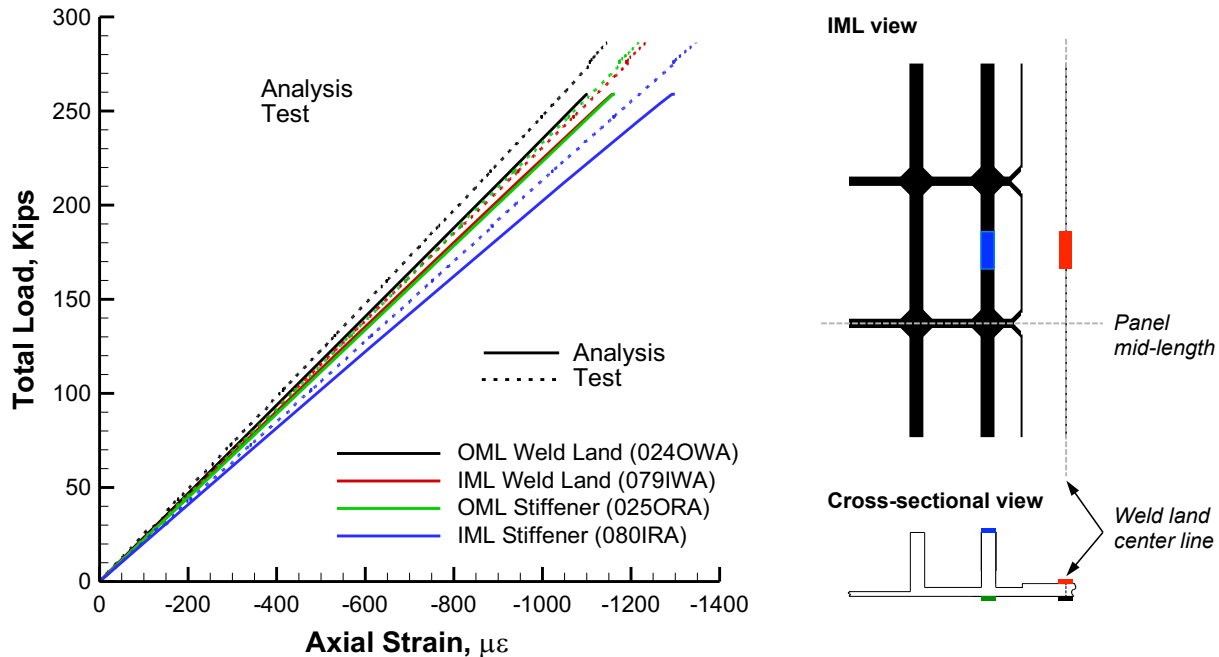


Figure 4.18. Predicted and measured strains of back-to-back axial gages, center of weld land AB and adjacent axial stiffener in Panel A. Weld land AB: 024OWA/079IWA, Panel A stiffener: 025OWA/080IRA.

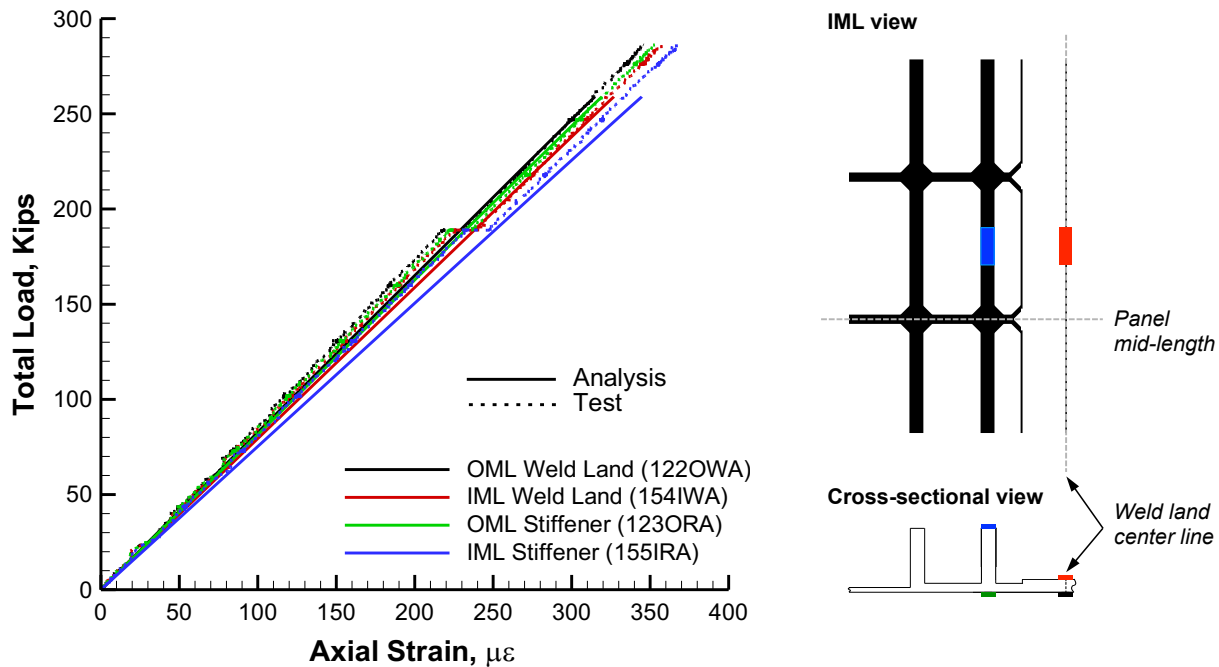


Figure 4.19. Predicted and measured strains of back-to-back axial gages, center of weld land BC and adjacent axial stiffener in Panel B. Weld land BC: 122OWA/154IWA, Panel B stiffener: 123ORA/155IRA.

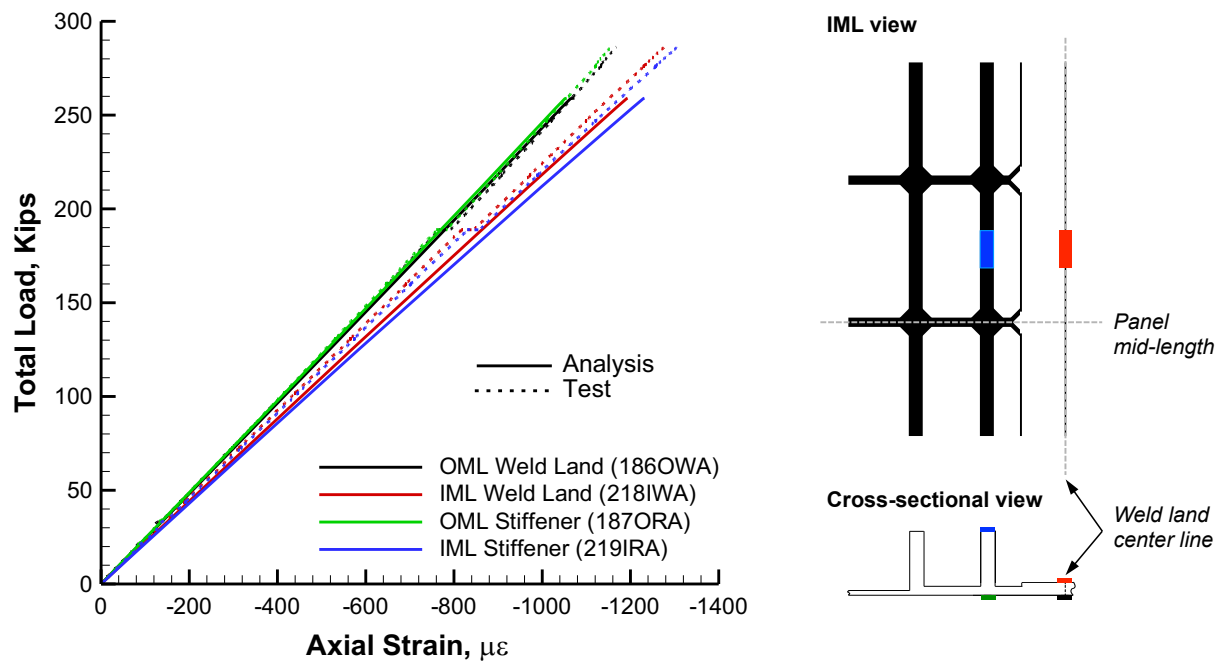


Figure 4.20. Predicted and measured strains of back-to-back axial gages, center of weld land CA and adjacent axial stiffener. Weld land CA: 186OWA/218IWA, Panel C stiffener: 187ORA/219IRA.

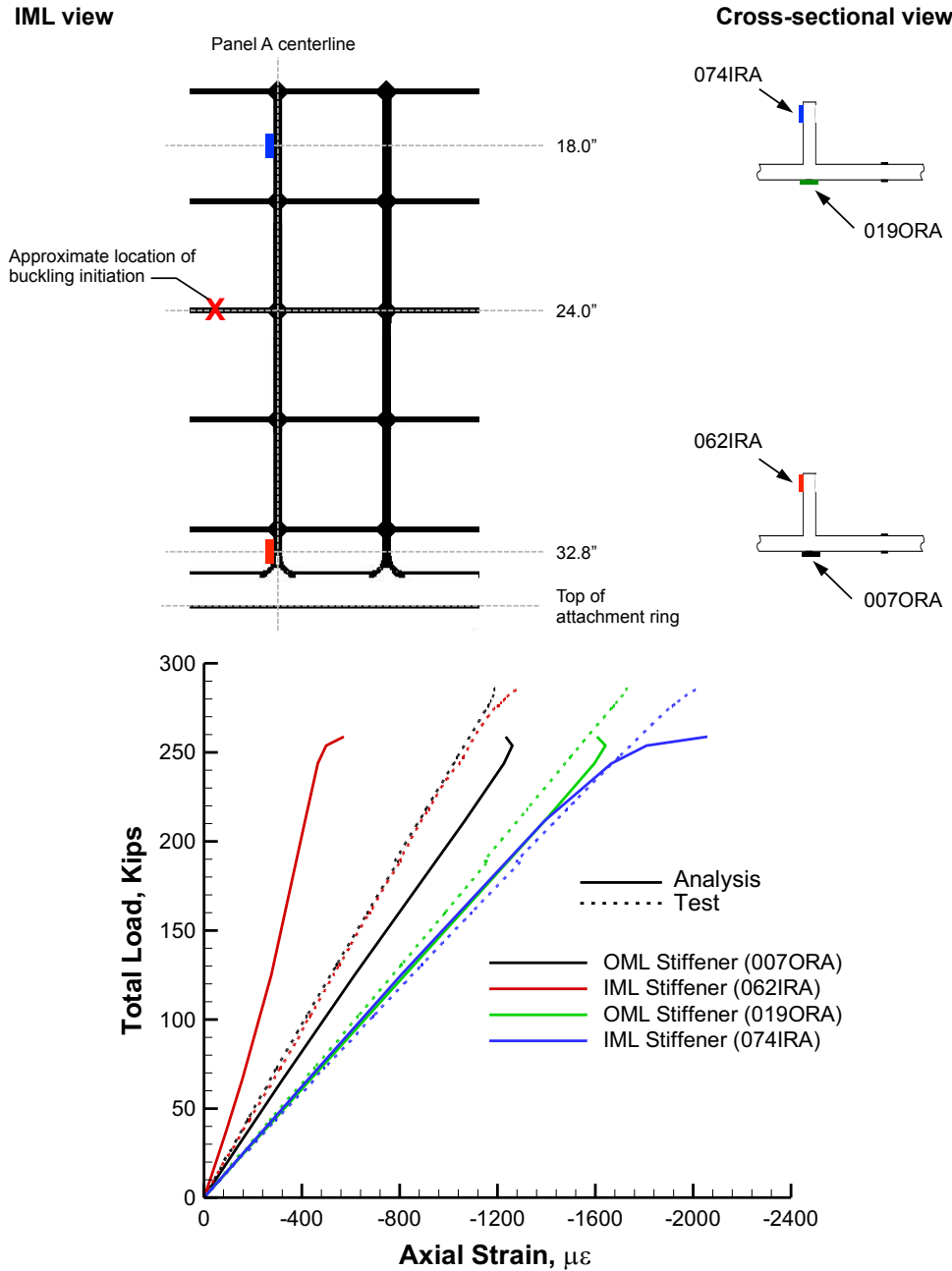


Figure 4.21. Predicted and measured strains of back-to-back axial gages, near buckling initiation location.

4.2.4 Axial Strain Distribution

Plots of the predicted and measured axial membrane strain distribution around the circumference of the test article are presented for selected prebuckling load levels and incipient buckling in Figs. 4.22 through 4.25. Each plot includes data from five different axial locations on the test article including, $x = +32.8$ inches, $+18.0$ inches, $+2.0$ inches, -8.0 inches, and -32.8 inches. The predicted membrane strains are displayed as a solid line and the measured strains from individual strain gages are plotted with open circle symbols. The measured membrane strains are obtained by taking the average of the back-to-back strain gage pairs. The dashed vertical lines at -60° ,

60°, and 180°, mark the weld land locations. The objectives of this strain data comparison are to assess the load distribution in the TA and to validate predicted results.

At a load level of 72.7 kips (25% classical buckling load), the strains exhibit a nonuniform distribution around the circumference of the cylinder as shown in Fig. 4.22 and are consistent with the application of a combined axial compression and bending load. The maximum compression strains occur at $\theta = 0^\circ$ in Panel A and range from $-310 \mu\epsilon$ near the ends of the cylinder to $-470 \mu\epsilon$ at its mid-length. Small magnitude tensile strains occur at $\theta = 180^\circ$ (BC weld land) and are on the order of $90 \mu\epsilon$. The short wave-length variation in the strain distribution near the boundary, shown in Figs. 4.23a and 4.23e, is associated with the skin and stiffener.

As loading increases up to 159.9 kips (55% classical buckling load) and 247.1 kips (85% classical buckling load), the global strain distributions (see Figs. 4.23 and 4.24) remain similar to those shown in Fig. 4.22 with maximum compression strains increasing to approximately $-1600 \mu\epsilon$ as shown in Fig. 4.24. In addition, a sinusoidal variation in the strain distribution appears near the mid-length of Panel A between $\theta = -30^\circ$ and $+30^\circ$ (Figs. 4.23c and 4.24c) and is associated with formation of localized bending deformations in the center of Panel A as shown in the displacement contours in Fig. 4.10.

Predicted and measured strain distributions incipient to buckling are presented in Fig. 4.25. The predicted strains at 258.1 kips (88.8% classical buckling load) are displayed as a solid line and the corresponding measured strains are plotted with open circle symbols. In addition, the measured buckling strains at 286.2 kips (98.4% classical buckling load) are displayed as filled square symbols. The strain distributions, for the most part, continue to follow the trends observed at lower prebuckling load levels, however, the measured and predicted results indicate a slight strain reduction between $\theta = 10^\circ$ and -15° near the bottom of the cylinder (-32.84 inches, Fig. 4.26e). This local reduction in strain corresponds to the formation of the initial ellipse-shaped dimple as shown in the displacement contours in Fig. 4.11a, which leads to a local load redistribution and reduction in membrane strain.

Overall, the predicted and measured strain distributions agree well.

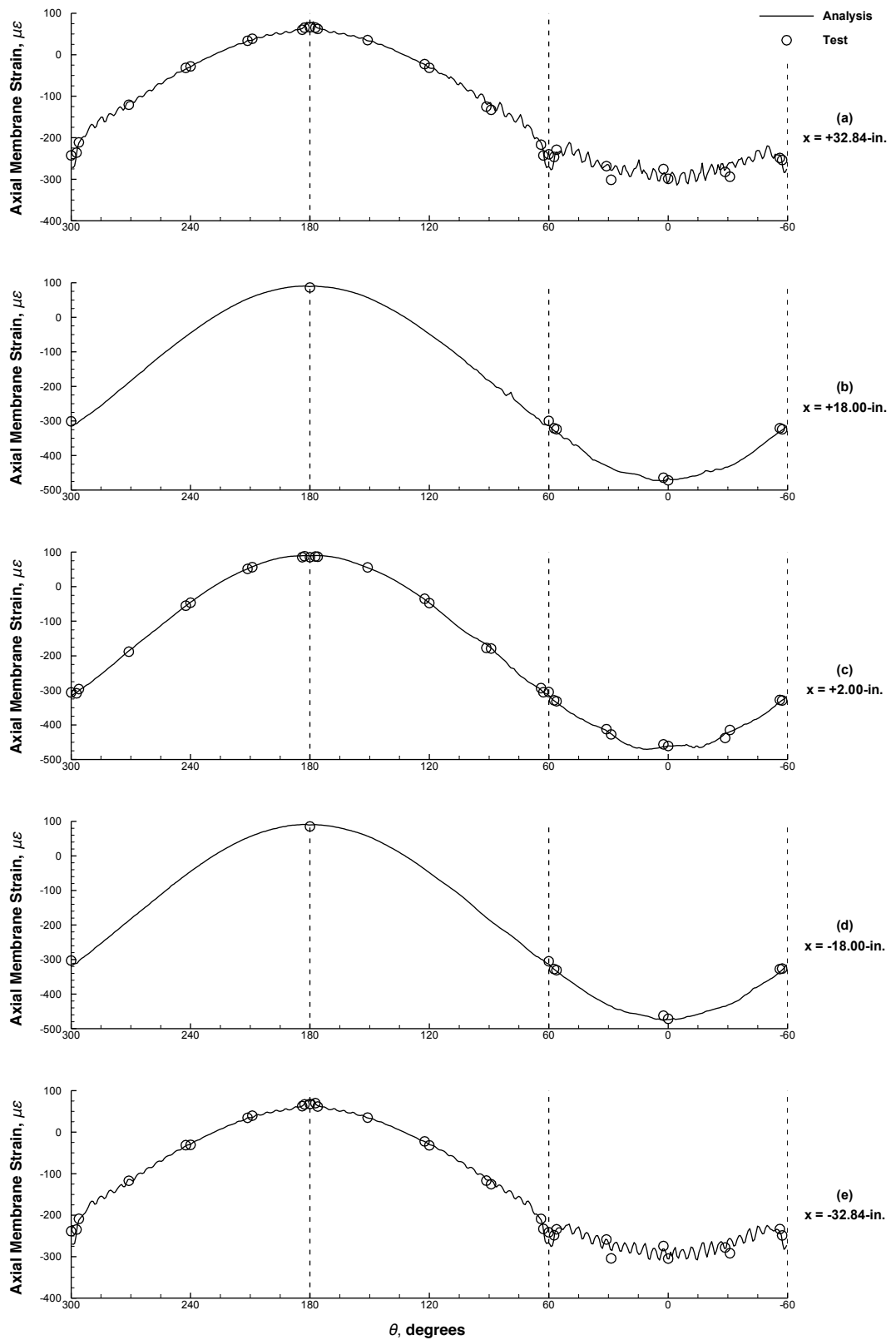


Figure 4.22. Predicted and measured axial membrane strain distribution around circumference, 72.2 kips (25% of classical buckling load).

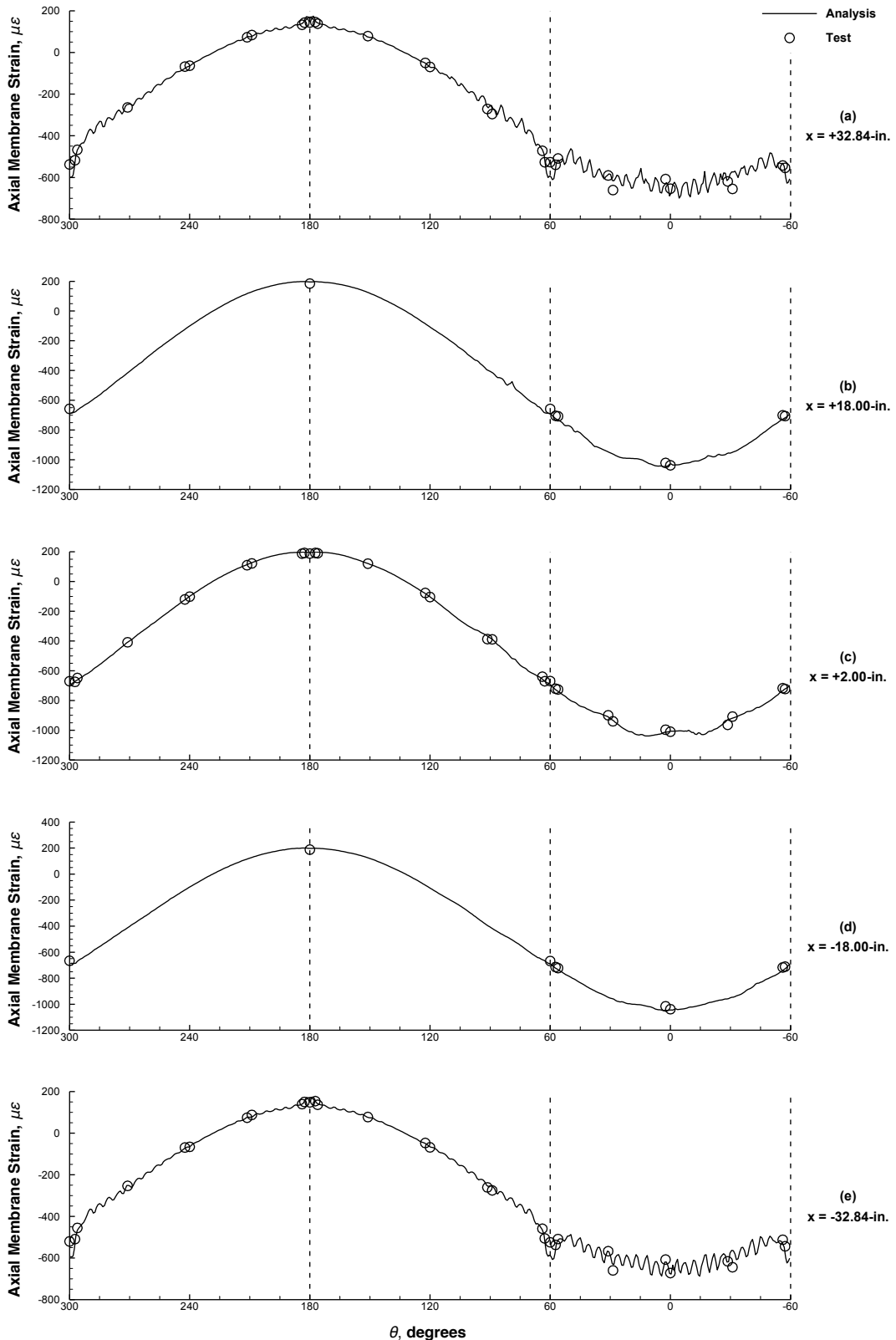


Figure 4.23. Predicted and measured axial membrane strain distribution around circumference, 159.9 kips (55% of classical buckling load).

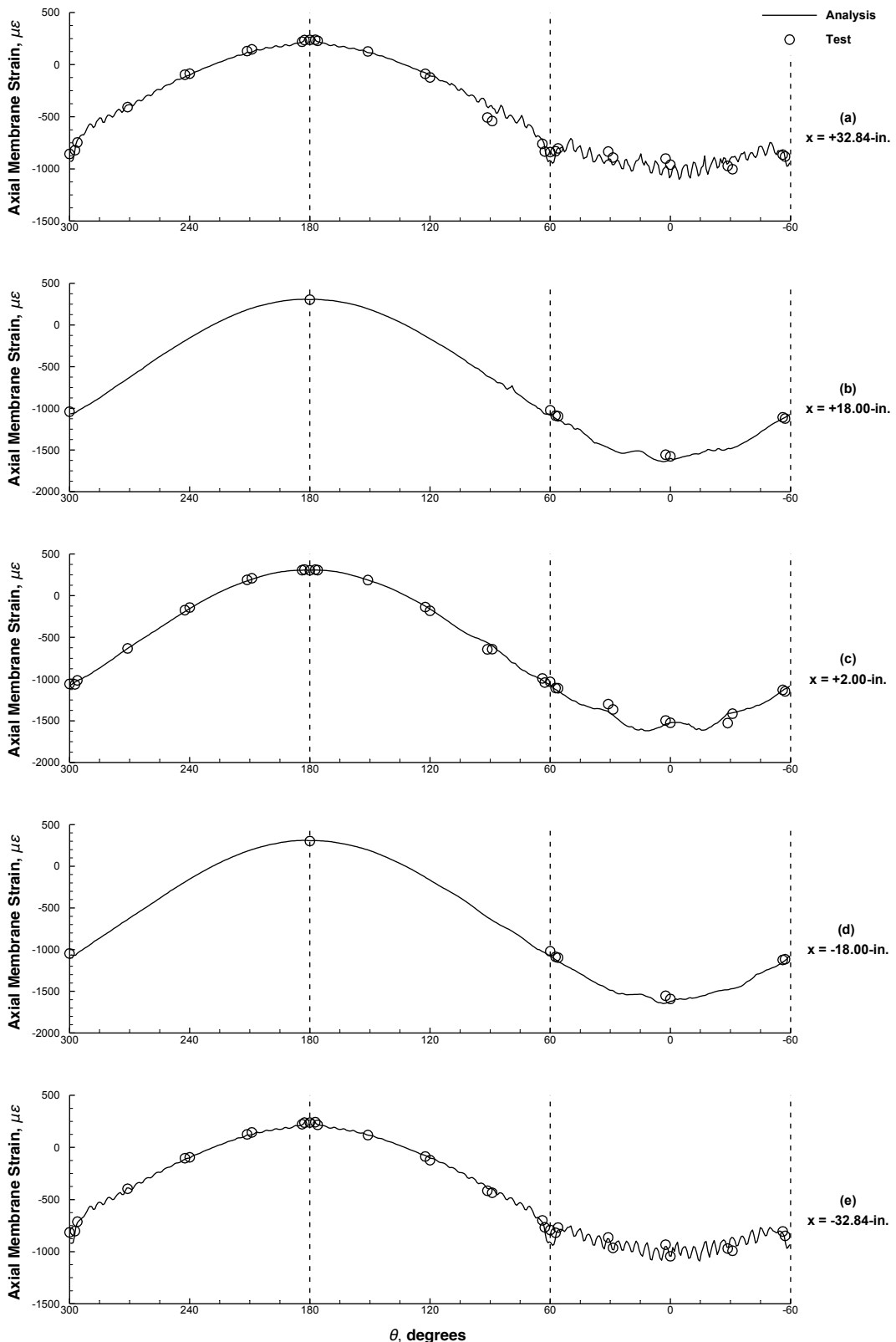


Figure 4.24. Predicted and measured axial membrane strain distribution around circumference, 247.1 kips (85% of classical buckling load).

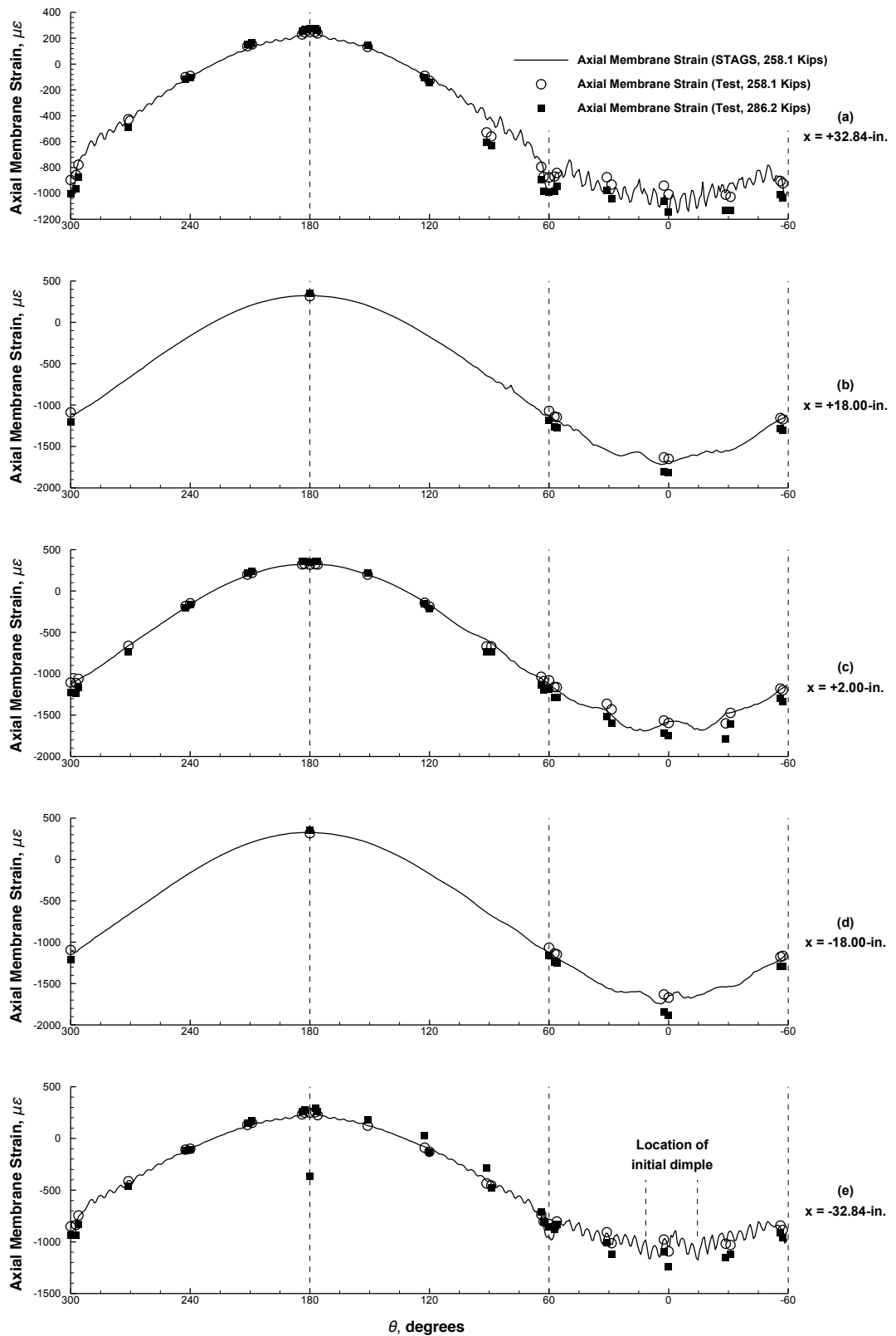


Figure 4.25. Predicted and measured axial membrane strain distribution around circumference, predicted buckling strains and measured data at 258.1 kips (88.8% classical buckling load), measured buckling strains at 286.2 kips (98.4% classical buckling load).

4.3 Buckling Response of TA02 – LS5: Combined Axial Compression and Bending with Maximum Compression over Weld Land BC

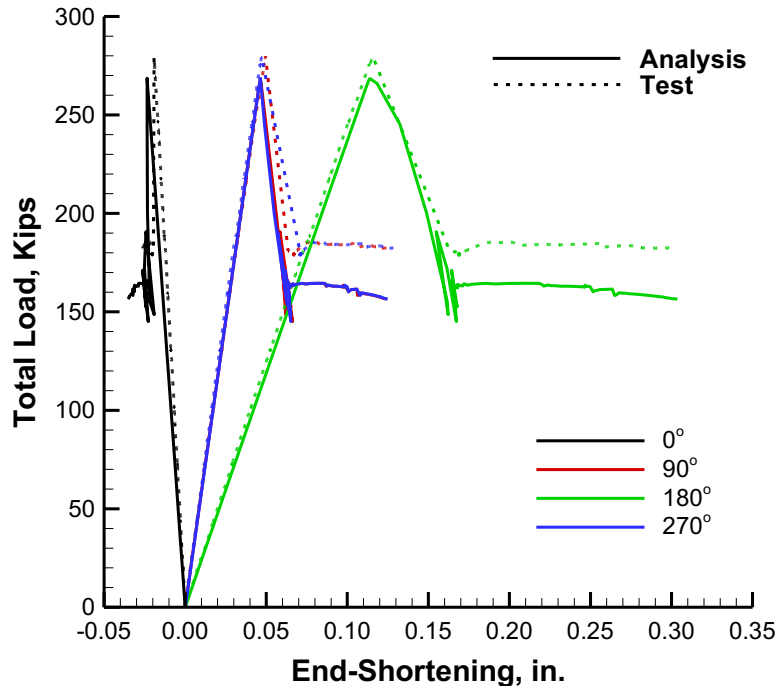
Selected test results are presented to illustrate the overall buckling response of TA02-LS5 subjected to combined axial compression and bending and are compared to pretest predictions. The loading of the cylinder is defined such that an axial-compression-to-bending-load ratio of $1.0P_{cr}:1.5M_{cr}$ is maintained throughout the test and induces a maximum compression load at the center of the BC weld land ($\theta = 180^\circ$) in the TA.

4.3.1 *Load versus Displacement Response*

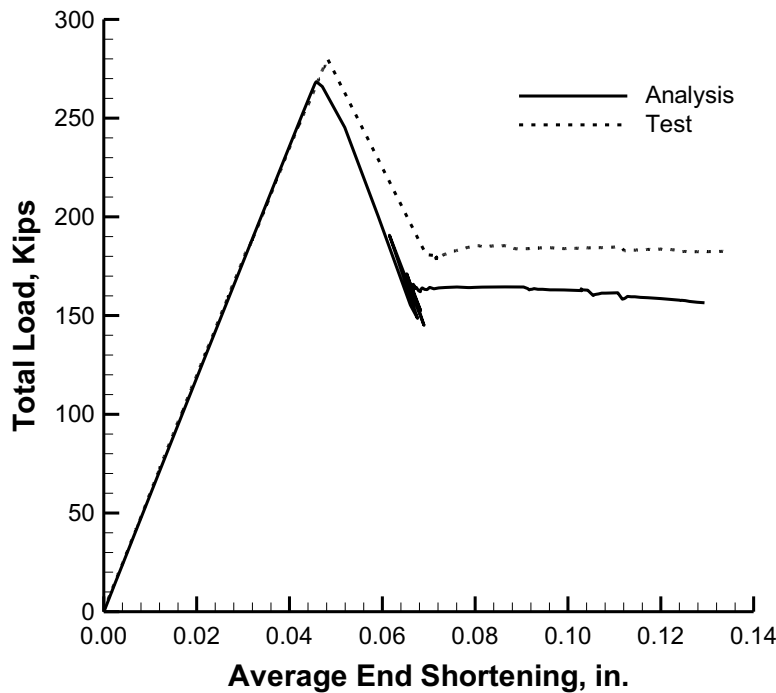
Predicted and measured total load versus end-shortening displacement response curves for TA02-LS5 are shown in Fig. 4.26 and are indicated by the solid and dashed curves, respectively. First, total load versus end-shortening response curves associated with $\theta = 0^\circ, 90^\circ, 180^\circ$, and 270° are presented in Fig. 4.26a by the black, red, green, and blue curves, respectively. The corresponding total load versus average end-shortening displacement response curves are shown in Fig. 4.26b. The total load is defined as the sum of the eight load line loads. The average end-shortening displacement is the average of the end-shortening displacements from the $0^\circ, 90^\circ, 180^\circ$, and 270° circumferential locations.

TA02-LS5 exhibits a linear prebuckling response up to a maximum total load of 280.0 kips. The maximum load is followed by the buckling of TA02-LS5 and is characterized by a sudden reduction in the axial load of approximately 36% to a postbuckling load of 180 kips. In addition, the measured load-shortening response curve indicates a significant increase in the end-shortening displacement during the buckling response from 0.049 inches to 0.072 inches. This behavior was also observed during the transient collapse response of TA02 during LS4.

Overall, the character of the load versus end-shortening response is predicted well, including the prebuckling and postbuckling axial stiffness; and, the predicted maximum total load of 268.0 kips is approximately 4.3% lower than the measured maximum total load of 280.0 kips. A similar difference was observed in the test and analysis correlation of TA02-LS4 as reported in Section 4.2.1.



a) Total load versus end-shortening displacement response at four circumferential locations.



b) Total load versus average end-shortening response.

Figure 4.26. Measured and predicted load versus end-shortening response of TA02-LS5 subjected to combined axial compression and bending.

Predicted and measured prebuckling total load versus radial displacement response curves at the center of each panel and the center of each weld land are presented in Figs. 4.27 and 4.28, respectively. Panels A, B, and C are shown with black, red, green, and blue curves, respectively.

Weld lands AB, BC, and CA are shown with black, red, and green curves respectively. The buckling and postbuckling data are omitted from the figures so that the small-magnitude prebuckling displacements could be seen more clearly. Positive displacements correspond to outward radial displacements.

The measured results indicate that the centers of panels B and C and weld land BC move radially outward during the prebuckling response with a maximum displacement of 0.049 inches at weld land BC. In contrast, the centers of weld lands AB and CA and Panel A move radially inward with a maximum displacement of -0.027 inches at the center of Panel A. The predicted results indicate similar response trends overall, however, the maximum displacement in the center of weld land BC is predicted to be 0.106 inches incipient to buckling, which is 116% greater than the corresponding measured displacement.

Prebuckling, buckling, and postbuckling radial displacement response curves for the centers of panels B and C and weld land BC are shown in Fig. 4.29. At the maximum load, the results indicate a sudden change in the displacements, corresponding to the buckling of the TA wall with maximum measured inward displacements of -2.35 inches at the center of Panel B. A photo of the buckled TA is shown in Fig. 4.30. The black **X** symbol on the TA corresponds to the center of the BC weld land, around which, some of the large magnitude buckling deformations can be observed.

Overall, the predicted load versus end-shortening displacement response trends and most of the radial displacement response trends correlate well with the measured results. However, as loading approaches the buckling load of the TA, the predicted displacements at weld land BC are larger in magnitude than the corresponding measured displacements. This difference between the predicted and measured behavior can be seen when comparing the predicted and measured displacement contours shown later in Fig. 4.38. In particular, the predicted results indicate the formation of a distinct outward bulge at the mid-length of the weld land. In contrast, the DIC results do not exhibit such a local displacement response.

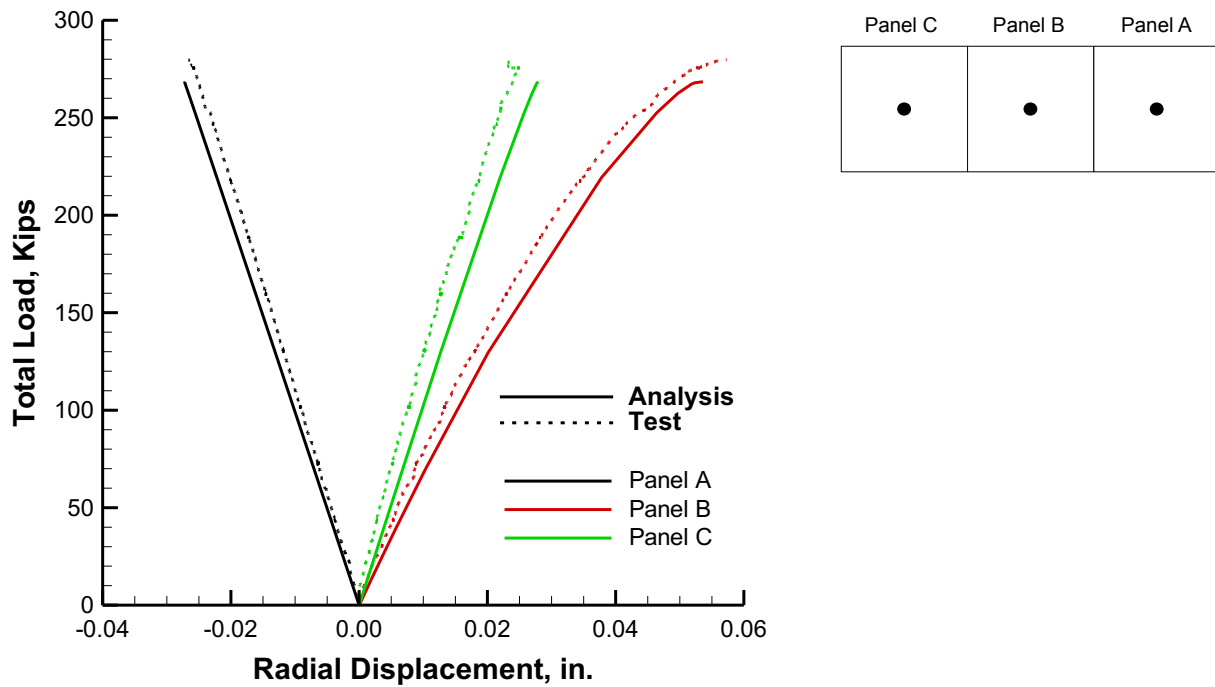


Figure 4.27. Measured and predicted load versus radial displacement response of TA02-LS5 at the center of each panel.

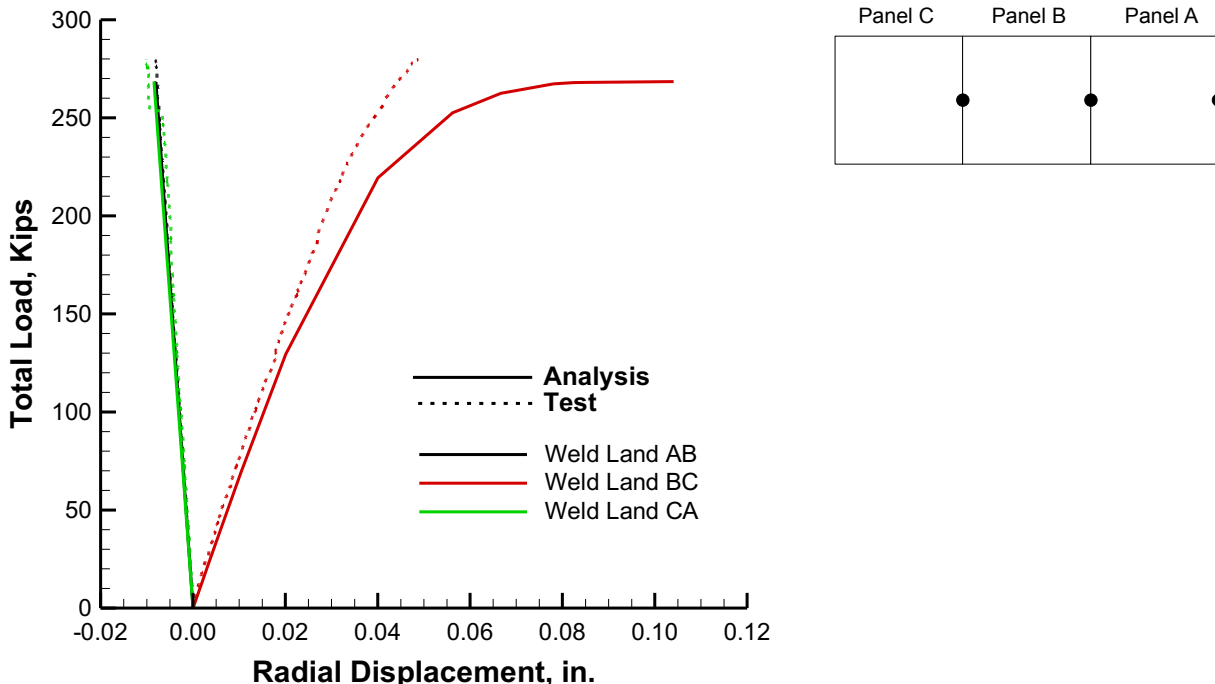


Figure 4.28. Measured and predicted load versus radial displacement response of TA02 at the center of each weld land.

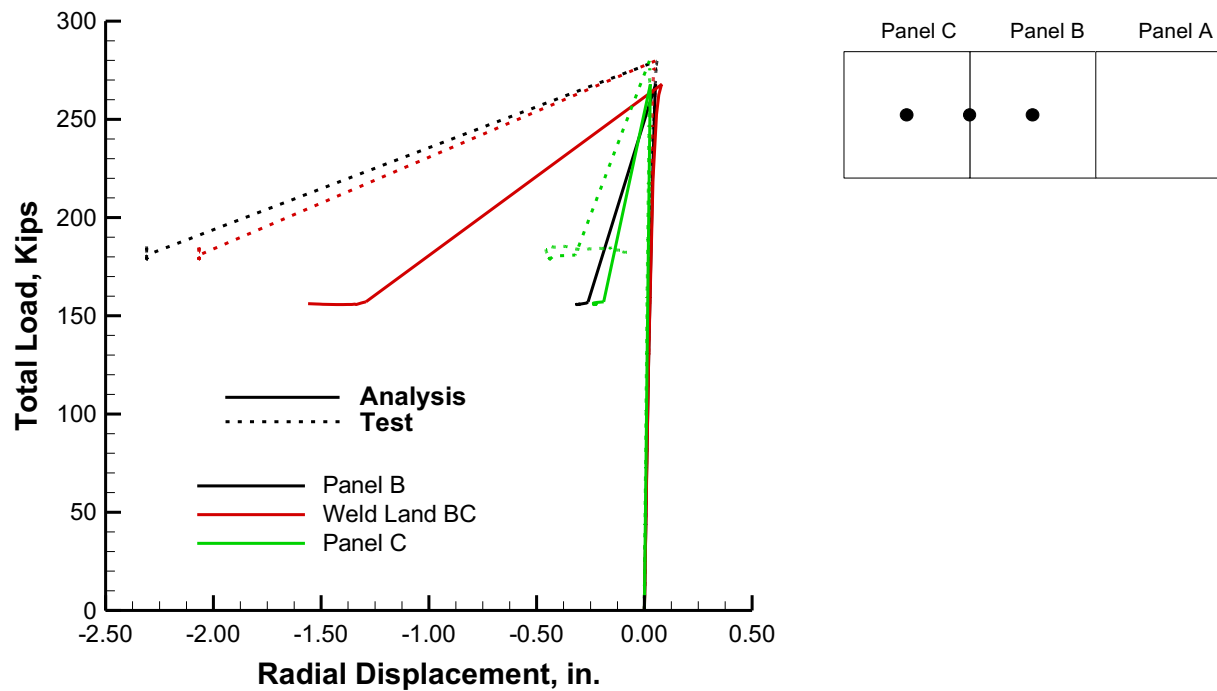


Figure 4.29. Measured and predicted load versus radial displacement response of TA02 at the center of weld land BC and panels B and C.



Figure 4.30. TA02-LS5 after buckling.

4.3.2 *Full-Field Displacement Contours*

Predicted and measured full-field prebuckling, buckling, and postbuckling displacement contours are presented in this section. Dashed vertical lines are shown in the contour plots at -60° , 60° , and 180° and correspond to weld lands CA, AB, and BC, respectively. First, estimates of the noise in the DIC measurements are presented. Second, the initial geometry for TA02-LS5 is presented and compared to the initial geometry for TA02-LS4. Third, selected axial and radial full-field displacement contours obtained from low-speed DIC systems are presented and compared to initial pretest predictions. Finally, HS-DIC displacement contours obtained during the buckling response of the test article are presented.

Low-Speed DIC Displacement Measurements

An estimate of the low-speed DIC measurement noise for the axial, u , and radial, w , displacement measurements is presented in Figs. 4.31a and 4.31b, respectively. The results indicate measurement noise across all DIC systems of approximately ± 0.004 inches in the axial displacements and ± 0.010 inches in the radial displacements. These levels of accuracy are typical for this type of DIC system, set-up parameters and calibration method used. In addition, these measurement noise values are same as those obtained for LS4 presented in Figs. 4.7a and 4.7b.

Note: data are missing in two locations around the circumference of the TA due to load lines obstructing the FOV of the DIC systems (i.e., approximately 10° bands near $\theta = 110^\circ$ and 290°).

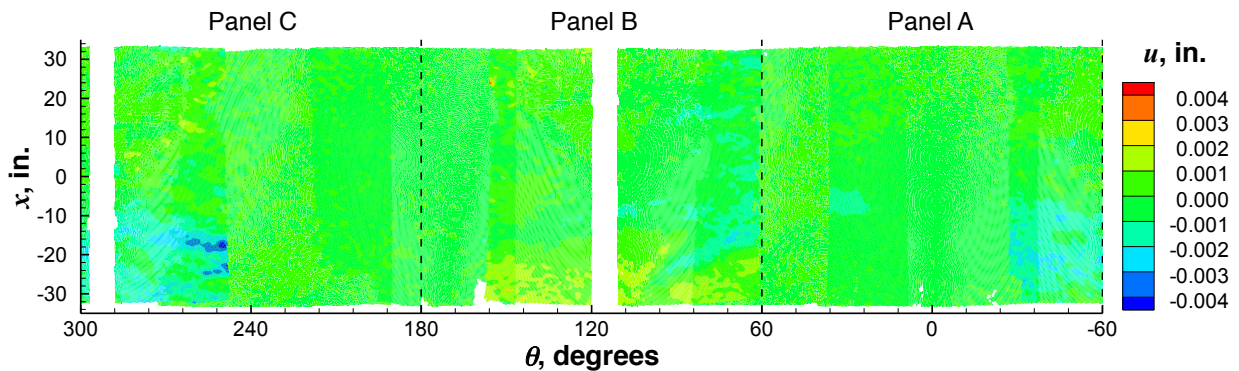
The geometry of TA02 was measured with the DIC systems prior to LS5 to characterize the residual deformations that resulted from material yielding that occurred during the TA02-LS4 test to failure (see Fig. 4.13). The geometry is shown in Fig. 4.32a and indicates a periodic distribution of residual deformations in Panel A and into the adjacent panels B and C. The magnitude and extent of the residual deformations can also be seen in Fig. 4.32b in which circumferential traces of the TA geometry at the cylinder mid-length are presented. In particular, DIC-based geometry prior to LS4 (unbuckled) and prior to LS5 (with residual deformations from LS4) are shown in the figure as black dotted and red solid lines, respectively. The residual deformations in the TA are indicated by the difference between the LS4 and LS5 data. The data also show that the TA does not appear to have any residual deformations between $\theta = 95^\circ$ and 240° as indicated by the coincident data curves.

Selected axial and radial displacement contours are presented in Figs. 4.33 through 4.37 and include predicted and measured results from three prebuckling load levels and initial postbuckling. Prebuckling u and w displacements at 72.8 kips (approximately 25% of the classical buckling load) are shown in Figs. 4.33 and 4.34, respectively. The predicted u displacements indicate a periodic end displacement distribution on the top edge of TA02 with maximum u displacement of -0.034 inches at $\theta = 180^\circ$ at weld land BC and a u displacement of 0.006 inches at $\theta = 0^\circ$ at the center of Panel A. This end displacement distribution is consistent with the applied combined axial compression and bending loads. Overall, the corresponding measured displacements show a similar sinusoidal distribution. However, some localized variation is observed in the measured data and is attributed to the inherent measurement noise shown in Fig. 4.31a. The predicted w displacements, shown in Fig. 4.34a, indicate the development of a periodic distribution of inward and outward radial deformations within panels B and C characterized by approximately five circumferential half-waves that span from 120° to 225° . This periodic distribution of circumferential half-waves is most noticeable at and below the mid-length of the cylinder and is similar to the response observed during LS4 as shown in Fig. 4.9. Maximum outward displacements of 0.023 inches occur at the top of panels B and C near the BC weld land and are associated with the applied bending load that causes the top portion of the cylinder to translate out of plane. The corresponding measured displacements are shown in Fig. 4.34b and indicate a similar response.

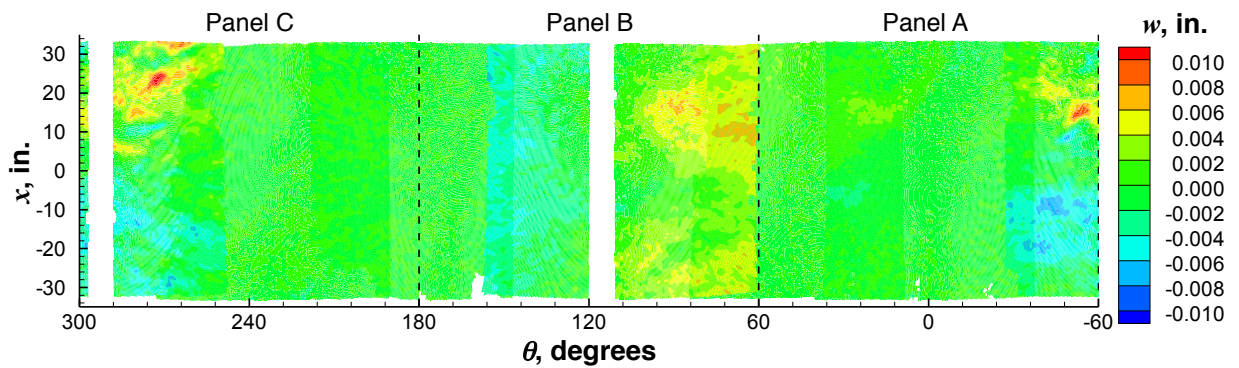
Predicted and measured w displacement contours at 159.6 kips (approximately 55% of the classical buckling load) are shown in Figs. 4.35a and 4.35b, respectively. Overall, the contour patterns are similar to those observed at the lower load levels. The predicted and measured u displacement distributions at this load level (not presented herein) are similar to those presented in Fig. 4.33.

As the applied load increases up to the buckling load of the TA, both the predicted and measured radial displacement contours indicate the development of a distinct ellipse-shaped dimple at the mid-length of the cylinder at $\theta = 140^\circ$ in Panel B as shown in Fig. 4.36. The predicted and measured amplitude of this inward dimple, incipient to buckling, is between 0.030 and 0.040 inches. The unstable buckling response of TA02-LS5 initiates at this dimple and is accompanied by a significant reduction in total load (see Fig. 4.26) and the development of numerous buckles throughout panels B and C as shown in Fig. 4.37. In particular, the predicted

initial postbuckling displacements exhibit a periodic distribution of buckles at the mid-length of the panel with the maximum amplitude displacements occurring at weld land BC on the order of -1.2 inches. The measured buckling displacements also exhibit a similar periodic distribution of buckles; however, the buckles are slightly offset towards Panel B. Post-test inspection of the test article indicated permanent deformations associated with material yielding in the areas of the buckles. Due to the nature of the buckles (i.e., having large out-of-plane displacements), large bending strains are generated when buckles develop. These large bending strains could cause material yielding during the transient buckling response and result in a different initial postbuckling state when compared to predictions from an analysis that only considers elastic material properties.

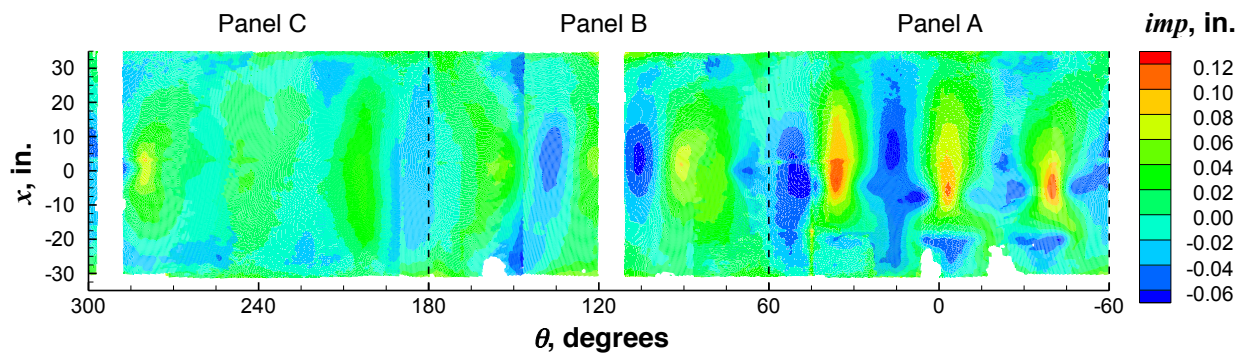


a) u displacement noise signature.

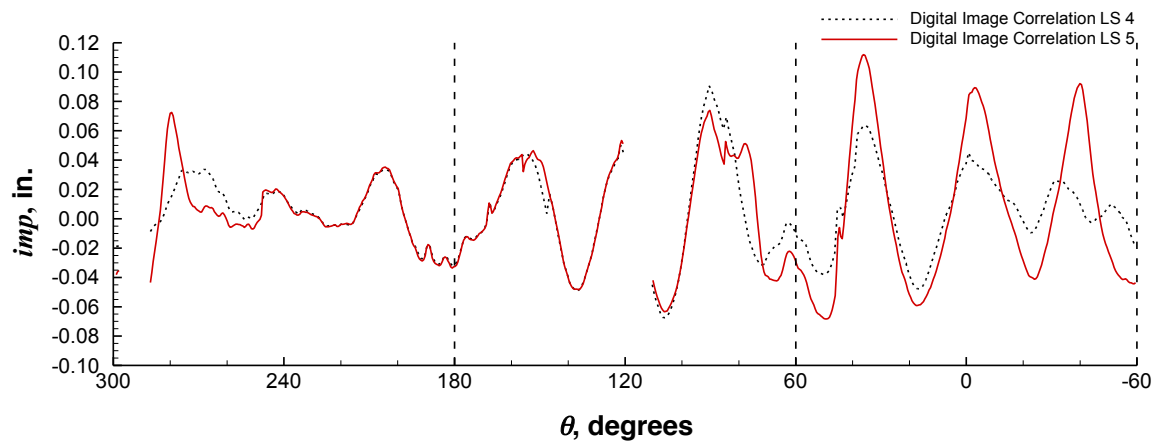


b) w displacement noise signature.

Figure 4.31. DIC noise signature for u and w displacement measurements for TA02-LS5.



a) DIC contour.



b) Circumferential trace of initial geometry measured at cylinder mid-length.

Figure 4.32. Measured initial geometry from DIC systems.

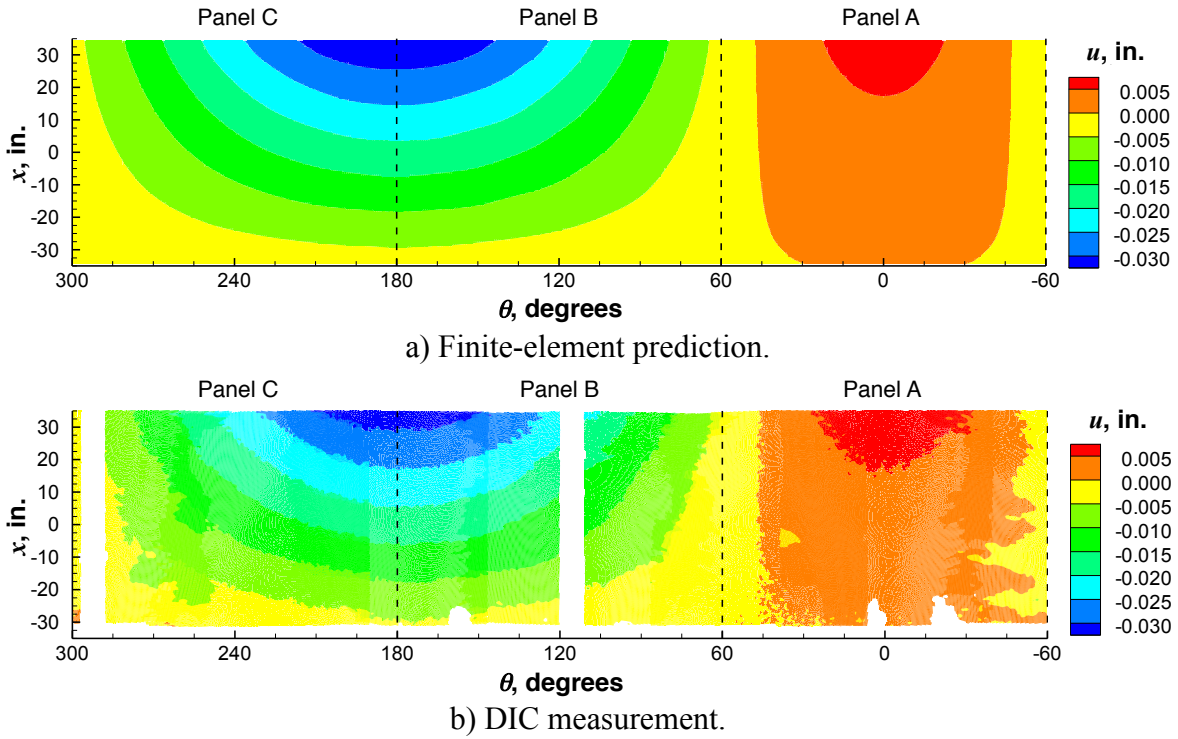


Figure 4.33. Predicted and measured axial displacement (u) contours at 72.8 kips (25% classical buckling load).

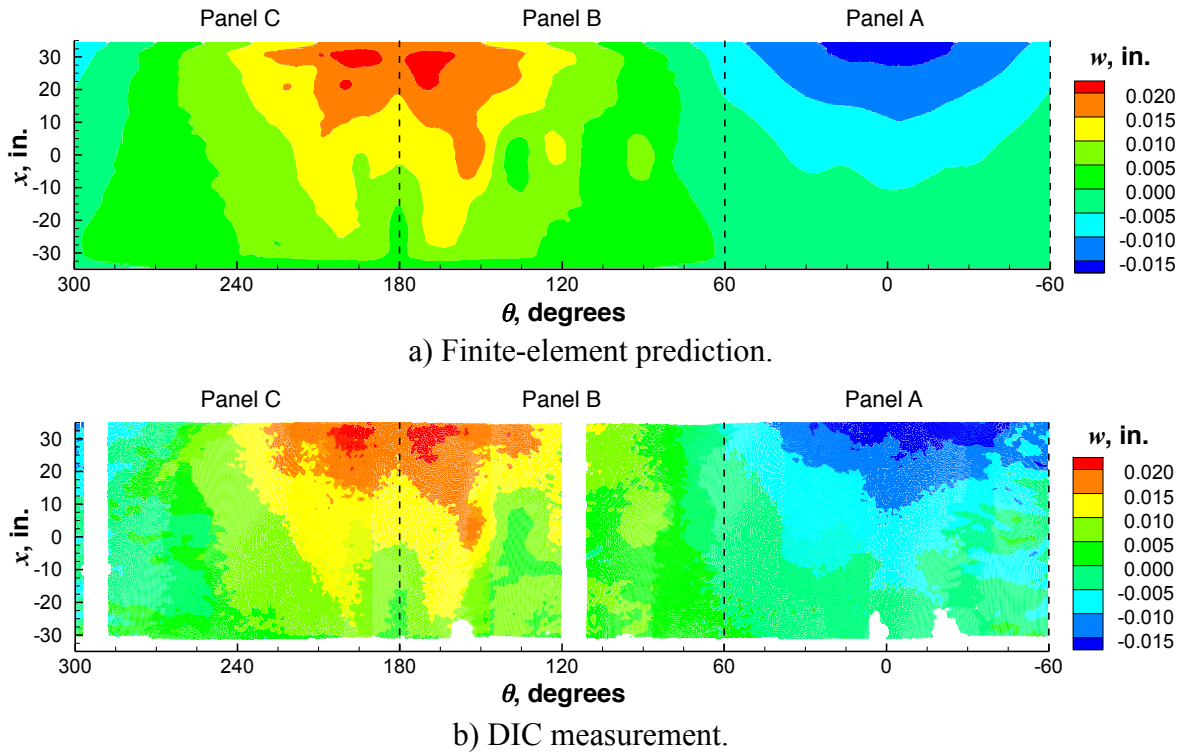
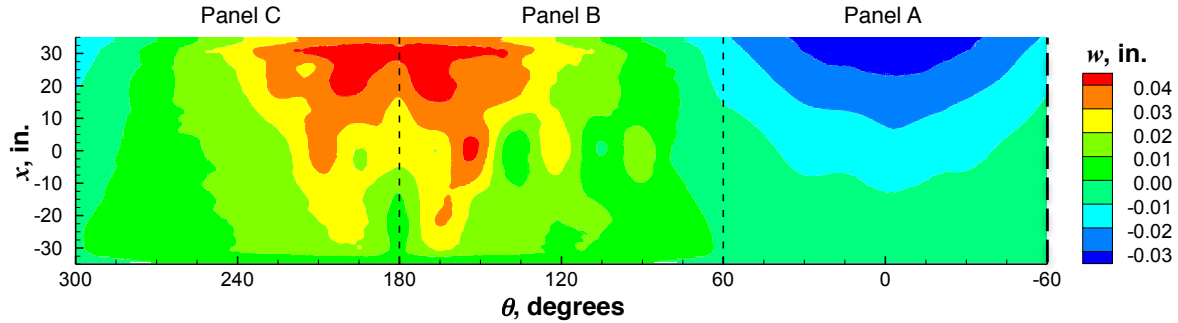
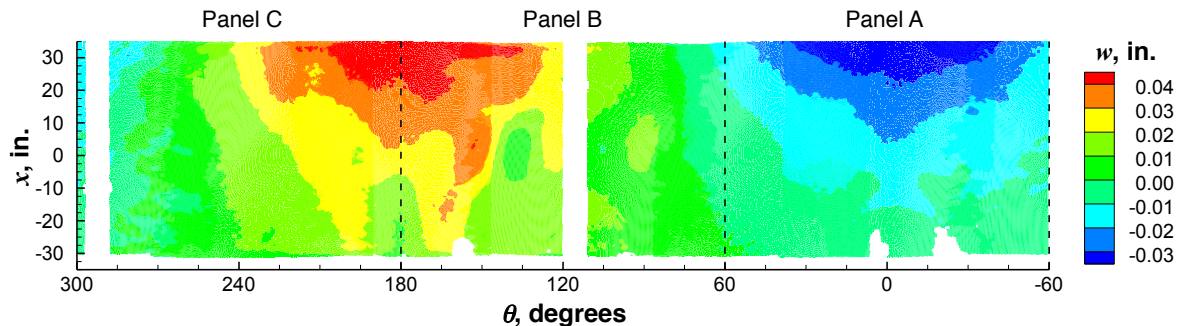


Figure 4.34. Predicted and measured radial displacement (w) contours at 72.8 kips (25% classical buckling load).

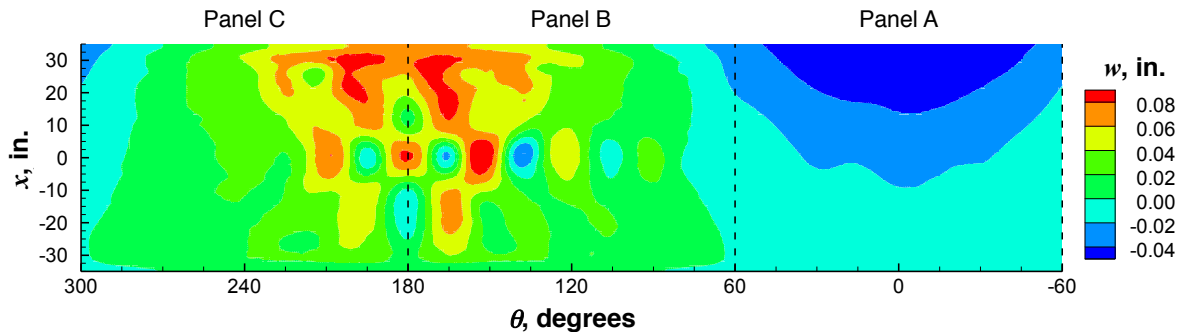


a) Finite-element prediction.

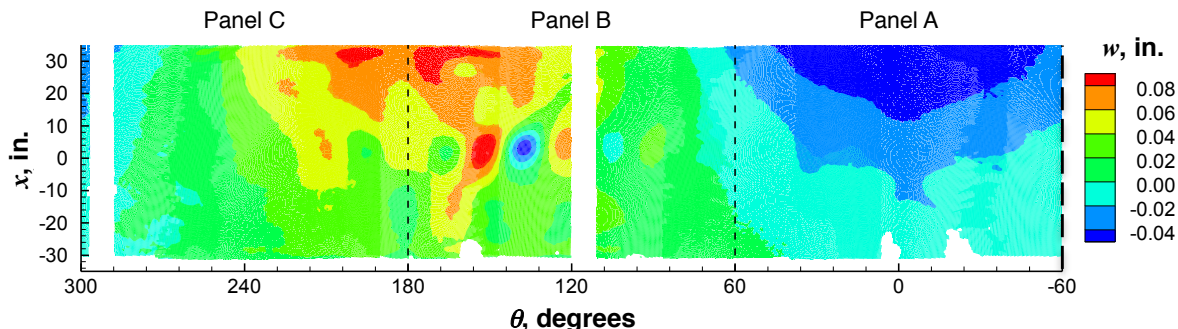


b) DIC measurement.

Figure 4.35. Predicted and measured radial displacement (w) contours at 159.6 kips (55% classical buckling load).

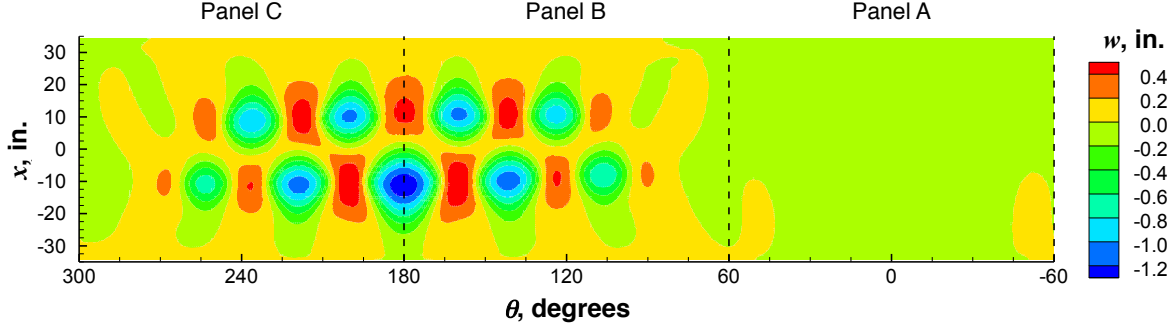


a) Finite-element prediction 267.9 kips (92% classical buckling load).

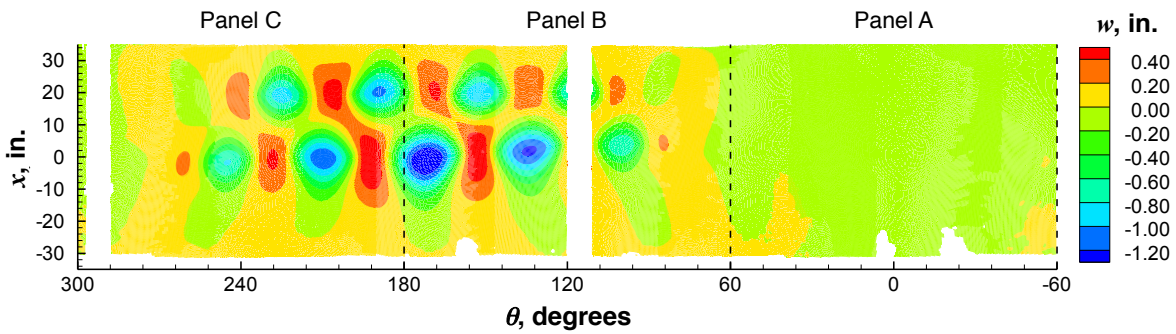


b) DIC measurement 279.7 kips (96% classical buckling load).

Figure 4.36. Predicted and measured radial displacement (w) contours incipient to buckling.



a) Finite-element prediction 164.3 kips.



b) DIC measurement 178.9 kips.

Figure 4.37. Predicted and measured radial displacement (w) contours at initial postbuckling equilibrium for TA02-LS5.

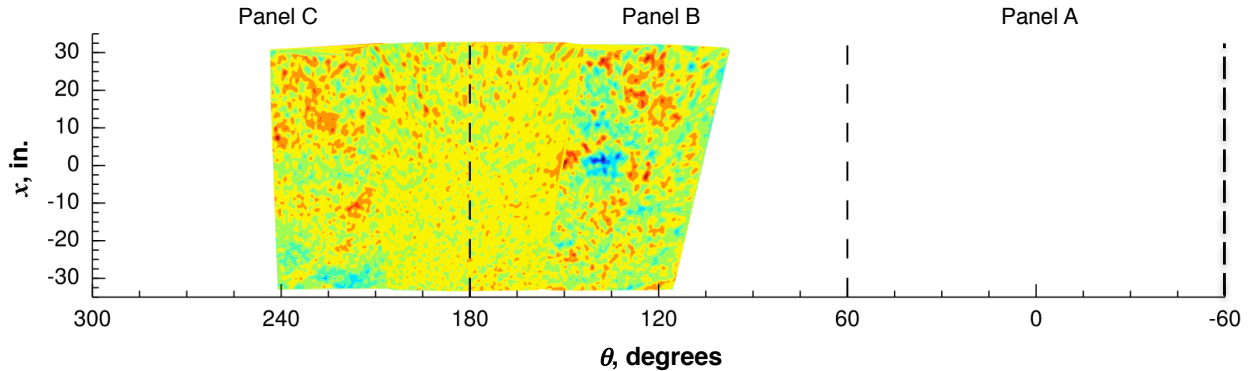
High-Speed DIC Displacement Measurements

Selected radial displacement contours obtained from the HS-DIC systems are presented to illustrate the unstable transient buckling response of the test article in Fig. 4.38. Four three-dimensional HS-DIC systems were set up around the circumference of the TA and captured images at 10,000 fps (see Fig. 2.13b). Three of the four HS-DIC systems were used to characterize the deformation response of portions of panels B and C and the BC weld land from approximately 120° to 240° around the circumference of TA02. The fourth HS-DIC system was positioned at $\theta = 0^\circ$ but failed to capture images during the collapse event. The blue and green contours represent inward radial deformations and the red contours represent outward radial deformations.

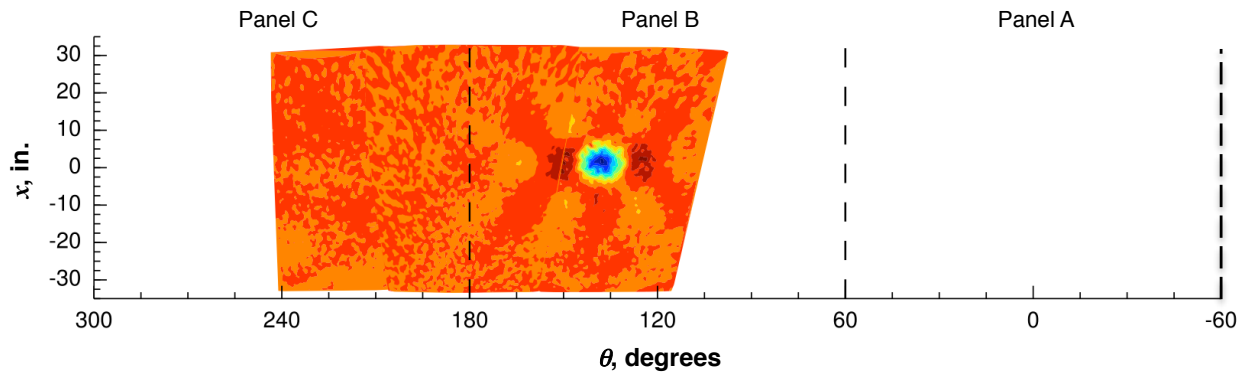
Incipient buckling contours are shown for $t = 0.0$ seconds⁷ in Fig. 4.38a and show a slight indication of an initial ellipse-shaped dimple in Panel B (blue contour), as was observed in the corresponding low-speed DIC measurement shown in Fig. 4.36b. At time $t = 0.0086$ seconds, the initial dimple becomes more distinct and additional small dimples begin to develop around the perimeter of the initial dimple as shown in Fig. 4.38b. As the collapse response continues, additional buckles form and propagate throughout Panel B and into Panel C as shown in Figs. 4.38c (time $t = 0.0128$ seconds), 4.38d (time $t = 0.0173$ seconds), and 4.38e (time $t = 0.0197$ seconds) until a fully developed postbuckling configuration is obtained as shown in

⁷ Note: $t = 0.0$ seconds is an arbitrary time reference used to determine relative time throughout the transient collapse response.

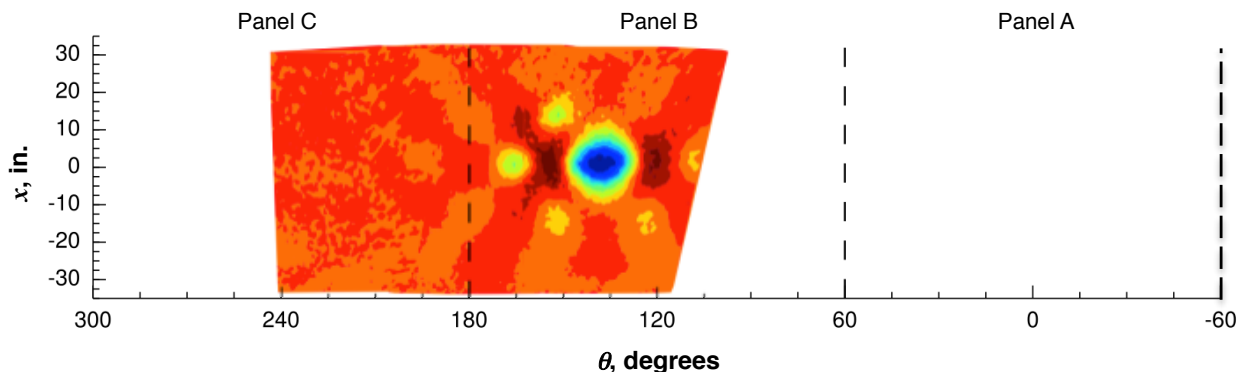
Fig. 4.38-f at time $t = 0.0312$ seconds. The measured postbuckling displacement patterns correlate well with the corresponding low-speed DIC contours presented in Fig. 4.37b and are characterized by two rows of buckles with nine half-waves visible in the FOV.



a) Incipient buckling, $t = 0.0$ seconds.

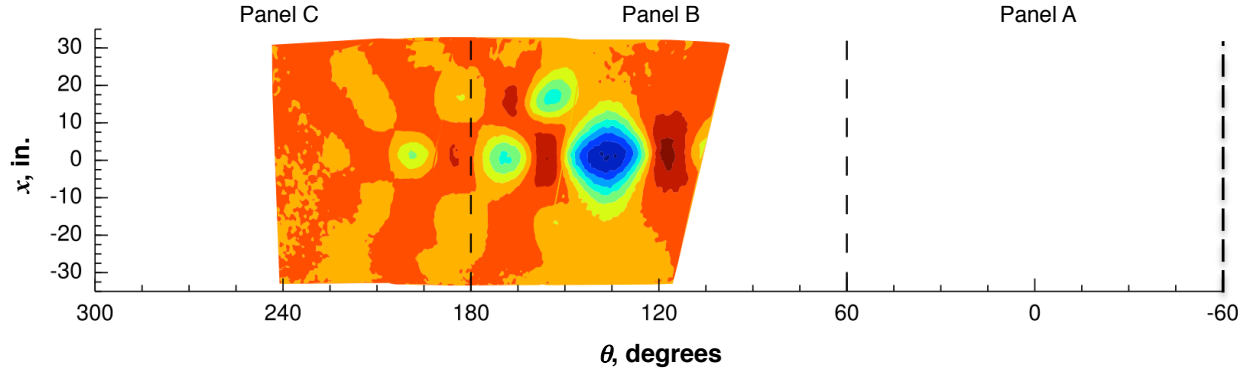


b) Buckling, $t = 0.0086$ seconds.

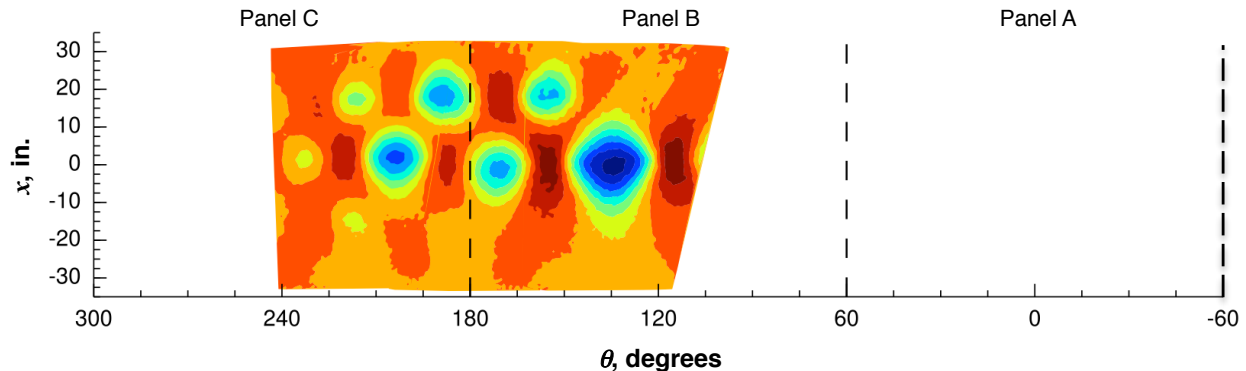


c) Buckling, $t = 0.0128$ seconds.

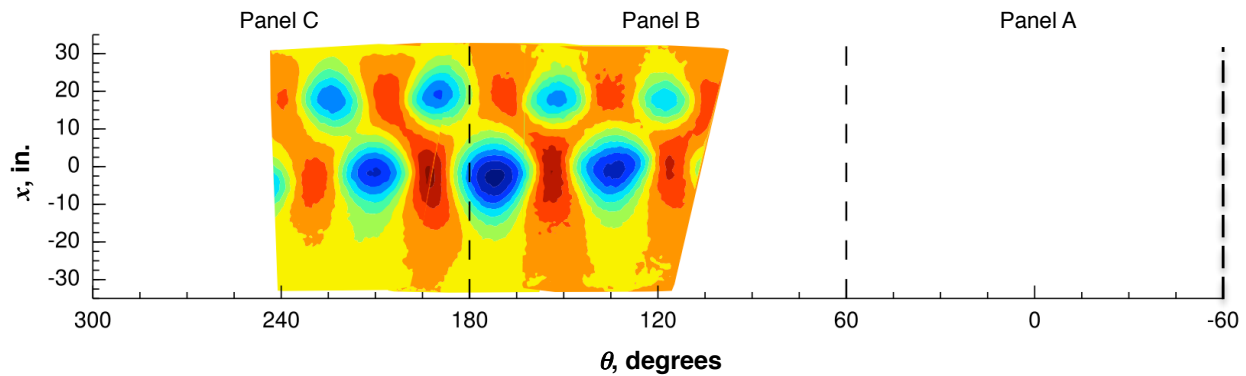
Figure 4.38. HS-DIC results illustrating the initiation and propagation of buckling deformations in TA02-LS5.



d) Buckling, $t = 0.0173$ seconds.



e) Buckling, $t = 0.0197$ seconds.



f) Initial postbuckling $t = 0.0312$ seconds.

Figure 4.38. Concluded.

4.3.3 Load versus Axial Strain Response

Predicted and measured prebuckling load versus axial-strain response curves are presented in Figs. 4.39 through 4.45. Negative strains correspond to compression. The buckling and postbuckling strains have been omitted from the figures so that the small-magnitude prebuckling strains may be observed. In addition, schematics of strain gage locations are provided in each figure. The objective of this strain data comparison is to help validate the predicted local response characteristics of the skin and stiffeners at various locations around the cylinder. First, back-to-back strain gage results from skin pockets and longitudinal stiffeners near the centers of panels A, B, and C, are shown in Figs. 4.39, 4.40 and 4.41, respectively. Similar results from

weld lands and adjacent longitudinal stiffeners for weld lands AB, BC, and CA, are presented in Figs. 4.42, 4.43, and 4.44, respectively. Finally, back-to-back strain gage results from two locations near the buckling initiation site in Panel B are shown in Fig. 4.45.

Back-to-back strain gage results from skin pockets and longitudinal stiffeners near the center of panels A, B, and C, are shown in Figs. 4.39, 4.40, and 4.41, respectively. Each figure contains analysis and test results from the center of a skin pocket near the center of each panel, corresponding to the black and red lines, and results from longitudinal stiffeners adjacent to each of these skin pockets, corresponding to the green and blue lines in the figures. The combined axial compression and bending loads applied in LS5 cause the maximum compression strains to occur in panels B and C and tension strains in Panel A, as expected. The measured results for Panel A indicate that the strain response is linear up to buckling with strains that range from $+345 \mu\epsilon$ to $+365 \mu\epsilon$. The strains at the center of panels B and C are significantly larger in magnitude than those in Panel A and range from approximately $-1000 \mu\epsilon$ to $-1400 \mu\epsilon$. Noticeable bending is observed in Panel B as indicated by the divergent load versus strain response curves and corresponds to the development of local bending deformations as shown in the displacement contours in Figs. 4.35 and 4.36. For the most part, the predicted and measured strain results agree well, however, the measured strains at the center of Panel B indicate more bending as compared to the corresponding predicted strains.

Back-to-back strain gage results from weld lands AB, BC, and CA and from longitudinal stiffeners adjacent to the weld lands, are shown in Figs. 4.42, 4.43, and 4.44, respectively. Each figure contains analysis and test results from the center of each weld land, corresponding to the black and red lines, and results from longitudinal stiffeners adjacent to each of the weld lands, corresponding to the green and blue lines in the figures. Overall, the predicted and measured strains agree well. The results indicate similar strain behavior as was seen in the skin pockets and stiffeners presented in Figs. 4.39 through 4.41 previously. The measured strains near weld lands AB and CA are similar in character and range from $-125 \mu\epsilon$ to $-245 \mu\epsilon$. The measured strains at weld land BC are aligned with the maximum compression load in the cylinder and range from $-1530 \mu\epsilon$ to $-1950 \mu\epsilon$. Bending in weld land BC is indicated by the diverging back-to-back strains results and corresponds to the onset of buckling in the TA. However, the predicted strains indicate slightly more bending than was observed in the test.

Predicted and measured strains from gage locations nearest the buckling initiation location are presented in Fig. 4.45. Buckling initiated in the cylinder wall near the location indicated by the red **X** symbol in the figure. The measured strain data are from two pairs of strain gages closest to the buckling initiation location. Strain gages 125OSA and 157ISA are back-to-back gages located in a skin pocket at $(+2.0 \text{ inches } 122.4^\circ)$, where (x, θ) denote axial and circumferential coordinate locations using the coordinate system defined in Fig. 2.7. Strain gages 126OSA and 158ISA are back-to-back skin pocket gages at $+2.0 \text{ inches } 151.1^\circ$. The measured results indicate a slightly nonlinear response up to approximately 250 kips. However, as the buckling load is approached in TA02-LS5, the measured load versus strain response for the OML skin gages, 125OSA and 126OSA, exhibit a strain reversal (i.e., reversing their initial prebuckling trend) associated with the onset of buckling in the TA. The corresponding predicted strains are also presented and indicate similar response trends, overall.

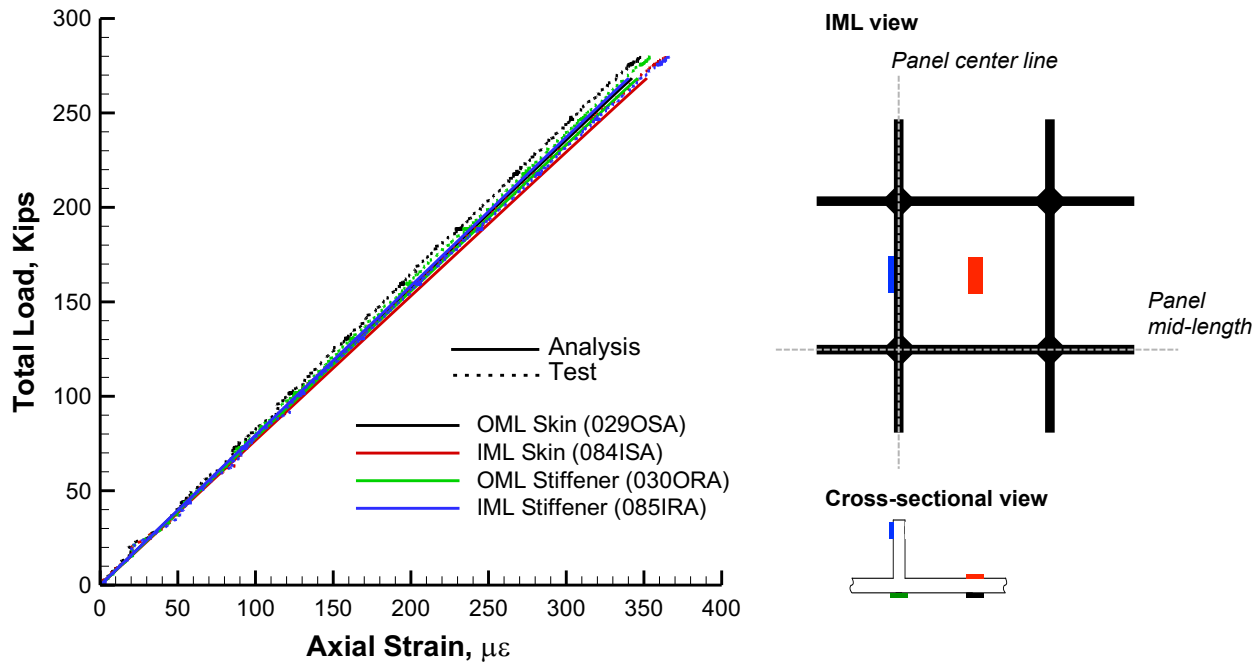


Figure 4.39. Predicted and measured back-to-back axial strains of skin and axial stiffener near center of Panel A. Panel A skin pocket: 029OSA/084ISA, Panel A stiffener: 030ORA/085IRA.

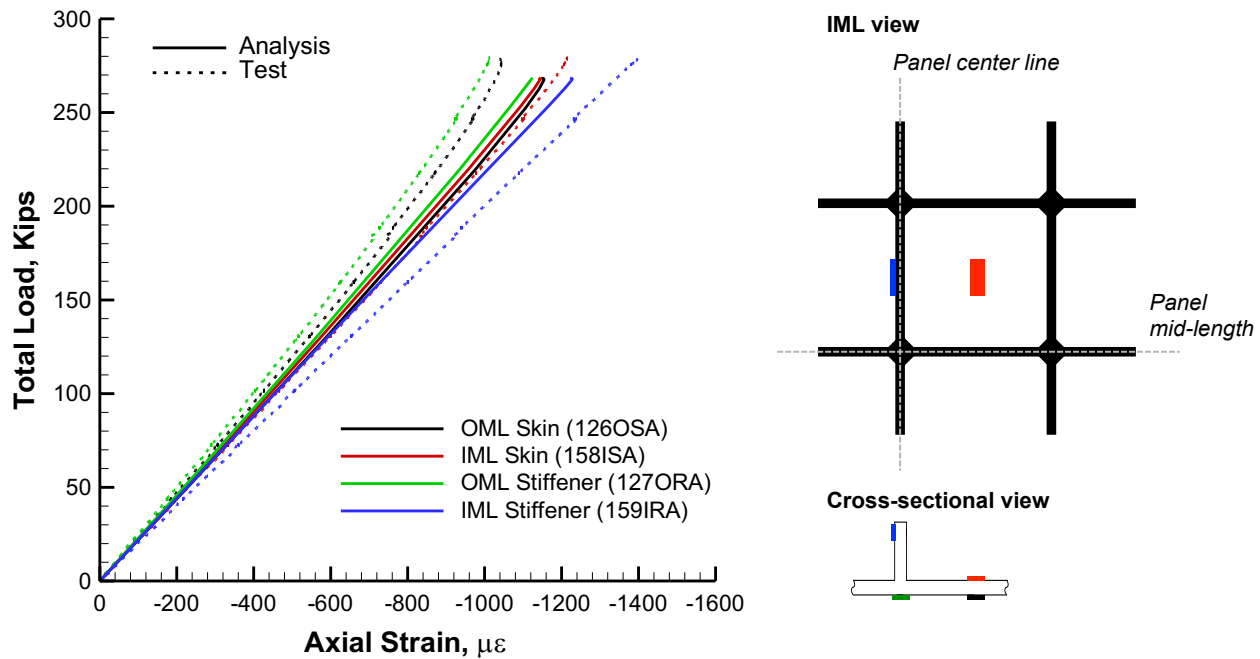


Figure 4.40. Predicted and measured back-to-back axial strains of skin and axial stiffener near center of Panel B. Panel B skin pocket: 126OSA/158ISA, Panel B stiffener: 127ORA/159IRA.

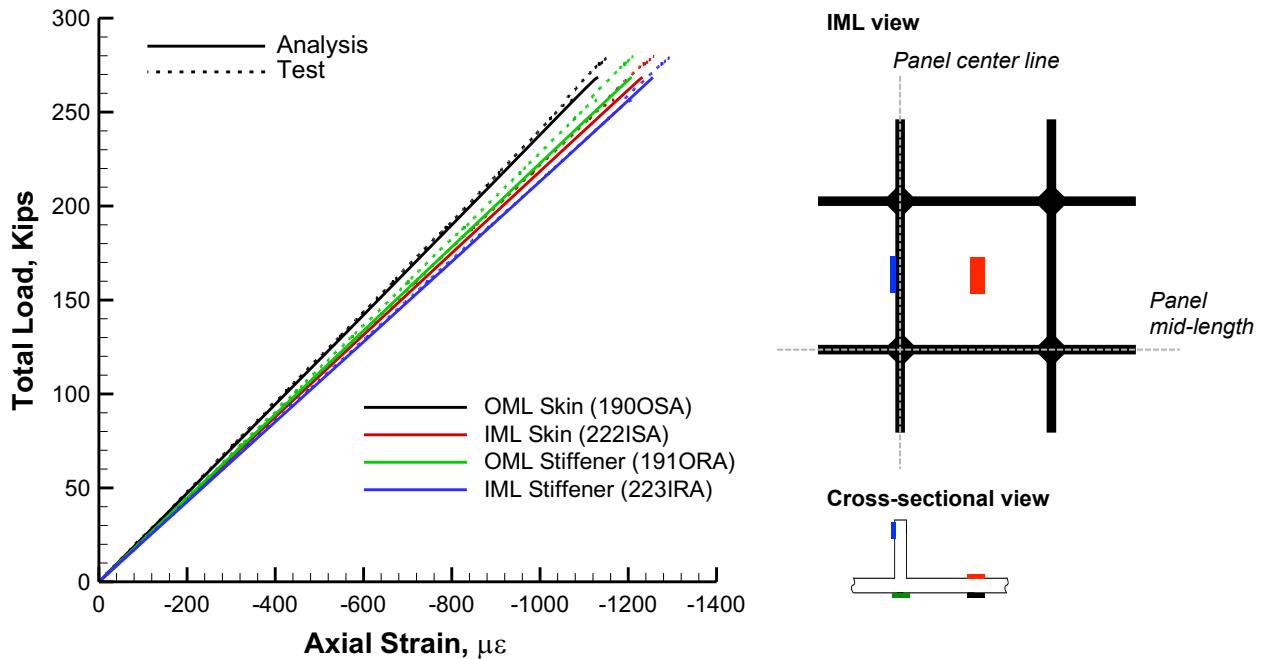


Figure 4.41. Predicted and measured back-to-back axial strains of skin and axial stiffener near center of Panel C. Panel C skin pocket: 190OSA/222ISA, Panel C stiffener: 191ORA/223IRA.

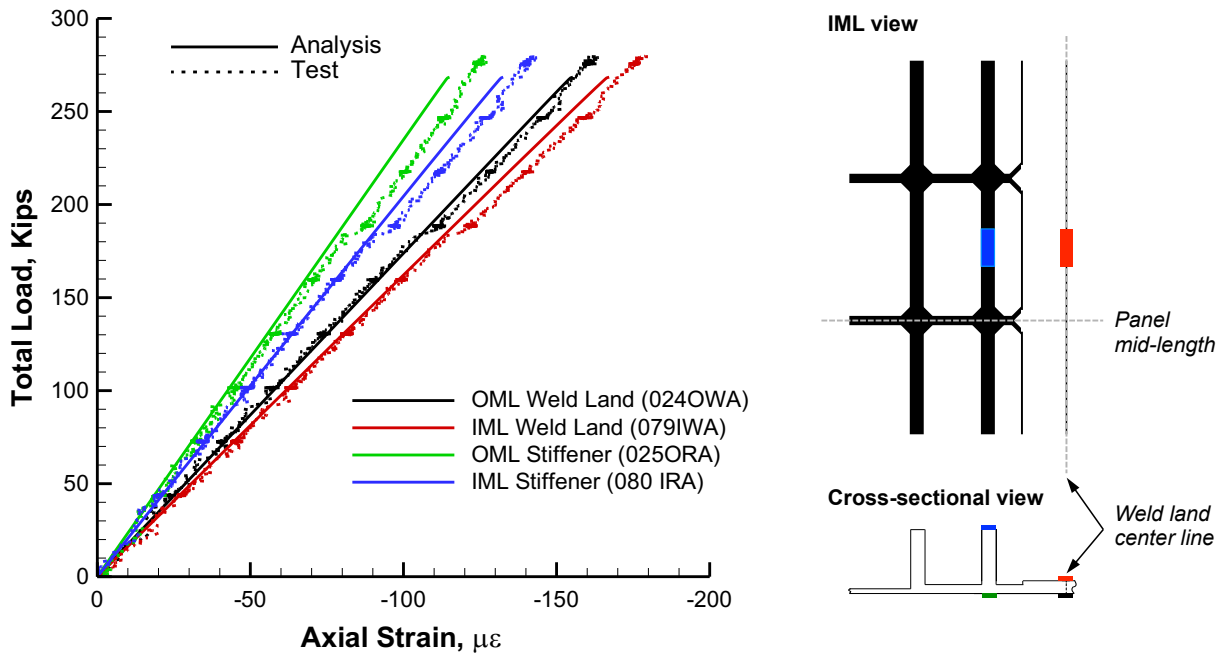


Figure 4.42. Predicted and measured back-to-back axial strains at center of weld land AB and adjacent axial stiffener. Weld land AB: 024OWA/079IWA, Panel A stiffener: 025ORA/080IRA.

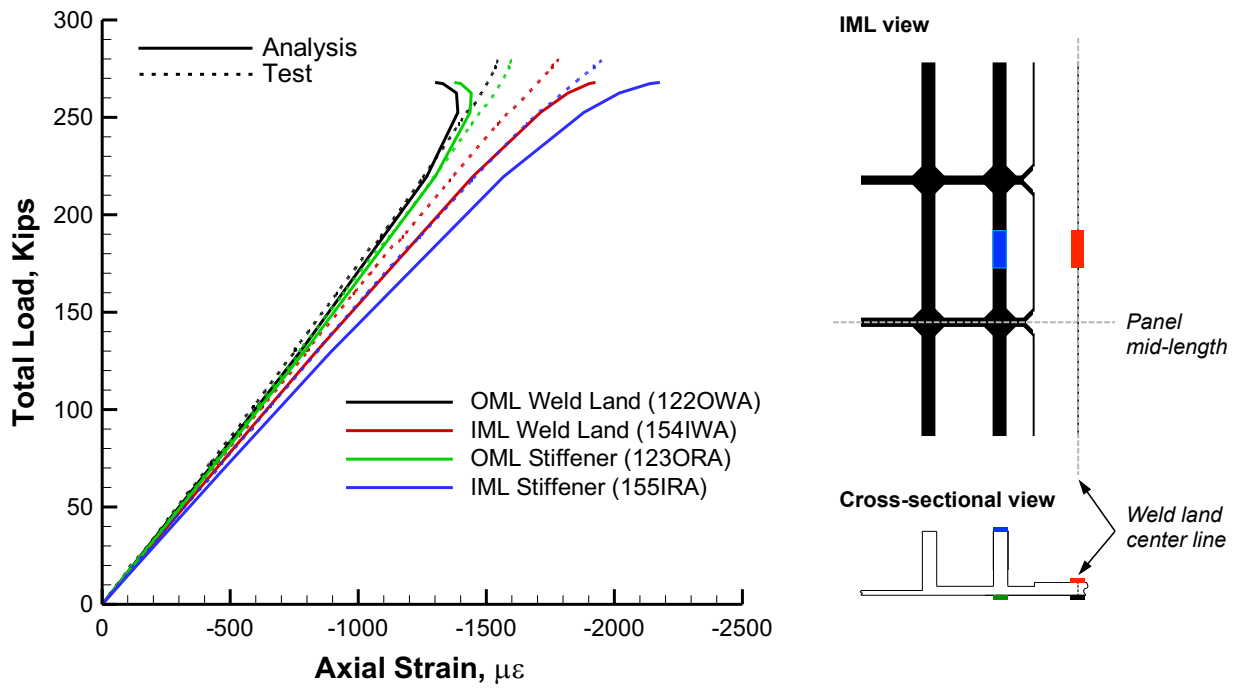


Figure 4.43. Predicted and measured back-to-back axial strains at center of weld land BC and adjacent axial stiffener. Weld land AB: 122OWA/154IWA, Panel B stiffener: 123ORA/155IRA.

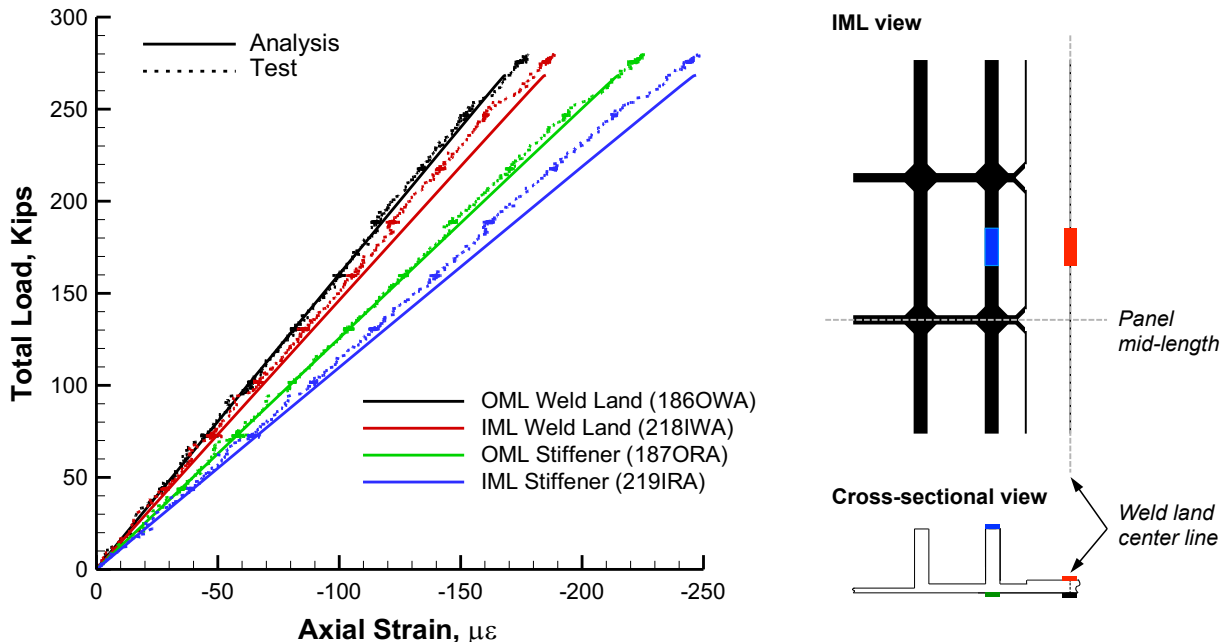


Figure 4.44. Predicted and measured back-to-back axial strains at center of weld land CA and adjacent axial stiffener. Weld land CA: 187OWA/219IWA, Panel C stiffener: 186ORA/218IRA.

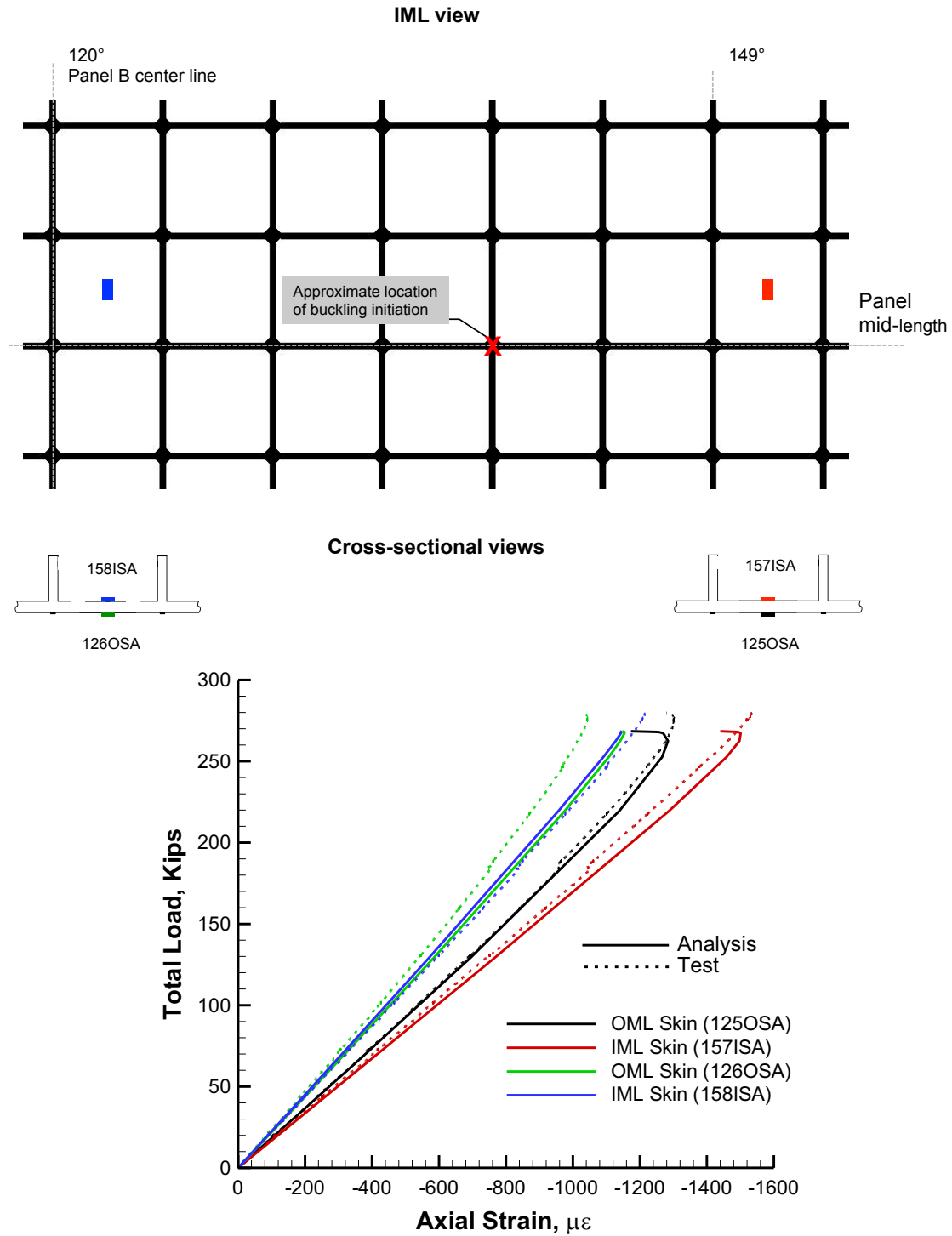


Figure 4.45. Predicted and measured back-to-back axial strains in selected Panel B skin pockets.

4.3.4 Axial Strain Distribution

Selected plots of the predicted and measured axial membrane strain distribution around the circumference of the test article are presented for several prebuckling load levels and incipient buckling in Figs. 4.46 through 4.49. Each plot includes data from five different axial locations

along the length of the test article including, +32.84 inches, +18.0 inches, +2.0 inches, -8.0 inches, and -32.84 inches. The predicted membrane strains are displayed as solid lines and the measured strains from individual strain gages are plotted with open circle symbols. The measured membrane strains are obtained by taking the average of the back-to-back strain gage pairs. The dashed vertical lines at 60° , 180° , and -60° mark the weld land locations. The objectives of this strain data comparison are to assess the load distribution in the test article and to validate predicted results.

At a load level of 72.8 kips (25% classical buckling load), the strains exhibit a sinusoidal distribution around the circumference of the cylinder as shown in Fig. 4.46 and are consistent with the application of a combined axial compression and bending load. The maximum compression strains occur at $\theta = 180^\circ$ and range from $-390 \mu\epsilon$ near the ends of the cylinder to $-460 \mu\epsilon$ at its mid length. Small magnitude tensile strains occur at 0° in Panel A and are between $70 \mu\epsilon$ to $90 \mu\epsilon$. The short wave-length variation in the strain distribution near the boundary (see Figs. 4.46a and 4.46e) is associated with the local stiffness variation of the skin and stiffener construction.

As loading increases up to 159.6 kips (55% classical buckling load) and 246.3 kips (85% classical buckling load), the global strain distributions (see Figs. 4.47 and 4.48) remain similar to those shown in Fig. 4.46 with maximum compression strains increasing to approximately $-1600 \mu\epsilon$ as shown in Fig. 4.51c. In addition, a sinusoidal variation in the strain distribution appears near the mid-length of panels B and C (Figs. 4.47c and 4.48c) and is associated with formation of localized bending deformations in the cylinder wall as shown in the displacement contours in Fig. 4.36.

Predicted and measured strain distributions incipient to buckling are presented in Fig. 4.49. The predicted strains at 267.6 kips (92% classical buckling load) are displayed as a solid line and the corresponding measured strains are plotted with open circle symbols. In addition, the measured strains incipient to buckling at 279.7 kips (96% classical buckling load) are presented and displayed as filled square symbols. The strain distributions, for the most part, continue to follow the trends observed at lower prebuckling load levels; however, the measured and predicted results at the mid-length indicate an increase in the magnitude of the strain variation near the location of buckling initiation (see Fig. 4.49c between $\theta = 120^\circ$ and 150°).

Overall, the predicted and measured strain distribution agrees well and indicates that the loading into the TA is modeled accurately.

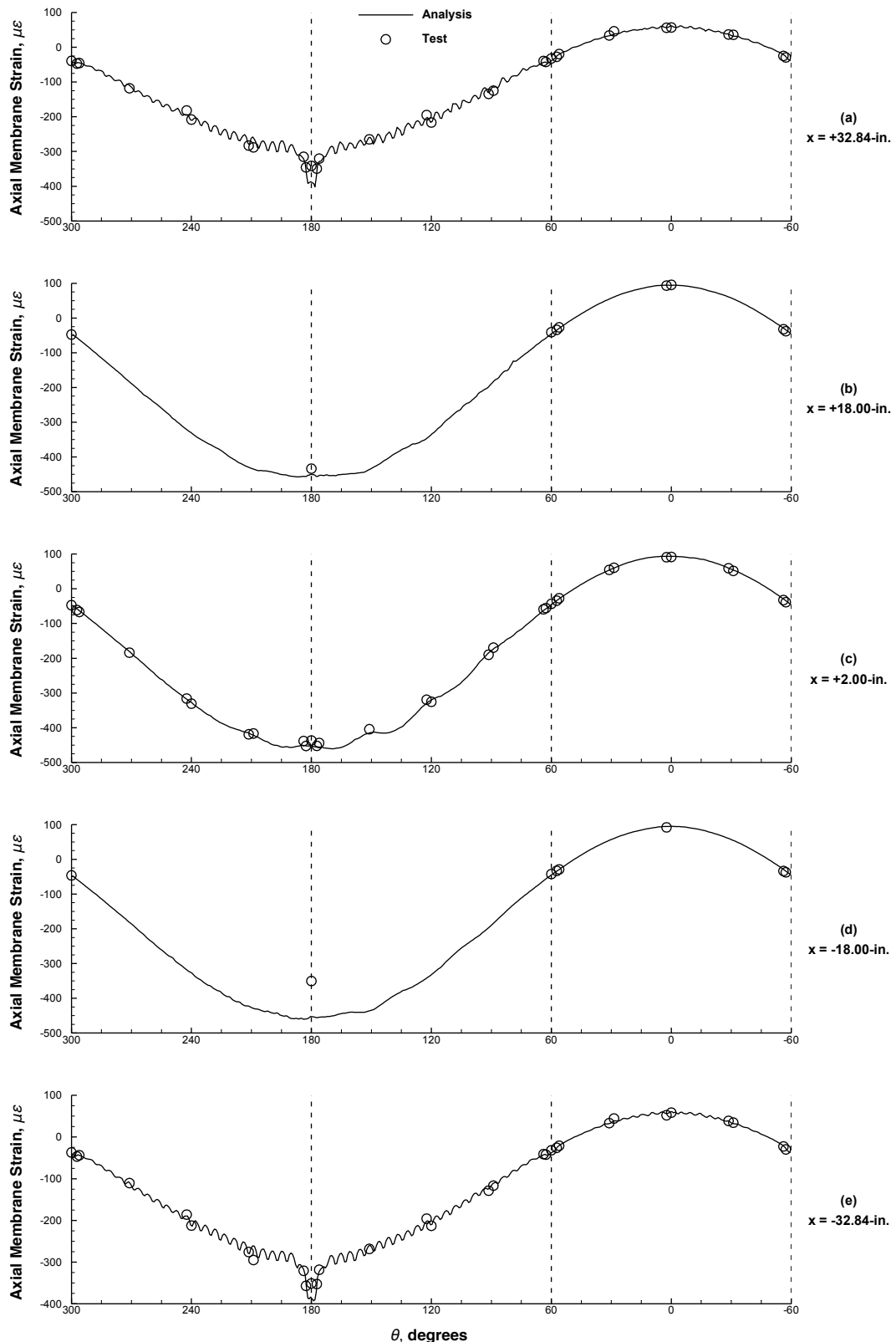


Figure 4.46. Predicted and measured axial membrane strain distribution around circumference, 72.8 kips (25% classical buckling load).

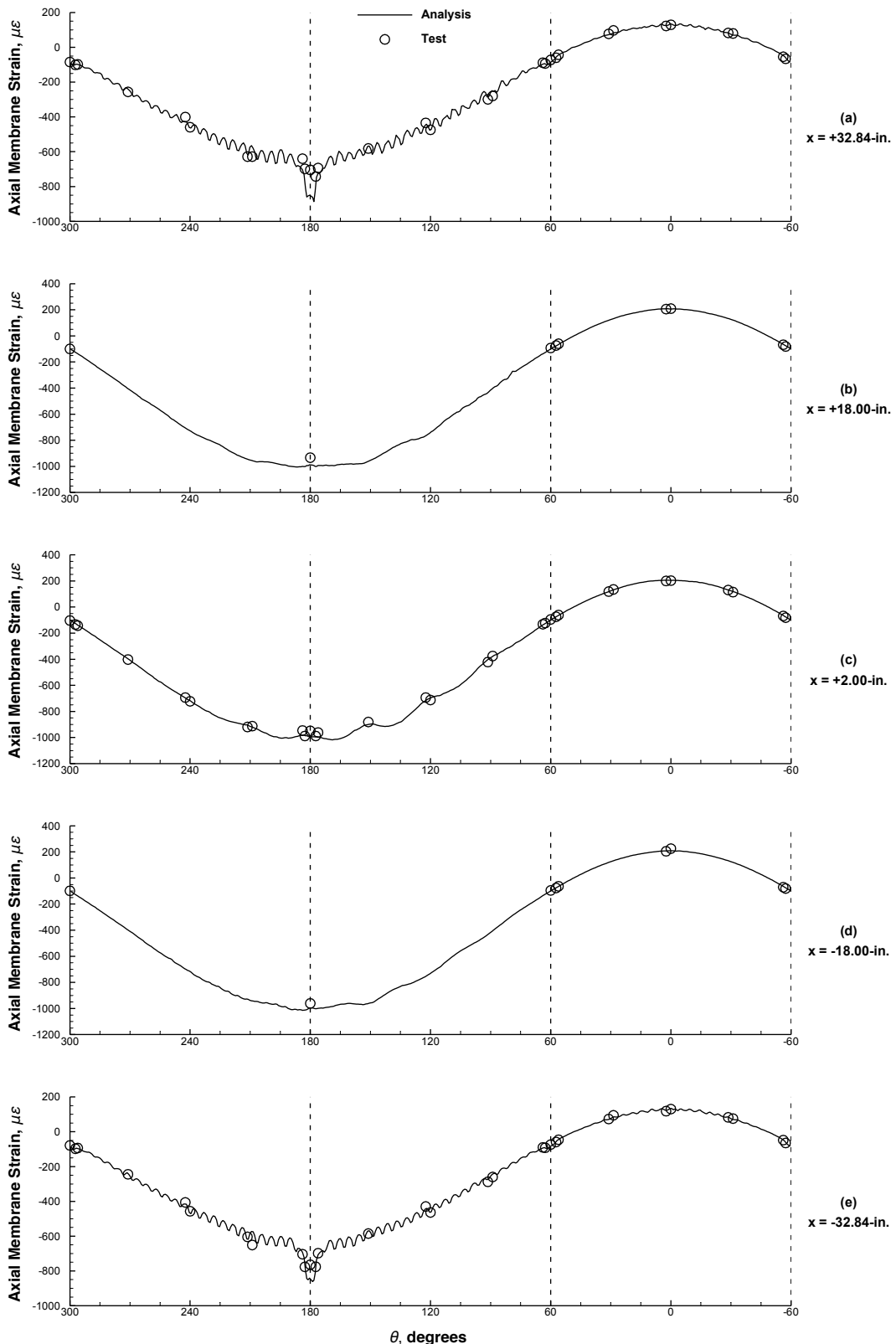


Figure 4.47. Predicted and measured axial membrane strain distribution around circumference, 159.6 kips (55% classical buckling load).

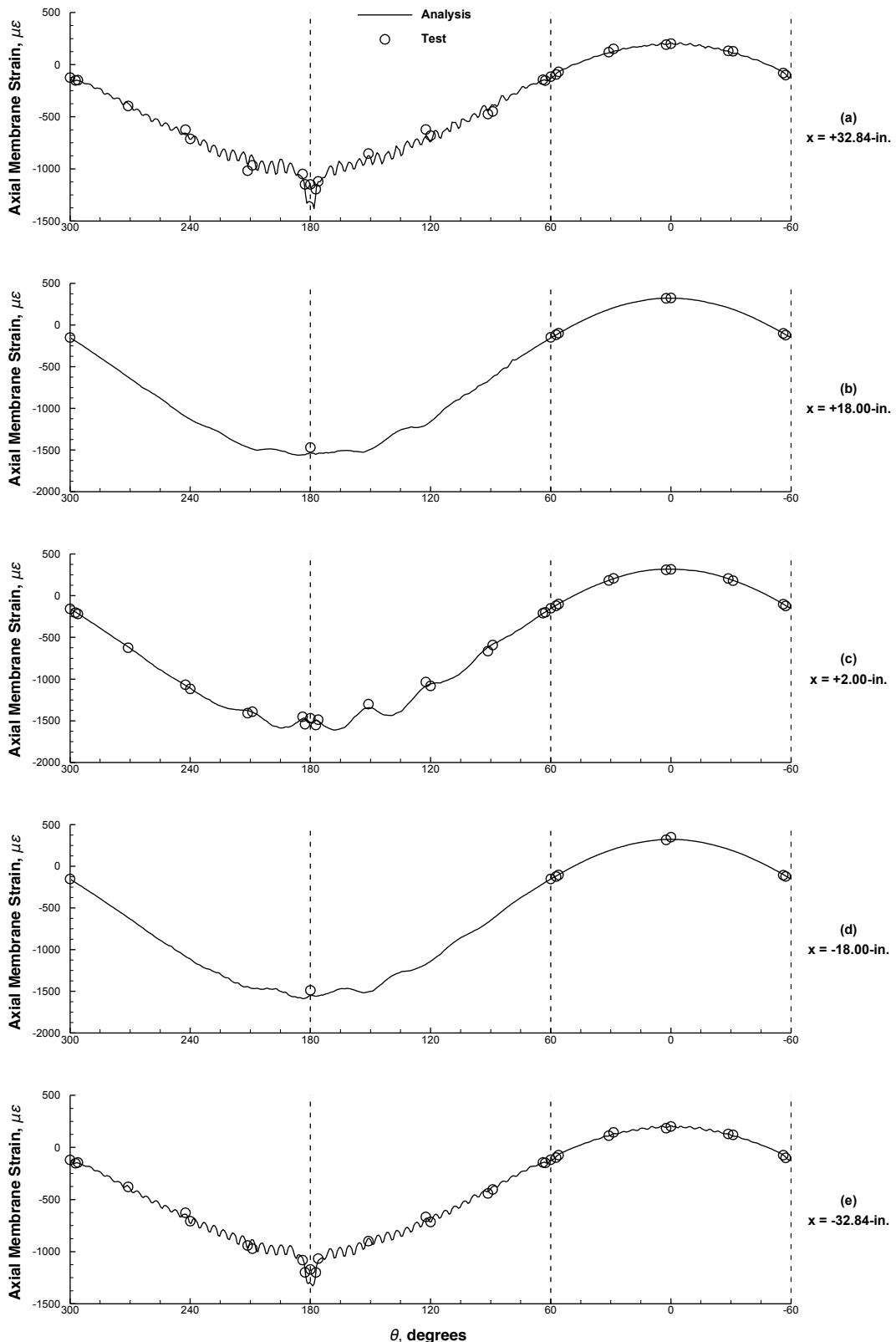


Figure 4.48. Predicted and measured axial membrane strain distribution around circumference, 246.8 kips (85% classical buckling load).

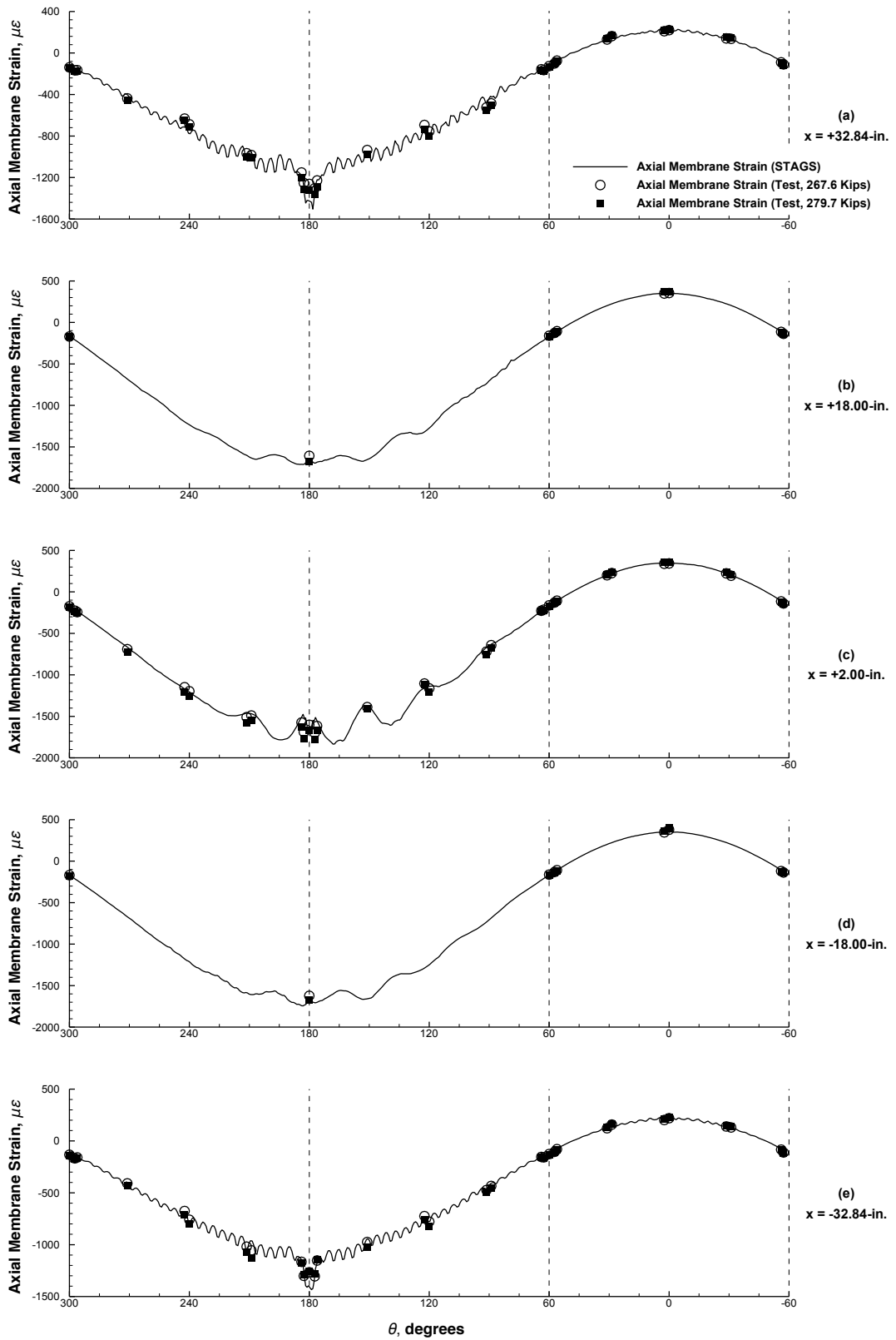


Figure 4.49. Predicted and measured axial membrane strain distribution around circumference incipient to buckling.

5.0 Concluding Remarks

Predicted and measured results for the 8-foot-diameter Al-Li orthogrid-stiffened cylinder TA02 are presented. TA02 was the second in a series of eight subscale, integrally stiffened barrels defined in the SBKF test program. The test of TA02 was conducted on February 3–6, 2009 at MSFC. The primary objectives of this test were to verify the performance of a new purpose-built test facility, verify the adequacy of the test procedures, and verify the test article design and analysis approach through detailed test and analysis correlation. To this end, selected results from the testing of TA02 were presented. First, descriptions of the test article design, fabrication, and test are presented and pretest analysis predictions are briefly described. Then, selected test results are presented and compared to pretest predictions.

Test Objectives and Success Criteria

All test objectives were successfully achieved and, for the most part, the test was executed as defined by the test plan and test procedure. Specifically, the test system and instrumentation operated as desired and the test article was tested to buckling and into the postbuckling range of loading. In addition, all test data necessary to verify the test article design and analysis approach were obtained; however, one of the HS-DIC systems failed to capture images of the transient collapse event during one of the load sequences. Fortunately, the HS-DIC data that were obtained for that load sequence, and presented herein, were sufficient to characterize the initiation and propagation of the buckling response as required.

Test Results and Pretest Predictions

During testing, TA02 was subjected to two different load sequences to failure. Both load sequences applied a combination of axial compression and bending loads; first, with the maximum compression load being applied over the center of Panel A at $\theta = 0^\circ$ until buckling (LS4) and then over weld land BC at $\theta = 180^\circ$ until buckling (LS5). During both load sequences, TA02 exhibited a linear prebuckling load versus end-shortening response, and achieved maximum total loads of 286.2 kips (LS4) and 279.7 kips (LS5) for the two different loading sequences. Full-field low-speed DIC and HS-DIC displacement data indicated that both buckling events initiated as a single ellipse-shaped dimple in the cylinder wall and led to the sudden buckling of the TA. Buckling of the cylinder resulted in a significant reduction in axial load carrying capability and effective axial stiffness. In addition, the TA exhibited material yielding due to the development of large-magnitude bending deformations in the shell wall during the buckling response.

Overall, the pretest predictions showed good correlation with the measured prebuckling, buckling, and postbuckling behavioral characteristics of TA02 and indicate that the modeling approach used can produce physically meaningful results that are suitable for pretest predictions and test planning. In particular, the pretest predictions indicated similar load versus displacement and load versus strain response trends including an accurate representation of the axial stiffness and axial strain distribution around the circumference of the cylinder (within $\pm 5\%$ difference). In addition, the overall character of the prebuckling full-field radial displacements agreed well with the measured DIC displacements including the development of a single ellipse-shaped dimple that initiated a transient buckling response. However, the predicted prebuckling radial displacement amplitudes were typically greater than the corresponding measured displacements. In addition, the analyses of the two failure load sequences predicted buckling loads of 258.1 kips

(LS4) and 267.6 kips (LS5) which are approximately 9.8% and 4.3% lower than the corresponding measured values, respectively. It is not known at this time what has caused the differences between the predicted and measured radial displacement amplitudes and buckling loads; however, it is likely that several of the modeling assumptions used in the pretest analysis may have some influence.

Future Work

Future detailed analysis studies will be performed to determine the effects of selected modeling assumptions on the predicted response and improve the test and analysis correlation. For example, the TA stiffeners were modeled with beam elements which cannot predict rolling displacements of the stiffener blade (i.e., the displacement of the stiffener mid-surface out of the undeformed plane). Omitting this displacement mode could cause discrepancies in local stiffness and load distributions in the TA model. Similarly, the fillets at the intersection between the stiffeners and the skin and the fillets at the intersections between the circumferential and longitudinal stiffeners (often referred to as nodes; see Section 2.2) were omitted from the model for simplicity. These fillet details can contribute additional bending and torsional stiffness to the stiffener and skin, which could reduce the predicted prebuckling radial displacements in the shell wall and increase the predicted buckling load. In addition, the models assume idealized boundary conditions in which the ends of the TA are rigidly clamped in the attachment rings. The actual as-tested boundary conditions consisted of the TA potted in a low-melting-temperature alloy (see Section 2.3) that may allow some rotation of the TA in the attachment ring due to the relatively low stiffness of the potting and thus change the local bending response in the TA. Finally, the effects of manufacturing tolerances associated with the as-built skin and stiffener dimensions should be investigated.

Archival Information

A complete listing of all test and analysis data, data files, and drawings is provided in Appendix A and includes archival directory names, file names and file format descriptions, and example data plots. All data, reports, drawings, and other supporting materials for TA02 design, fabrication, and testing will be located in the SBKF_TA02_Archive directory in the SBKF Archive Directory on the NASA Langley central storage system (CSS) and the NES NASA Safety Center Knowledge Now (NSCKN) storage site once the SBKF project is complete.

6.0 References

1. Hilburger, M. W.; and Thornburgh, R. P.: *Shell Buckling Knockdown Factor Program SBKF-P2-CYL-SD02 Test Plan v1.1.*, NASA Langley Research Center, Hampton, VA, 28 January 2009.
2. Roberts, M. G.: *Test and Checkout Procedure: Shell Buckling Knockdown Factor (SBKF) Test #2.* TCP-ED30.1.MGR.102708, NASA Marshall Space Flight Center, Huntsville, AL, February 3, 2009.
3. Hilburger, M. W.; Waters, W. A.; and Haynie, W. T.: *Buckling Test Results from the 8-Foot-Diameter Orthogrid-Stiffened Cylinder Test Article TA01.* NASA/TP-2015-218785, August 2015.
4. Thornburgh, R. P.; and Hilburger, M. W.: *Design of Orthogrid Cylinder Test Articles for the Shell Buckling Knockdown Factor Assessment.* NASA/TM-2010-216866 and ARL-TR-5122, November 2010.
5. Weingarten, V.; Seidi, P.; and Peterson, J. P.: *Buckling of Thin-Walled Circular Cylinders.* NASA SP-8007, September 1965, revised August 1968.
6. Drawing No. 1167189, Revision B: *Panels Checkout Test Panel.* NASA Langley Research Center, Hampton, VA, 19 March 2008.
7. Bjorkman, G.: *TD 6456F NASA LaRC Shell Buckling Knockdown Factor Assessment Support: Task 3 - Barrel Fabrication.* ETTP-3913-08-001, June 11, 2008.
8. Drawing No. 1238206: *NESC Shell Buckling Test Barrel Assembly.* NASA Langley Research Center, Hampton, VA, 17 March 2009.
9. Drawing No. 1238205, Revision B: *NESC Shell Buckling Test Panel Mounting Ring.* NASA Langley Research Center, Hampton, VA, March 17, 2009.
10. Drawing 90M12370: *Test Assembly.* NASA Marshall Space Flight Center, Huntsville, AL, 28 October 2008.
11. Drawing 90M12375: *Load Structure Assembly.* NASA Marshall Space Flight Center, Huntsville, AL, 20 February 2008.
12. Drawing No. 1238207, Revision B: *NESC Shell Buckling Test Checkout Test Panel Instrumentation.* NASA Langley Research Center, Hampton, VA, 22 July 2008.
13. Rankin, C. C.; Brogan, F. A.; Loden, W. A.; and Cabiness, H. D.: *STAGS User's Manual, Version 5.0.* Lockheed Martin Missiles & Space Co., Inc., Advanced Technology Center, Report LMSC P032594, January 2005.
14. Hastings, K.; and Malone, T. W.: "Design Allowables Handbook for Aluminum-Lithium 2195 Plates, Extrusions, forgings, & Welds." MSFC-HDBK-3513, December 2007.
15. Thornburgh, R. P.; and Hilburger, M. W.: *Pre-Test Analysis Predictions for the Shell Buckling Knockdown Factor Checkout Tests – TA01 and TA02.* NASA/TM-2011-216875 ARL-TR-5123, January 2011.

Appendix A Archive Information

All electronic files associated with the testing of TA02 are stored in the SBKF Data Archive located on the NASA Langley central storage system (CSS) and the NESC NASA Safety Center Knowledge Now (NSCKN) storage site. These files include all test data, manufacturing plan, test plan, test procedure, test article and test facility drawings, quality assurance reports and data, finite-element results, and selected processed data and plots. The electronic files are listed in this section along with a short description of the format of the files. File names and directory paths are indicated in Arial font throughout the Appendix for clarity.

A.1 Plans, Procedures, Drawings and Reports

TA02 plans, procedures, drawing files and reports are found in SBKF_TestData_Archive > TA02 > Docs. Files include:

Plans and Procedures

TA02 Test Plan: SBKF-P2-CYL-SD02-TestPlan_v1.1.pdf

TA02 Test Procedure: TCP-ED30.1-MGR-020209.pdf

TA02 Manufacturing Plan: ETTP-3913-08-001.pdf

Drawings

Barrel Panel Design Drawing: 1167189 Rev. B

Barrel Test Article Attachment Ring Drawing: 1238205 Rev. A

Barrel Test Article Assembly Drawing: 1238206

Instrumentation Pattern Drawing: 1238207 Rev. B

Load Structure Assembly Drawing: 90M12375

Test Assembly Drawing: 90M12370

Quality and Manufacturing Reports

Material Requirements Report: EC-012200_STM11A1-4.pdf

Material Qualification Report: SBKF_Material_Qualification.pdf

A.2 TA02 Measured Geometry

The initial geometry of TA02 was measured after fabrication was complete and before instrumentation was installed. The raw data were provided in global Cartesian coordinates and was converted to cylindrical coordinates. The data were then fit to a best-fit circular cylinder and the deviations from the perfect OML cylinder radius were calculated and denoted by the variable *imp* as shown in Fig. 2.6. The resulting test-article geometry data are reported in *x*, θ , *imp* column format, where *x* and θ are the OML coordinates as defined in Fig. 2.7 and *imp* is the measured deviation.

The measured data are found in SBKF_TestData_Archive > MeasuredGeometry_Data. Files include:

TA02 measured imperfection data file: TA02_imp.dat

Fortran subroutine used to input the geometry data into the FEM: TA02_dimp.F

TA02 measured imperfection plot (Fig. 2.6): TA02_imp.jpg

A.3 Test Data

Test data for all load sequences conducted during the testing of TA02 have been archived. Archived test data and plots for LS5 are described in this section; however, similar data are available for the other load sequences in the archives and follows a similar directory and file name format. The data can be found in the following directories:

Load Sequence 1 Data: SBKF_TestData_Archive > TA02 > LS_1

Load Sequence 2 Data: SBKF_TestData_Archive > TA02 > LS_2

Load Sequence 3 Data: SBKF_TestData_Archive > TA02 > LS_3

Load Sequence 4 Data: SBKF_TestData_Archive > TA02 > LS_4

Load Sequence 5 Data: SBKF_TestData_Archive > TA02 > LS_5

A.3.1 Raw Test Data Files

The raw test data for the five load sequences in standard text format in the SBKF Data Archive in the following directory and file structure (LS5 is used as an example): SBKF_TestData_Archive > TA02 > LS_5 > Raw_Test_Data >

Text files:

Shell Buckling LS5 DB1 11_21-2008 - EU1of3 - 11-20-2008.txt

Shell Buckling LS5 DB1 11_21-2008 - EU2of3 - 11-20-2008.txt

Shell Buckling LS5 DB1 11_21-2008 - EU3of3 - 11-20-2008.txt

Shell Buckling LS5 DB1 11_21-2008 - LPS1of3 - 11-20-2008.txt

Shell Buckling LS5 DB1 11_21-2008 - LPS2of3 - 11-20-2008.txt

Shell Buckling LS5 DB1 11_21-2008 - LPS3of3 - 11-20-2008.txt

The “EU” (Engineering Units) series files are full test data sets and are separated into three files due to the size limitations of the software. The “LPS” (Load Point Scans) series files contain the tagged scan data. Tagged scan data refers to a subset of the full data set in which data are saved at specific times during the test, typically at prescribed load levels defined in the test plan and after prominent response events during the test such as buckling. All data channels are clearly labeled in the files and are consistent with the name and labeling convention in drawings and other related documents.

A.3.2 Digital Image Correlation Data Files and Contour Plots

Only a subset of the total DIC images were processed into data due to the extensive number of images collected during the testing. However, all images, calibration, and data files have been retained for future processing if necessary. Selected files for DIC data and predicted data are listed in Tables A3 and A4 and include finite-element model analysis load step, DIC photo number, raw test data scan number, and corresponding data file names. The raw image files (.tiff files) and processed DIC data are located in the SBKF Data Archive in the following directory: SBKF_TestData_Archive > TA02 > LS_5 > DIC-3D_Data > Images_Data. Calibration data and information is located in SBKF_TestData_Archive > TA02 > LS_5 > DIC-3D_Data > Calibration. The image file names include the camera location names defined in Fig. 2.13, e.g., DIC1, DIC2, DIC3, etc.

A.3.3 High-Speed Video

High-speed camera cine files are stored on the SBKF Data Archive in the following directory: SBKF_TestData_Archive > TA02 > LS_5 > DIC-3D_Data > High-Speed_Video. The cine file names include the camera location names defined in Fig. 2.13, e.g., HS-DIC1, HS-DIC2, HS-DIC3, etc.

A.3.4 Photos and Video

Low-resolution and high-resolution photos and video of the test setup and test control room were taken February 3–6, 2009 during testing. The photos can be found in the following directory: SBKF_TestData_Archive > TA02 > Photos. Video can be found in the following directory: SBKF_TestData_Archive > TA02 > Video

Table A1. Strain Gage Locations and Orientations for TA02

OML GAGE NUMBER	OML GAGE ID	IML GAGE NUMBER	IML GAGE ID	HOOP DIMENSION, (in.)	AXIAL DIMENSION, (in.)	PANEL	LOCATION	ORIENTATION
1	001OWA	56	056IWA	50.27	-32.84	A	Weld	Axial
2	002ORA	57	057IRA	48.00	-32.84	A	Stiffener	Axial
3a	003OSA	58a	058ISA	47.00	-32.84	A	Pocket	Axial
3b	003OSH	58b	058ISH	47.00	-32.84	A	Pocket	Hoop
4	004OSA	59	059ISA	26.00	-32.84	A	Pocket	Axial
5	005ORA	60	060IRA	24.00	-32.84	A	Stiffener	Axial
6a	006OSA	61a	061ISA	2.00	-32.84	A	Pocket	Axial
6b	006OSH	61b	061ISH	2.00	-32.84	A	Pocket	Hoop
7	007ORA	62	062IRA	0.00	-32.84	A	Stiffener	Axial
8	008ORA	63	063IRA	-24.00	-32.84	A	Stiffener	Axial
9	009OSA	64	064ISA	-26.00	-32.84	A	Pocket	Axial
10a	010OSA	65a	065ISA	-47.00	-32.84	A	Pocket	Axial
10b	010OSH	65b	065ISH	-47.00	-32.84	A	Pocket	Hoop
11	011ORA	66	066IRA	-48.00	-32.84	A	Stiffener	Axial
12	012OSH	67	067IRH	47.00	-32.00	A	Rib	Hoop
13	013OSH	68	068IRH	2.00	-32.00	A	Rib	Hoop
14	014OSH	69	069IRH	-47.00	-32.00	A	Rib	Hoop
15	015OWA	70	070IWA	50.27	-18.00	A	Weld	Axial
16	016ORA	71	071IRA	48.00	-18.00	A	Stiffener	Axial
17	017OSA	72	072ISA	47.00	-18.00	A	Pocket	Axial
18	018OSA	73	073ISA	2.00	-18.00	A	Pocket	Axial
19	019ORA	74	074IRA	0.00	-18.00	A	Stiffener	Axial
20	020OSA	75	075ISA	-47.00	-18.00	A	Pocket	Axial
21	021ORA	76	076IRA	-48.00	-18.00	A	Stiffener	Axial
22	022ORH	77	077IRH	47.00	0.00	A	Rib	Hoop
23	023ORH	78	078IRH	-47.00	0.00	A	Rib	Hoop
24	024OWA	79	079IWA	50.27	2.00	A	Weld	Axial
25	025ORA	80	080IRA	48.00	2.00	A	Stiffener	Axial

Table A1. Continued

OML GAGE NUMBER	OML GAGE ID	IML GAGE NUMBER	IML GAGE ID	HOOP DIMENSION, (in.)	AXIAL DIMENSION, (in.)	PANEL	LOCATION	ORIENTATION
26a	026OSA	81a	081ISA	47.00	2.00	A	Pocket	Axial
26b	026OSH	81b	081ISH	47.00	2.00	A	Pocket	Hoop
27	027OSA	82	082ISA	26.00	2.00	A	Pocket	Axial
28	028ORA	83	083IRA	24.00	2.00	A	Stiffener	Axial
29	029OSA	84	084ISA	2.00	2.00	A	Pocket	Axial
30	030ORA	85	085IRA	0.00	2.00	A	Stiffener	Axial
31	031ORA	86	086IRA	-24.00	2.00	A	Stiffener	Axial
32	032OSA	87	087ISA	-26.00	2.00	A	Pocket	Axial
33a	033OSA	88a	088ISA	-47.00	2.00	A	Pocket	Axial
33b	033OSH	88b	088ISH	-47.00	2.00	A	Pocket	Hoop
34	034ORA	89	089IRA	-48.00	2.00	A	Stiffener	Axial
35	035OWA	90	090IWA	50.27	18.00	A	Weld	Axial
36	036ORA	91	091IRA	48.00	18.00	A	Stiffener	Axial
37	037OSA	92	092ISA	47.00	18.00	A	Pocket	Axial
38	038OSA	93	093ISA	2.00	18.00	A	Pocket	Axial
39	039ORA	94	094IRA	0.00	18.00	A	Stiffener	Axial
40	040OSA	95	095ISA	-47.00	18.00	A	Pocket	Axial
41	041ORA	96	096IRA	-48.00	18.00	A	Stiffener	Axial
42	042ORH	97	097IRH	47.00	32.00	A	Rib	Hoop
43	043ORH	98	098IRH	2.00	32.00	A	Rib	Hoop
44	044ORH	99	099IRH	-47.00	32.00	A	Rib	Hoop
45	045OWA	100	100IWA	50.27	32.84	A	Weld	Axial
46	046ORA	101	101IRA	48.00	32.84	A	Stiffener	Axial
47a	047OSA	102a	102ISA	47.00	32.84	A	Pocket	Axial
47b	047OSH	102b	102ISH	47.00	32.84	A	Pocket	Hoop
48	048OSA	103	103ISA	26.00	32.84	A	Pocket	Axial
49	049ORA	104	104IRA	24.00	32.84	A	Stiffener	Axial
50a	050OSA	105a	105ISA	2.00	32.84	A	Pocket	Axial

Table A1. Continued

OML GAGE NUMBER	OML GAGE ID	IML GAGE NUMBER	IML GAGE ID	HOOP DIMENSION, (in.)	AXIAL DIMENSION, (in.)	PANEL	LOCATION	ORIENTATION
50b	050OSH	105b	105ISH	2.00	32.84	A	Pocket	Hoop
51	051ORA	106	106IRA	0.00	32.84	A	Stiffener	Axial
52	052ORA	107	107IRA	-24.00	32.84	A	Stiffener	Axial
53	053OSA	108	108ISA	-26.00	32.84	A	Pocket	Axial
54a	054OSA	109a	109ISA	-47.00	32.84	A	Pocket	Axial
54b	054OSH	109b	109ISH	-47.00	32.84	A	Pocket	Hoop
55	055ORA	110	110IRA	-48.00	32.84	A	Stiffener	Axial
111	111OWA	143	143IWA	50.27	-32.84	B	Weld	Axial
112	112ORA	144	144IRA	48.00	-32.84	B	Stiffener	Axial
113	113OSA	145	145ISA	47.00	-32.84	B	Pocket	Axial
114	114OSA	146	146ISA	26.00	-32.84	B	Pocket	Axial
115	115OSA	147	147ISA	2.00	-32.84	B	Pocket	Axial
116	116ORA	148	148IRA	0.00	-32.84	B	Stiffener	Axial
117	117ORA	149	149IRA	-24.00	-32.84	B	Stiffener	Axial
118	118OSA	150	150ISA	-26.00	-32.84	B	Pocket	Axial
119	119OSA	151	151ISA	-47.00	-32.84	B	Pocket	Axial
120	120ORA	152	152IRA	-48.00	-32.84	B	Stiffener	Axial
121	121OWA	153	153IWA	50.27	-18.00	B	Weld	Axial
122	122OWA	154	154IWA	50.27	2.00	B	Weld	Axial
123	123ORA	155	155IRA	48.00	2.00	B	Stiffener	Axial
124	124OSA	156	156ISA	47.00	2.00	B	Pocket	Axial
125	125OSA	157	157ISA	26.00	2.00	B	Pocket	Axial
126	126OSA	158	158ISA	2.00	2.00	B	Pocket	Axial
127	127ORA	159	159IRA	0.00	2.00	B	Stiffener	Axial
128	128ORA	160	160IRA	-24.00	2.00	B	Stiffener	Axial
129	129OSA	161	161ISA	-26.00	2.00	B	Pocket	Axial
130	130OSA	162	162ISA	-47.00	2.00	B	Pocket	Axial
131	131ORA	163	163IRA	-48.00	2.00	B	Stiffener	Axial

Table A1. Continued

OML GAGE NUMBER	OML GAGE ID	IML GAGE NUMBER	IML GAGE ID	HOOP DIMENSION, (in.)	AXIAL DIMENSION, (in.)	PANEL	LOCATION	ORIENTATION
132	132OWA	164	164IWA	50.27	18.00	B	Weld	Axial
133	133OWA	165	165IWA	50.27	32.84	B	Weld	Axial
134	134ORA	166	166IRA	48.00	32.84	B	Stiffener	Axial
135	135OSA	167	167ISA	47.00	32.84	B	Pocket	Axial
136	136OSA	168	168ISA	26.00	32.84	B	Pocket	Axial
137	137OSA	169	169ISA	2.00	32.84	B	Pocket	Axial
138	138ORA	170	170IRA	0.00	32.84	B	Stiffener	Axial
139	139ORA	171	171IRA	-24.00	32.84	B	Stiffener	Axial
140	140OSA	172	172ISA	-26.00	32.84	B	Pocket	Axial
141	141OSA	173	173ISA	-47.00	32.84	B	Pocket	Axial
142	142ORA	174	174IRA	-48.00	32.84	B	Stiffener	Axial
175	175OWA	207	207IWA	50.27	-32.84	C	Weld	Axial
176	176ORA	208	208IRA	48.00	-32.84	C	Stiffener	Axial
177	177OSA	209	209ISA	47.00	-32.84	C	Pocket	Axial
178	178OSA	210	210ISA	26.00	-32.84	C	Pocket	Axial
179	179OSA	211	211ISA	2.00	-32.84	C	Pocket	Axial
180	180ORA	212	212IRA	0.00	-32.84	C	Stiffener	Axial
181	181ORA	213	213IRA	-24.00	-32.84	C	Stiffener	Axial
182	182OSA	214	214ISA	-26.00	-32.84	C	Pocket	Axial
183	183OSA	215	215ISA	-47.00	-32.84	C	Pocket	Axial
184	184ORA	216	216IRA	-48.00	-32.84	C	Stiffener	Axial
185	185OWA	217	217IWA	50.27	-18.00	C	Weld	Axial
186	186OWA	218	218IWA	50.27	2.00	C	Weld	Axial
187	187ORA	219	219IRA	48.00	2.00	C	Stiffener	Axial
188	188OSA	220	220ISA	47.00	2.00	C	Pocket	Axial
189	189OSA	221	221ISA	26.00	2.00	C	Pocket	Axial
190	190OSA	222	222ISA	2.00	2.00	C	Pocket	Axial
191	191ORA	223	223IRA	0.00	2.00	C	Stiffener	Axial

Table A1. Concluded

OML GAGE NUMBER	OML GAGE ID	IML GAGE NUMBER	IML GAGE ID	HOOP DIMENSION, (in.)	AXIAL DIMENSION, (in.)	PANEL	LOCATION	ORIENTATION
192	192ORA	224	224IRA	-24.00	2.00	C	Stiffener	Axial
193	193OSA	225	225ISA	-26.00	2.00	C	Pocket	Axial
194	194OSA	226	226ISA	-47.00	2.00	C	Pocket	Axial
195	195ORA	227	227IRA	-48.00	2.00	C	Stiffener	Axial
196	196OWA	228	228IWA	50.27	18.00	C	Weld	Axial
197	197OWA	229	229IWA	50.27	32.84	C	Weld	Axial
198	198ORA	230	230IRA	48.00	32.84	C	Stiffener	Axial
199	199OSA	231	231ISA	47.00	32.84	C	Pocket	Axial
200	200OSA	232	232ISA	26.00	32.84	C	Pocket	Axial
201	201OSA	233	233ISA	2.00	32.84	C	Pocket	Axial
202	202ORA	234	234IRA	0.00	32.84	C	Stiffener	Axial
203	203ORA	235	235IRA	-24.00	32.84	C	Stiffener	Axial
204	204OSA	236	236ISA	-26.00	32.84	C	Pocket	Axial
205	205OSA	237	237ISA	-47.00	32.84	C	Pocket	Axial
206	206ORA	238	238IRA	-48.00	32.84	C	Stiffener	Axial

Table A2. Electronic Displacement Indicator (EDI) Locations

EDI	EDI ID	Angular Location, deg.	x, in.	Component Location	Orientation	IML/OML Location
239	D239AA	0°	36.313	Top Attachment Ring	Axial	IML
240	D240AA	90°	36.313	Top Attachment Ring	Axial	IML
241	D241AA	180°	36.313	Top Attachment Ring	Axial	IML
242	D242AA	270°	36.313	Top Attachment Ring	Axial	IML
243	D243BR	60°	0.00	Panel A/B Weld Land	Radial	IML
244	D244BR	180°	0.00	Panel B/C Weld Land	Radial	IML
245	D245BR	300°	0.00	Panel C/A Weld Land	Radial	IML
246	D246CR	0°	0.00	Panel A	Radial	IML
247	D247CR	120°	0.00	Panel B	Radial	IML
248	D248CR	240°	0.00	Panel C	Radial	IML
249	D249DR	60°	-29.375	Panel A/B Weld Land	Radial	IML
250	D250ER	0°	-29.375	Panel A	Radial	IML
251	D251FR	0°	36.313	Top Attachment Ring	Radial	IML
252	D252FR	120°	36.313	Top Attachment Ring	Radial	IML
253	D253FR	240°	36.313	Top Attachment Ring	Radial	IML
254	D254FR	0°	-36.313	Bottom Attachment Ring	Radial	IML
255	D255FR	120°	-36.313	Bottom Attachment Ring	Radial	IML
256	D256FR	240°	-36.313	Bottom Attachment Ring	Radial	IML
257	D257GH	0°	36.313	Top Attachment Ring	Tangential	OML
258	D258GH	0°	-36.313	Bottom Attachment Ring	Tangential	OML
259	D259AA	0°	-36.313	Bottom Attachment Ring	Axial	IML
260	D260AA	90°	-36.313	Bottom Attachment Ring	Axial	IML
261	D261AA	180°	-36.313	Bottom Attachment Ring	Axial	IML
262	D262AA	270°	-36.313	Bottom Attachment Ring	Axial	IML
263	D263AA	0°	(1)	(1)	Axial	IML
264	D264AA	90°	(2)	(2)	Axial	IML
265	D265AA	180°	(3)	(3)	Axial	IML
266	D266AA	270°	(4)	(4)	Axial	IML

$$(1) \delta_{D263AA} = \delta_{D239AA} - \delta_{D259AA}$$

$$(2) \delta_{D264AA} = \delta_{D240AA} - \delta_{D260AA}$$

$$(3) \delta_{D265AA} = \delta_{D241AA} - \delta_{D261AA}$$

$$(4) \delta_{D266AA} = \delta_{D242AA} - \delta_{D262AA}$$

Table A3. Files Used to Generate Color Contour Plots, Load Sequence 4 (Tecplot Format, see Figures 4.8–4.13)

Test Article 2, Load Sequence 4	STAGS Load Step	DIC Photo Number From Test	Total Scan Number From Test	P/P _{cr} ⁽¹⁾	DIC Data File From Test (for contour plots)
		0	633	0.0000	
		1	633	0.0000	SB2-LS4-West-VIC_Image_0001.dat
		2	633	0.0000	SB2-LS4-West-VIC_Image_0002.dat
		3	4520	0.0000	SB2-LS4-West-VIC_Image_0003.dat
		39	5412	0.0000	SB2-LS4-West-VIC_Image_0039.dat
		48	6344	-0.1142	SB2-LS4-West-VIC_Image_0048.dat
		60	6578	0.1501	SB2-LS4-West-VIC_Image_0060.dat
Figures 4.8, 4.9	4 ⁽²⁾	70	6769	0.2498	SB2-LS4-West-VIC_Image_0070.dat
		81	6993	0.3499	SB2-LS4-West-VIC_Image_0081.dat
		91	7205	0.4496	SB2-LS4-West-VIC_Image_0011.dat
		105			SB2-LS4-West-VIC_Image_0105.dat
Figure 4.10	8 ⁽²⁾	109	7560	0.5495	SB2-LS4-West-VIC_Image_0109.dat
		117			SB2-LS4-West-VIC_Image_0117.dat
		119	7785	0.6493	SB2-LS4-West-VIC_Image_0119.dat
		202	9415	0.6494	SB2-LS4-West-VIC_Image_0202.dat
		215	9685	0.7494	SB2-LS4-West-VIC_Image_0215.dat
		224	9856	0.8494	SB2-LS4-West-VIC_Image_0224.dat
Figure 4.11a	13 ⁽²⁾			0.8896	
		237	10121	0.9494	SB2-LS4-West-VIC_Image_0237.dat
Figure 4.11b		245	10292	0.9842	SB2-LS4-West-VIC_Image_0245.dat
Figure 4.12b		247	10329	0.6416	SB2-LS4-West-VIC_Image_0247.dat
Figure 4.12a	230			0.6087	
		324			SB2-LS4-West-VIC_Image_0324.dat
Figure 4.13		339	12161		SB2-LS4-West-VIC_Image_0339.dat
		354	12464	0.1144	SB2-LS4-West-VIC_Image_0354.dat

(1) $P_{cr} = 290,800$ -lb. total load.

(2) Re-run of original STAGS nonlinear prebuckling analysis with solutions obtained at prescribed test loads.

Table A4. Files Used to Generate Color Contour Plots, Load Sequence 5 (Tecplot Format, see Figures 4.34–4.39)

Test Article 2, Load Sequence 5	STAGS Load Step	DIC Photo Number From Test	Total Scan Number From Test	P/P _{cr} ⁽¹⁾	DIC Data File From Test (for contour plots)
		0		0.0000	
		1		0.0000	SB2-LS5-West-VIC_Image_0001.dat
		2	16487	0.0000	SB2-LS5-West-VIC_Image_0002.dat
		3	16487	0.0000	SB2-LS5-West-VIC_Image_0003.dat
		4	17139	0.0002	SB2-LS5-West-VIC_Image_0004.dat
		49	18030	0.0000	SB2-LS5-West-VIC_Image_0049.dat
		58	18234	-0.1147	SB2-LS5-West-VIC_Image_0058.dat
			18268	0.0000	
			69	0.1503	SB2-LS5-West-VIC_Image_0069.dat
Figure 4.34, 4.35	4 ⁽²⁾	78	18631	0.2500	SB2-LS5-West-VIC_Image_0078.dat
		98	19041	0.3491	SB2-LS5-West-VIC_Image_0098.dat
		110	19277	0.4490	SB2-LS5-West-VIC_Image_0110.dat
Figure 4.36	9 ⁽²⁾	128	19636	0.5489	SB2-LS5-West-VIC_Image_0128.dat
		146	19999	0.6485	SB2-LS5-West-VIC_Image_0146.dat
		160	20283	0.7483	SB2-LS5-West-VIC_Image_0160.dat
		170	20485	0.8480	SB2-LS5-West-VIC_Image_0170.dat
		175			SB2-LS5-West-VIC_Image_0175.dat
Figure 4.37a, 4.38a	14 ⁽²⁾			0.9213	
		179	20669	0.9480	SB2-LS5-West-VIC_Image_0179.dat
		185	20790	0.9619	SB2-LS5-West-VIC_Image_0185.dat
Figure 4.37b, 4.38b		186	20790	0.9619	SB2-LS5-West-VIC_Image_0186.dat
Figure 4.39b		187	20822	0.6150	SB2-LS5-West-VIC_Image_0187.dat
		248			SB2-LS5-West-VIC_Image_0248.dat
		268			SB2-LS5-West-VIC_Image_0268.dat
		281	22699	0.5763	SB2-LS5-West-VIC_Image_0281.dat
Figure 4.39a				05650	
		316			SB2-LS5-West-VIC_Image_0316.dat
		330	23683	-0.0009	SB2-LS5-West-VIC_Image_0330.dat
		345	23977	0.1143	SB2-LS5-West-VIC_Image_0345.dat
		348			SB2-LS5-West-VIC_Image_0348.dat

(1) $P_{cr} = 290,800\text{-lb. total load.}$

(2) Re-run of original STAGS nonlinear prebuckling analysis with solutions obtained at prescribed test loads.

REPORT DOCUMENTATION PAGE				Form Approved OMB No. 0704-0188	
<p>The public reporting burden for this collection of information is estimated to average 1 hour per response, including the time for reviewing instructions, searching existing data sources, gathering and maintaining the data needed, and completing and reviewing the collection of information. Send comments regarding this burden estimate or any other aspect of this collection of information, including suggestions for reducing this burden, to Department of Defense, Washington Headquarters Services, Directorate for Information Operations and Reports (0704-0188), 1215 Jefferson Davis Highway, Suite 1204, Arlington, VA 22202-4302. Respondents should be aware that notwithstanding any other provision of law, no person shall be subject to any penalty for failing to comply with a collection of information if it does not display a currently valid OMB control number.</p> <p>PLEASE DO NOT RETURN YOUR FORM TO THE ABOVE ADDRESS.</p>					
1. REPORT DATE (DD-MM-YYYY)	2. REPORT TYPE		3. DATES COVERED (From - To)		
01-03 - 2017	Technical Publication				
4. TITLE AND SUBTITLE			5a. CONTRACT NUMBER		
Buckling Test Results and Preliminary Test and Analysis Correlation from the 8-Foot-Diameter Orthogrid-Stiffened Cylinder Test Article TA02			5b. GRANT NUMBER		
Test Dates: 3-6 February 2009			5c. PROGRAM ELEMENT NUMBER		
6. AUTHOR(S)			5d. PROJECT NUMBER		
Hilburger, Mark, W.; Waters, W. Allen, Jr.; Haynie, Waddy T.; Thornburgh, Robert P.			5e. TASK NUMBER		
			5f. WORK UNIT NUMBER		
			869021.04.07.01.13		
7. PERFORMING ORGANIZATION NAME(S) AND ADDRESS(ES)			8. PERFORMING ORGANIZATION REPORT NUMBER		
NASA Langley Research Center Hampton, VA 23681-2199			L-20801		
9. SPONSORING/MONITORING AGENCY NAME(S) AND ADDRESS(ES)			10. SPONSOR/MONITOR'S ACRONYM(S)		
National Aeronautics and Space Administration Washington, DC 20546-0001			NASA		
			11. SPONSOR/MONITOR'S REPORT NUMBER(S)		
			NASA/TP-2017-219587		
12. DISTRIBUTION/AVAILABILITY STATEMENT					
Unclassified - Unlimited					
Subject Category 16 Space Transportation and Safety					
Availability: NASA STI Program (757) 864-9658					
13. SUPPLEMENTARY NOTES					
14. ABSTRACT					
Results from the testing of cylinder test article SBKF-P2-CYL-TA02 (referred to herein as TA02) are presented. TA02 is an 8-foot-diameter (96-inches), 78.0-inch-long, aluminum-lithium (Al-Li), orthogrid-stiffened cylindrical shell similar to those used in current state-of-the-art launch-vehicle structures and was designed to exhibit global buckling when subjected to combined compression and bending loads. The testing was conducted at the Marshall Space Flight Center (MSFC), February 3-6, 2009, in support of the Shell Buckling Knockdown Factor Project (SBKF). The test was used to verify the performance of a newly constructed buckling test facility at MSFC and to verify the test article design and analysis approach used by the SBKF researchers.					
15. SUBJECT TERMS					
Orthogrid; Cylinder; Buckling; Testing; Design; Knockdown Factors					
16. SECURITY CLASSIFICATION OF:			17. LIMITATION OF ABSTRACT	18. NUMBER OF PAGES	19a. NAME OF RESPONSIBLE PERSON
a. REPORT	b. ABSTRACT	c. THIS PAGE	UU	104	STI Help Desk (email: help@sti.nasa.gov)
U	U	U			19b. TELEPHONE NUMBER (Include area code)
					(443) 757-5802